THE FABRICATION AND CHARACTERIZATION OF ALUMINUM AND MAGNESIUM NANOPARTICLES

by

Mark Michel Swartz

A dissertation submitted to the faculty of
The University of Utah
in partial fulfillment of the requirements for the degree of

Doctor of Philosophy

Department of Chemistry

The University of Utah

May 2017

The University of Utah Graduate School

STATEMENT OF DISSERTATION APPROVAL

The dissertation of **Mark Michel Swartz**

has been approved by the following supervisory committee members:

Jennifer Shumaker-Parry	, Chair	**8/22/16** Date Approved
Joel Mark Harris	, Member	**8/22/16** Date Approved
John C. Conboy	, Member	**8/22/16** Date Approved
Cynthia Burrows	, Member	**8/22/16** Date Approved
Bruce K. Gale	, Member	**8/22/16** Date Approved

and by **Cynthia Burrows**, Chair/Dean of

the Department/College/School of **Chemistry**

and by David B. Kieda, Dean of The Graduate School.

ABSTRACT

Plasmonics, the study of light metal interactions, has shown great potential in the fields of spectroscopy, catalysis, medicine, and photovoltaics. There is significant interest in the design of metal nanoparticles that interact with specific wavelengths of light. By changing the size, shape, and metal composition, nanoparticles can be tuned to interact with different regions of the electromagnetic spectrum. Gold and silver are the two most common metals used in plasmonics, but are inefficient in the ultraviolet (UV) wavelength range and expensive. This has driven the research of plasmonics with non-noble metals that support plasmons in the UV and are cost-effective. Aluminum has been widely considered to be the ideal metal to fill this application has favorable plasmonic properties in the UV wavelength range and is cheap. However, Al is difficult to structure at the nanoscale due to its rapidly forming and chemically stable native oxide.

Here we report the simple, large scale fabrication of Aluminum nanoparticle antennas. These nanoparticles have plasmon resonances in the UV, visible, near infrared, and infrared wavelengths. We demonstrate the utility of these nanoparticles as substrates for surface-enhanced infrared absorption spectroscopy, a wavelength range that is usually not associated with Aluminum. We also demonstrate that this fabrication technique allows for the fabrication of more complex nanoparticle geometries. These complex nanoparticles geometries have utility in both fundamental studies, and in surface-enhanced spectroscopies.

We also demonstrate the potential of magnesium as a plasmonic metal. Magnesium is shown to support plasmon resonances from the UV to near infrared wavelengths. We investigate the plasmonic properties of nanostructured magnesium films and demonstrate that pure magnesium does not support sharp nanoscale features. By alloying magnesium with aluminum, its plasmonic and structural properties are improved.

To my family, for their unwavering support throughout my graduate career.

TABLE OF CONTENTS

ABSTRACT iii

ACKNOWLEDGEMENTS viii

Chapters

1. INTRODUCTION 1

    1.1 Localized Surface Plasmon Resonance 1
    1.2 Nanoparticle Fabrication 6
    1.3 Dissertation Outline 10
    1.4 References 15

2. ALUMINUM NANOCRESCENT PLASMONIC ANTENNAS FABRICATED BY COPPER MASK NANOSPHERE TEMPLATE LITHOGRAPHY 21

    2.1 Introduction 21
    2.2 Materials and Methods 24
    2.3 Results and Discussion 26
    2.4 Conclusions 33
    2.5 References 40

3. ARRAYED ALUMINUM PLASMONIC ANTENNAS FOR SURFACE-ENHANCED INFRARED ABSORPTION 44

    3.1 Introduction 44
    3.2 Materials and Methods 45
    3.3 Results and Discussion 48
    3.4 Conclusion 57
    3.5 References 64

4. HOMO- AND HETEROMETALLIC DIMER NANOCRESCENT ANTENNAS 68

    4.1 Introduction 68
    4.2 Materials and Methods 69
    4.3 Results and Discussion 71
    4.4 Conclusions 79
    4.5 References 85

5. INFLUENCE OF ALUMINUM CONTENT ON PLASMONIC BEHAVIOR OF MG-AL ALLOY THIN FILMS....89

5.1 Abstract....89
5.2 Introduction....90
5.2 Materials and Methods....91
5.3 Results and Discussion....94
5.4 Conclusions....102
5.5 References....111

6. MAGNESIUM NANOHOLE ARRAYS....114
6.1 Introduction....114
6.2 Materials and Methods....115
6.3 Results and Discussion....117
6.4 Conclusions....120
6.5 References....124

7. CONCLUSION AND FUTURE WORK....126

7.1 Conclusion....126
7.2 Future Work....127
7.3 References....130

ACKNOWLEDGEMENTS

I would like to thank my advisor, Dr. Jennifer Shumaker-Parry for her guidance over these past 5 years. I would also like to thank the current and former members of the Shumaker-Parry lab. I am eternally grateful to the state of Utah as it has provided me with numerous adventures outside of the lab.

I would like to thank Stephanie Meek, who has put up with me for the last few years both as a partner and roommate. She has been instrumental in my success in these last few years of graduate school. Most importantly I would like to thank my family. My parents, Mike and Becky Swartz, have been the best role models in my life. They continually support my education and all my decisions, good or bad. My brother, Thomas, has been my best friend and mentor, without him I would have no humility. Without their support, I would have never made it this far in my academic career.

CHAPTER 1

INTRODUCTION

1.1 Localized Surface Plasmon Resonance

As materials are scaled down to nanometer sizes, their physical and chemical properties change drastically. The noble metal gold (Au), which has a distinct yellow appearance as a bulk material is a common example. By decreasing the dimensions of Au particles to the nanoscale, this optical property that we take for granted is significantly altered. This change in the optical property of Au has been exploited for centuries to make red stained glass. Au's appearance at the nanoscale is explained by plasmonics; the study of light-metal interactions. When metal particles are decreased to the nanometer size, nanoparticles (NPs) experience the electric component of an electromagnetic (EM) wave as a uniform field.[1] When the electric field passes over the particle, electrons in the conduction band are perturbed leading to a dipole whose direction is dictated by the incident field (Figure 1.1).[1, 2] This collective oscillation is known as localized surface plasmon resonance (LSPR) and spatially focuses the EM field near the surface of the particle. The frequency of the resonance condition depends on the size, shape, metal, and dielectric environment of the NP. This field enhancement decays evanescently, leading to areas of high EM field enhancement near the particle's surface. This property has been used to nondestructively enhance spectroscopic signals in techniques such as; surface-enhanced Raman spectroscopy (SERS), infrared absorbance (SEIRA), and fluorescence

(SEF).[3-10]

Plasmonic materials have applications in fields beyond just surface-enhanced spectroscopies. In photovoltaics, metal NPs are used to improve the solar efficiency by increasing light absorption and scattering.[11-15] Likewise these particles have been used in photocatalysis, helping to improve reaction efficiencies by increasing the amount of available light at the nanoscale.[16-19] Metal NPs have also found use in the medical community for therapeutic and diagnostic applications.[20, 21] In the aforementioned applications the metal NPs must interact with specific wavelengths of light, which is accomplished by changing the size, shape, and metal composition. Consequently, designing and fabricating metal NPs to interact with specific wavelengths remains an active area of research.

1.1.2 Noble metals

In order to design plasmonic materials, there are considerations that must be accounted for. The sphere in Figure 1.1 is polarized by the incident light which results in an enhanced electric field on the surface. The field enhancement at the surface of a metal sphere ($\boldsymbol{E}_{out}$) is described by Eq. 1.1. The first term describes the contribution from the incident field and the second term describes the enhancement due to the induced dipole. Here E_o is the magnitude of the applied electric field, α represents the polarizability of the metal sphere while x, y, z, **x**, **y**, **z** are the Cartesian coordinates and Cartesian unit vectors, respectively, while the radial distance is represented by r. This equation shows that the field enhancement of the sphere is primarily dependent on distance from the surface (r, which leads to the evanescent field decay) and the polarizability of the sphere. The polarizability of a metal sphere is described by Eq. 1.2 and is dependent on the radius of

the sphere (a), the complex dielectric function of the metal sphere (ε_{in}), and of the surrounding media (ε_{out}). The polarizability of the sphere reaches a maximum when $-2\varepsilon_{in} = \varepsilon_{out}$, consequently this condition leads to the largest field enhancements. Since the dielectric function of a metal is a complex number (Eq. 1.3), the imaginary component ($\varepsilon 2$) must be small while the real component ($\varepsilon 1$) should be large and negative.[22] By selecting metals that are readily polarizable, nanoparticles with large field enhancements can be designed.

$$\boldsymbol{E}_{out} = E_o \boldsymbol{z} - \alpha E_o \left[\frac{\boldsymbol{z}}{r^3} - \frac{3z}{r^5} (z\boldsymbol{z} + x\boldsymbol{x} + y\boldsymbol{y}) \right] \tag{1.1}$$

$$\alpha = a^3 \frac{\varepsilon_{in} - \varepsilon_{out}}{\varepsilon_{in} + 2\varepsilon_{out}} \tag{1.2}$$

$$\varepsilon_{in} = \varepsilon 1 + i\varepsilon 2 \tag{1.3}$$

Au and silver (Ag) have been used extensively in the field of plasmonics, especially in SERS and SEIRA, because of their favorable dielectric properties.[9, 23-27] An ideal plasmonic material will conduct electrons and not absorb light over the wavelengths of interest. From Figure 1.2 it is evident that $\varepsilon 1$ for both Au and Ag is large and negative over the visible and IR wavelength range. A negative $\varepsilon 1$ indicates the material is highly conductive, allowing electrons to move freely over these wavelengths, a property that is desirable if we want to induce a collective electron oscillation. Alternatively $\varepsilon 2$ is small and positive over a similar wavelength range. High values of $\varepsilon 2$ are associated with losses in the material (typically by absorption) and are not desirable as they dampen the polarizability. Ag is widely considered to be the best plasmonic metal in terms of optical properties, due to its low losses (low $\varepsilon 2$) and high conductivity (high $\varepsilon 1$) over the visible and near-infrared (NIR) wavelengths. While Au is inferior to Ag in terms of optical

properties, its chemical properties are superior.

Au is one of the most chemically inert metals available, consequently, it is safe to handle and stable in many applications. The primary concern for plasmonic metals is their susceptibility to oxidation. Au does not succumb to oxidation under normal atmospheric conditions unlike Ag. On a macroscopic level, Ag will slowly oxidize over time, giving it a tarnished appearance. At the nanometer scale, the oxidation process is more pronounced due to the increased surface area. The Ag oxide that forms is not self-limiting and does not support a plasmon resonance, meaning that Ag NPs have a limited shelf-life. Consequently many researchers favor Au both in fundamental studies and in applications.

While Au and Ag possess desirable optical characteristics in the visible and NIR wavelength ranges, they are incapable of supporting plasmon resonances in the ultraviolet (UV) range. As $\varepsilon 1$ decreases to zero and $\varepsilon 2$ increases, indicating no conductivity and high losses (Figure 1.2). This phenomenon is due to the presence of interband transitions for Ag and Au at around 310 nm and 500 nm, respectively. Consequently, light below these wavelengths leads to the excitation of electron-hole pairs instead of coherent electron oscillations. Metals capable of supporting plasmons in the UV region have garnered considerable attention in recent years. Plasmonic metals that are active in the UV have potential applications in photovoltaics, catalysis, and surface-enhanced spectroscopies particularly UV-SERS.[3, 16, 17, 19, 28-33]

1.1.3 Non-noble plasmonic metals

Several non-noble metals have the potential to be used in UV plasmonics, including aluminum (Al), magnesium (Mg), indium, gallium, and lead.[29, 30, 34] These metals maintain their conductivity and have relatively low losses at UV wavelengths. Several of the non-

noble metals have not found broad appeal in the plasmonics community due to various chemical or physical properties. Lead is highly toxic and consequently cannot be used in biological applications, gallium melts at very low temperatures (29.8˚C) which makes it very difficult to structure at the nanoscale, indium is difficult to structure and is expensive,[35] and, while magnesium has been shown to have excellent UV plasmonic properties, pure Mg suffers from rapid and complete oxidation in the presence of water[34, 36], essentially eliminating the use of pure Mg in any biological application. Al has been the most promising metal since it is inexpensive, has limited toxicity, is thermally stable, and has a self-limiting oxide.

Although Al is one of the more promising of the non-noble metals, there are a few properties that make it difficult to structure at the nanoscale. One notable issue is the presence of the Al oxide layer that forms rapidly upon exposure to oxygen. Unlike Ag or Mg, this oxide layer is self-limiting at ~3nm and is thermally and chemically stable (Figure 1.3).[37] Several common methods for NP fabrication have been employed to synthesize and fabricate Al plasmonic structures with varying degrees of success.[38]

1.1.4 Shape effects of nanoparticle antennas

Metal NPs can be treated as antennas that manipulate light at the nanoscale, however, radio frequency (RF) antenna theory does not always accurately describe the interaction of metal NPs and light at optical frequencies.[39] This is because metals experience large resistive losses at optical frequencies resulting in a phase offset between the incident radiation and the electronic oscillation in the metal. Some aspects of RF antenna theory translate well at the nanoscale, such as sharp tips leading to large field enhancements.[40] One large difference in the design of RF antennas and nanoscale antennas

is the issue of impedance matching, which helps to maximize energy transfer from the incident radiation. In RF antennas, this is accomplished through the use of transmission lines which couple the circuit load to the antenna. In a nanoscale antenna system, this is achieved through the use of a small, dielectric gap which helps to maximize energy transfer. The design of materials that can produce large field enhancements to enhance spectroscopic sensitivity is focused on producing sharp features, small gaps, or a combination of the two.[41-43]

1.2 Nanoparticle Fabrication

1.2.1 Bottom up synthesis (also known as metal salt reduction)

One common technique for the synthesis of plasmonic NPs, is the reduction of a metal salt. This method is well suited for the production of large amounts of particles in solution. For the synthesis Au and Ag NPs, this process is very straightforward, $AuCl_4$ or $AgNO_3$ is reduced with $NaBH_4$ and capping agents are used to direct particle shape.[44, 45] A similar approach can be used to synthesize Al NPs, where Al hydride is reduced to Al metal.[46] However, Al hydrides undergo rapid exothermic reduction in the presence of water, and consequently, significant precautions are required.[38] Compared to Au or Ag, comparatively little work has been done on the bottom up synthesis of AlNPs; consequently, there is a limited range of shapes and sizes that have been achieved, thus limiting the tunability of this approach. In a broader sense, the bottom up synthesis of metal NPs suffers from the lack of orientation. This is not an issue if the particles will remain in solution, but if the particles will be used in a system where uniform orientation is necessary (for photovoltaics or optics), then this approach falls short.

1.2.2 Top down fabrication

An alternative approach to the fabrication of NPs that maintains orientation and can be used with a variety of plasmonic materials is the patterning of a thin metal film. In this approach, a mask is created over a flat substrate and a thin (5-50nm) metal film is deposited through the mask either by sputtering or thermal deposition. This approach has been used extensively in the fabrication of Au and Ag NPs and can, in most cases, be transferred to the fabrication of Al NPs. The fabrication of a nanoscale mask is commonly achieved using electron beam lithography (EBL).[4, 47-49] In EBL, an electron beam is used to draw patterns in a polymer mask and the desired plasmonic metal is deposited over the mask. Solvents are then used to dissolve out the mask and the plasmonic NPs are left behind on the substrate. A wide variety of sizes and shapes can be fabricated using EBL, and thus the technique lends itself very well to the study of fundamental properties of metal nanostructures. EBL suffers from two major limitations, minimum achievable feature size and cost. EBL is limited to ~10 nm feature sizes, whereas a 5 nm feature size is desirable for most plasmonic antennas.[40] Additionally, EBL is costly and time-consuming for fabricating structures over large substrate areas; consequently, it has limited applicability in a commercial setting.[38, 39] Focused ion-beam (FIB) milling is very similar to EBL except patterns are drawn using a beam of focused ions instead of electrons. Single nanometer feature sizes can be achieved using a helium FIB, however the cost is considerably higher than EBL.[50]

1.2.3 Nanosphere lithography

Alternative approaches for the cost-effective production of masks include laser interference and polystyrene nanospheres.[51-55] Nanosphere lithography (NSL) is a

common metal NP fabrication technique that was made popular by the Van Duyne group at Northwestern.[52, 56-60] In this method, a close-packed monolayer of polystyrene nanospheres is deposited on a flat substrate and a plasmonic metal is deposited over the surface. The metal fills in the gaps between the particles, and, upon removal of the templates, a uniform array of nanotriangles is left behind. This method has been used with a variety of different metals including copper (Cu) and Al, and produced different aspect ratios for nanotriangles.[56-58] While this method is a relatively cost-effective way to fabricate NPs, it is limited by the range of shapes that can be produced as well as the spacing and surface density of NPs.

Several variations of NSL have been developed to overcome the limited range of shapes. Moiré nanosphere lithography (MNL), hole-mask colloid lithography (HCL), and nanosphere template lithography (NTL) are variations of NSL that have greatly expanded upon the range of achievable structures.[37, 53-55] MNL is the simplest variation of NSL and involves depositing two close-packed monolayers of polystyrene templates on top of each other. An oxygen plasma is then used to shrink the templates and the metal is deposited on the surface. The two monolayers' orientation relative to each other determines the final NP shape (Figure 1.4A). There is no way to control this orientation, consequently, what is left is a random distribution of shapes across the substrate.[54] So far this technique has only been used for the fabrication of Au NPs, but it could easily be applied towards Al plasmonics.

HCL has shown remarkable promise in regards to metal compatibility and shape tunability.[37, 61, 62] Much like EBL, a polymer layer is deposited onto the substrate first, followed by a dispersion of polystyrene nanospheres (Figure 1.4B). A metal coating is

then applied over the surface (typically Au), and then the nanospheres are removed leaving a perforated metal film over the polymer. Oxygen plasma is used to remove the polymer inside the holes, revealing the substrate. The plasmonic metal is then deposited over this mask, and by varying the metal deposition angle, different shapes are produced. The polymer film is dissolved away and what remains are the NPs adhered to the substrate. Significant control over the shape of particles is achieved and it is compatible with a range of metals including Mg, which is a challenging metal to work with.[63] The only disadvantage to this method is the number of steps increases fabrication costs.

Reducing the number of steps in the fabrication process helps to bring the overall cost down. NTL is a three-step technique that has been used to make a disk, ring, and crescent nanostructures out of Au, Ag, and recently, Al.[23, 53, 55, 64] Polystyrene nanospheres are dispersed onto a flat surface and metal is deposited normal to the surface or at an angle to produce ring or crescent structures, respectively (Figure 1.4C). For nanodisks, the metal is deposited first followed by the polystyrene templates. The metal film is then removed using an argon plasma while the metal underneath the polystyrene template remains on the surface, thus each polystyrene nanosphere acts as an individual template for the final plasmonic nanostructure. This method has worked well for the fabrication of Ag and Au plasmonic nanostructures with resonances tuned from the visible through IR wavelengths.[23, 65]

Until recently, NTL was not successful for the fabrication of Al plasmonic structures. While Al can be etched using an argon plasma, it takes a significant amount of time to etch through the initial oxide layer. Consequently, the polystyrene templates would deform leading to irregular structures that were difficult to reproduce. The inability of

NTL to utilize Al as a plasmonic material prevented this method from being utilized in the UV wavelengths.

1.3 Dissertation Outline

The over-arching goal of this dissertation work is to fabricate and examine the fundamental optical properties of plasmonic NPs made from noble and non-noble metals. By using non-noble metals, we are able to study plasmonic properties of metal NPs at wavelengths from the UV through IR wavelength ranges. These metal NPs are fabricated using cost-effective materials and techniques, making them appealing in fields beyond fundamental plasmonics.

1.3.1 NTL of Al nanocrescents

While NTL is a versatile and cost-effective method for the fabrication of Ag and Au NPs, it has been difficult to incorporate Al. The native alumina layer that forms over the film is challenging to remove with an argon plasma without simultaneously degrading the templates. Here we demonstrate how NTL can be used for the fabrication of Al nanocrescents (AlNCs) by incorporating a sacrificial copper layer. The resulting NCs have LSPRs that can be tuned from the UV to the IR ranges/wavelengths by increasing the diameter of the polystyrene templates. Additionally, we demonstrate that our fabrication method does not appreciably increase the oxide layer covering the particles.

1.3.2 Al and Au nanocrescent arrays in SEIRA

Simulations have shown the NC geometry leads to large field enhancements at the tips of the structures, meaning these structures have the potential to be useful in surface-enhanced spectroscopic techniques.[23, 33] However, the previous fabrication results in

particles that are dispersed over a large substrate area. Consequently the region of enhancement is small compared to the total surface area of the substrate. By close-packing the polystyrene templates, the entire substrate surface can be covered in plasmonic NPs, thereby increasing the area that undergoes enhancement. We demonstrate that this close-packing significantly increases the number of particles available for sensing. Additionally, we show Al NPs utility at long wavelengths by measuring SEIRA responses and comparing it to Au arrays with similar LSPR.

1.3.3 Homo- and heterometallic dimer nanocrescents

Previous work utilizing NTL was limited to the fabrication of three shapes; rings, disks, and crescents. By incorporating a sacrificial copper mask, we have added an additional structure that may be fabricated using NTL. The deposition of three metallic films as opposed to just two, we demonstrate the versatility of NTL to expand into more complicated geometries. Through the creation of a circular mask with copper, plasmonic metals deposited at opposing angles result in the fabrication of dimer NCs (DNCs). Due to Al's ability to form a rapid, self-limiting oxide layer, these DNCs are separated by nanometer sized gaps. Additionally this method can be used for the production of monometallic (Al-Al) or bimetallic (Al-Au) DNCs. These more complicated geometries have NIR/IR active resonances and presumably high-field enhancements due to the presence of a nanoscale gap.

1.3.4 Mg-Al alloy thin films for plasmonics

In addition to Al as a non-noble plasmonic metal, magnesium was studied for its ability to support a LSP in the UV wavelengths. In a collaborative effort, Mg-Al alloy thin

films were designed to improve the plasmonic properties of pure Mg. The effect of metal deposition rate on the structural and optical properties of Mg thin films was examined. By alloying Mg thin films with Al, the LSPR figure of merit could be improved to a point that exceed pure Mg or Al alone. These metals alloys were then patterned at the nanoscale using NSL and their LSPR properties were examined.

1.3.5 Mg hole arrays

Further studies of Mg's plasmonic properties were conducted using a nanohole array. The hole arrays were created by first depositing a close-packed monolayer of PS templates followed by oxygen plasma etching to create gaps in between the templates. Deposition of a thin Mg film over the PS templates and subsequent template removal leads to a periodic hole array. Previous work highlighted the difficulty associated with structuring Mg at the nanoscale. Consequently a different nanoscale geometry, one that resulted in fewer sharp features, was investigated. These hole arrays maintained their nanometer scale features and exhibited tunable LSPR and surface plasmon resonance modes in the UV, visible, and NIR wavelengths.

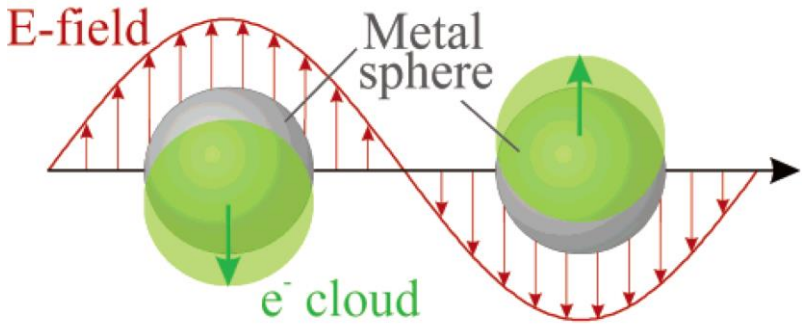

Figure 1.1 Cartoon representation of the electronic oscillation in a metal nanoparticle induced by an electromagnetic wave (Reprinted with permission from Kelly, K.L.; Coronado, E.; Zhao, L. L.; Schatz, G. C. *J. Phys. Chem. B* **2003**, 107, 668-677, Figure 1. Copyright 2003 American Chemical Society).

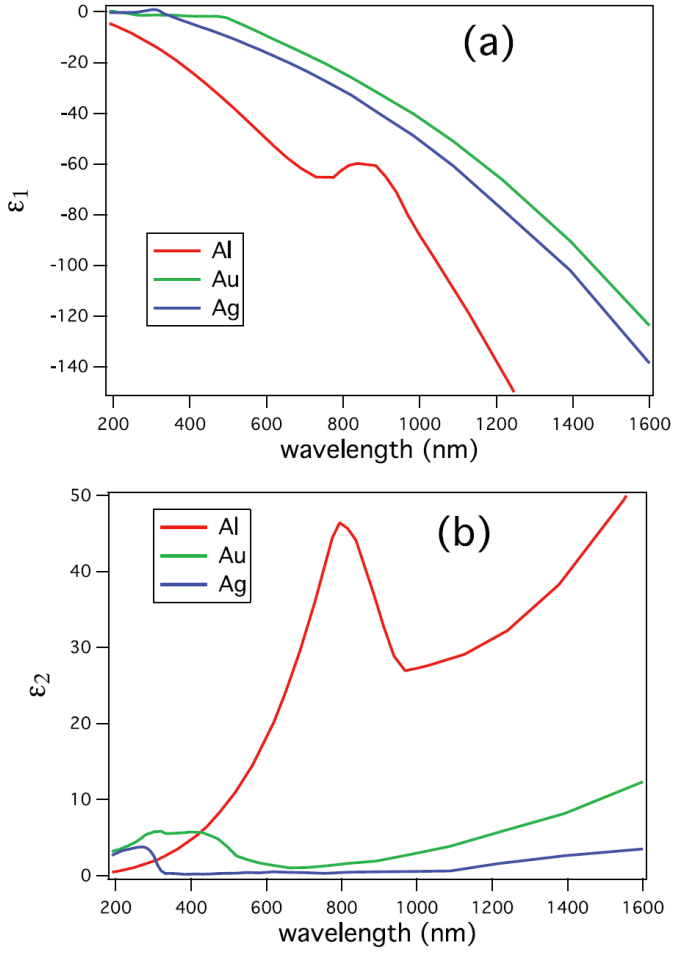

Figure 1.2 Optical response of different metals gives insight into their ability to support plasmon resonances. Real (a) and imaginary (b) components of the dielectric functions for Al, Au, and Ag (Reprinted with permission from Gerard, D.; Gray, S. K. *J. Phys. D: Appl. Phys.* **2015**, 48, 184001, Figure 1 Copyright 2015 IOP Science).

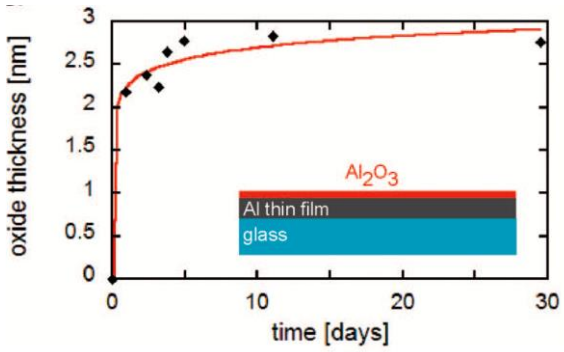

Figure 1.3 Oxide thickness of a 20 nm Al film measured by angle resolved X-ray photoelectron spectroscopy (Reprinted with permission from Langhammer, C.; Schwind, M.; Kasemo, B.; Zoric, I. *Nano Lett.***2008**, 8(5), 1461-1471, Figure 2A. Copyright 2008 Americal Chemical Society).

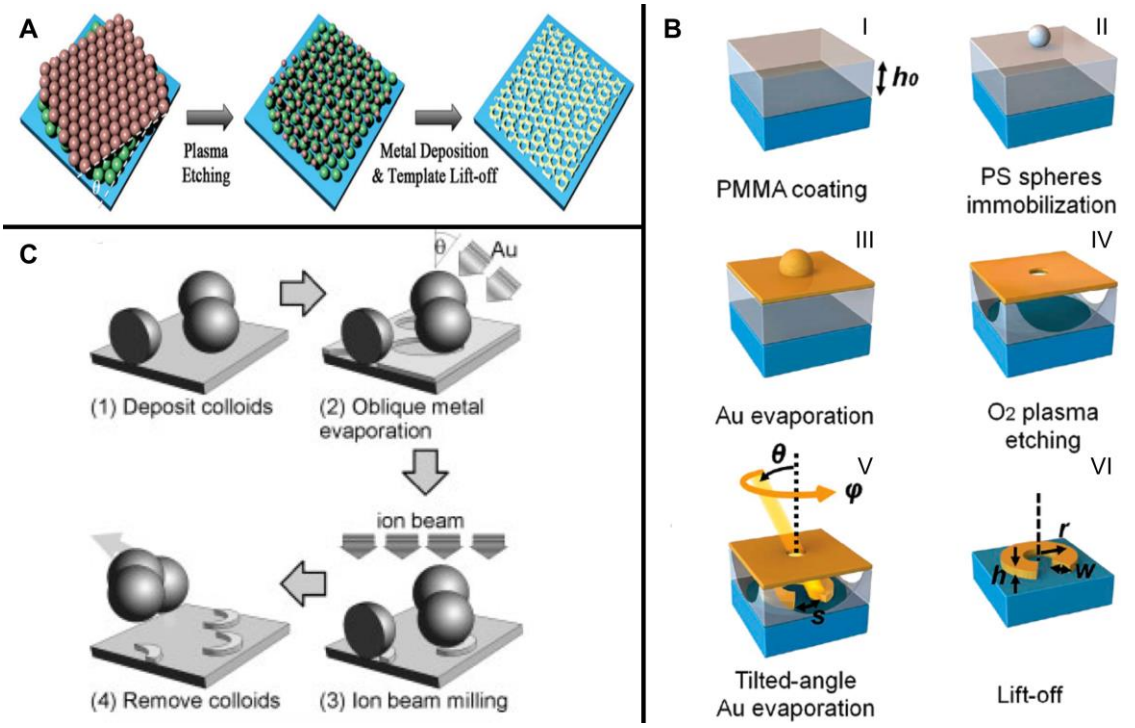

Figure 1.4 Polystyrene nanospheres can be arranged in multiple configurations to yield different plasmonic structures. A) Schematic representation of Moire Nanosphere lithography (Reprinted with permission from Wu, Z.; Chen, K.; Menz, R.; Nagao, T.; Zheng, Y. *Nanoscale*, **2015**, 7, 20391 Figure 1 Copyright 2015 Royal Society of Chemistry). B) Depiction of Hole-Mask Colloid lithography for the fabrication of split-ring resonators (Reprinted with permission from Cataldo, S.; Zhao, J.; Neubrech, F.; Frank, B.; Zhang, C.; Braun, P. V.; Giessen, H *ACS NanoI* **2012**, 6(1), 979 Figure 1 Copyright 2012 American Chemical Society). C) Nanosphere template lithography for the fabrication of gold nanocrescents (Reprinted with permission from Shumaker-Parry, J.; Rochholz, H.; Kreiter, M. *Adv. Mater.* **2005**, 17, 2131, Figure 1 Copyright 2005 Wiley-VCH).

1.4 References

(1) Kelly, K. L.; Coronado, E.; Zhao, L. L.; Schatz, G. C. The Optical Properties of Metal Nanoparticles: The Influence of Size, Shape, and Dielectric Environment. *J. Phys. Chem. B* **2003**, *107*, 668-677.

(2) Willets, K. A.; Duyne, R. P. V. Localized Surface Plasmon Resonance Spectroscopy and Sensing. *Annu. Rev. Phys. Chem.* **2007**, *58*, 267-297.

(3) Chowdhury, M. H.; Ray, K.; Gray, S. K.; Pond, J.; Lakowicz, J. R. Aluminum Nanoparticles as Substrates for Metal-Enhanced Fluorescence in the Ultraviolet for the Label-Free Detection of Biomolecules. *Anal. Chem.* **2009**, *81*, 1397-1403.

(4) Cerjan, B.; Yang, X.; Nordlander, P.; Halas, N. J. Asymmetric Aluminum Antennas for Self-Calibrating Surface-Enhanced Infrared Absorption Spectroscopy. *ACS Photonics* **2016**, *3*, 354-360.

(5) Brown, L. V.; Zhao, K.; King, N.; Sobhani, H.; Nordlander, P.; Halas, N. J. Surface-Enhanced Infrared Absorption Using Individual Cross Antennas Tailored to Chemical Moieties. *J. Am. Chem. Soc.* **2013**, *135*, 3688-3695.

(6) Wang, H.; Levin, C. S.; Halas, N. J. Nanosphere Arrays with Controlled Sub-10-nm Gaps as Surface-Enhanced Raman Spectroscopy Substrates. *J. Am. Chem. Soc.* **2005**, *127*, 14992-14993.

(7) Jensen, T. R.; Van Duyne, R. P.; Johnson, S. A.; Maroni, V. A. Surface-Enhanced Infrared Spectroscopy: A Comparison of Metal Island Films with Discrete and Nondiscrete Surface Plasmons. *Appl. Spectrosc.* **2000**, *54*, 371-377.

(8) Nie, S.; Emory, S. R. Probing Single Molecules and Single Nanoparticles by Surface-Enhanced Raman Scattering. *Science* **1997**, *275*, 1102-1106.

(9) Jensen, T. R.; Duyne, R. P. V.; Johnson, S. A.; Maroni, V. A. Surface-Enhanced Infrared Spectroscopy: A Comparison of Metal Island Films with Discrete and Nondiscrete Surface Plasmons. *Appl. Spectrosc.* **2000**, *54*, 371-377.

(10) Merklin, G. T.; Griffiths, P. R. Effect of Microscopic Surface Roughness in Surface-Enhanced Infrared Absorption Spectrometry. *J. Phys. Chem. B* **1997**, *101*, 5810-5813.

(11) Atwater, H. A.; Polman, A. Plasmonics for Improved Photovoltaic Devices. *Nat. Mater.* **2010**, *9*, 205-213.

(12) Ferry, V. E.; Munday, J. N.; Atwater, H. A. Design Considerations for Plasmonic Photovoltaics. *Adv. Mater.* **2010**, *22*, 4794-4808.

(13) Kochergin, V.; Neely, L.; Jao, C.-Y.; Robinson, H. D. Aluminum Plasmonic

Nanostructures for Improved Absorption in Organic Photovoltaic Devices. *Appl. Phys. Lett.* **2011**, *98*, 13305.

(14) Jo, H.; Sohn, A.; Shin, K.-S.; Kumar, B.; Kim, J. H.; Kim, D.-W.; Kim, S.-W. Novel Architecture of Plasmon Excitation Based on Self-Assembled Nanoparticle Arrays for Photovoltaics. *ACS Appl. Mater. Interfaces* **2013**, *6*, 1030-1035.

(15) Xu, Q.; Liu, F.; Liu, Y.; Meng, W.; Cui, K.; Feng, X.; Zhang, W.; Huang, Y. Aluminum Plasmonic Nanoparticles Enhanced Dye Sensitized Solar Cells. *Opt. Express* **2014**, *22*, A301-A310.

(16) Zhou, L.; Zhang, C.; McClain, M. J.; Manjavacas, A.; Krauter, C. M.; Tian, S.; Berg, F.; Everitt, H. O.; Carter, E. A.; Nordlander, P.; Halas, N. J. Aluminum Nanocrystals as a Plasmonic Photocatalyst for Hydrogen Dissociation. *Nano Lett.* **2016**, *16*, 1478-1484.

(17) Swearer, D. F.; Zhao, H.; Zhou, L.; Zhang, C.; Robatjazi, H.; Martirez, J. M. P.; Krauter, C. M.; Yazdi, S.; McClain, M. J.; Ringe, E.; Carter, E. A.; Nordlander, P.; Halas, N. J. Heterometallic Antenna−Reactor Complexes for Photocatalysis. *Proc. Natl. Acad. Sci USA* **2016**, *13*, 8916-8920.

(18) Xie, W.; Walkenfort, B.; Schlücker, S. Label-Free SERS Monitoring of Chemical Reactions Catalyzed by Small Gold Nanoparticles Using 3D Plasmonic Superstructures. *J. Am. Chem. Soc.* **2013**, *135*, 1657-1660.

(19) Hao, Q.; Wang, C.; Huang, H.; Li, W.; Du, D.; Han, D.; Qiu, T.; Chu, P. K. Aluminum Plasmonic Photocatalysis. *Sci. Rep.* **2015**, *5*, 15288.

(20) Murthy, S. K. Nanoparticles in Modern Medicine: State of the Art and Future Challenges. *Int. J. Nanomedicine* **2007**, *2*, 129-141.

(21) Jain, P. K.; Huang, X.; El-Sayed, I. H.; El-Sayed, M. A. Noble Metals on the Nanoscale: Optical and Photothermal Properties and Some Applications in Imaging, Sensing, Biology, and Medicine. *Acc. Chem. Res.* **2008**, *41*, 1578-1586.

(22) Schatz, G. C.; Van Duyne, R. P. Electromagnetic Mechanism of Surface-Enhanced Spectroscopy. In *Handbook of Vibrational Spectroscopy*; John Wiley & Sons, Ltd: 2006.

(23) Bukasov, R.; Shumaker-Parry, J. S. Silver Nanocrescents with Infrared Plasmonic Properties As Tunable Substrates for Surface Enhanced Infrared Absorption Spectroscopy. *Anal. Chem.* **2009**, *81*, 4531-4535.

(24) Brown, L. V.; Yang, X.; Zhao, K.; Zheng, B. Y.; Nordlander, P.; Halas, N. J. Fan-Shaped Gold Nanoantennas above Reflective Substrates for Surface-Enhanced Infrared Absorption (SEIRA). *Nano Lett.* **2015**, *15*, 1272-1280.

(25) Stiles, P. L.; Dieringer, J. A.; Shah, N. C.; Van Duyne, R. P. Surface-Enhanced Raman

Spectroscopy. *Annu. Rev. Anal. Chem.* **2008**, *1*, 601-626.

(26) Wustholz, K. L.; Henry, A.-I.; McMahon, J. M.; Freeman, R. G.; Valley, N.; Piotti, M. E.; Natan, M. J.; Schatz, G. C.; Duyne, R. P. V. Structure−Activity Relationships in Gold Nanoparticle Dimers and Trimers for Surface-Enhanced Raman Spectroscopy. *J. Am. Chem. Soc.* **2010**, *132*, 10903-10910.

(27) Kühler, P.; Roller, E.-M.; Schreiber, R.; Liedl, T.; Lohmüller, T.; Feldmann, J. Plasmonic DNA-Origami Nanoantennas for Surface-Enhanced Raman Spectroscopy. *Nano Lett.* **2014**, *14*, 2914-2919.

(28) Jha, S. K.; Ahmed, Z.; Agio, M.; Ekinci, Y.; Löffler, J. F. Deep-UV Surface-Enhanced Resonance Raman Scattering of Adenine on Aluminum Nanoparticle Arrays. *J. Am. Chem. Soc.* **2012**, *134*, 1966-1969.

(29) McMahon, J. M.; Schatz, G. C.; Gray, S. K. Plasmonics in the Ultraviolet with the Poor Metals Al, Ga, In, Sn, Tl, Pb, and Bi. *Phys. Chem. Chem. Phys.* **2013**, *15*, 5415-5423.

(30) Sanz, J. M.; Ortiz, D.; Alcaraz de la Osa, R.; Saiz, J. M.; González, F.; Brown, A. S.; Losurdo, M.; Everitt, H. O.; Moreno, F. UV Plasmonic Behavior of Various Metal Nanoparticles in the Near- and Far-Field Regimes: Geometry and Substrate Effects. *J. Phys. Chem. C* **2013**, *117*, 19606-19615.

(31) Sigle, D. O.; Perkins, E.; Baumberg, J. J.; Mahajan, S. Reproducible Deep-UV SERRS on Aluminum Nanovoids. *J. Phys. Chem. Lett.* **2013**, *4*, 1449-1452.

(32) Norek, M.; Włodarski, M.; Stępniowski, W. J. Tailoring of UV/violet Plasmonic Properties in Ag, and Cu Coated Al Concaves Arrays. *Appl. Surf. Sci.* **2014**, *314*, 807-814.

(33) Rodriguez, M.; Furse, C.; Shumaker-Parry, J. S.; Blair, S. Scaling the Response of Nanocrescent Antennas into the Ultraviolet. *ACS Photonics* **2014**, *1*, 496-506.

(34) Kanagasundar, A.; Xiaojin, J.; Steve, B.; Ajay, N.; Sivaraman, G. Mg Thin Films with Al Seed Layers for UV Plasmonics. *J. Phys. D: Appl. Phys.* **2015**, *48*, 184009.

(35) Kumamoto, Y.; Taguchi, A.; Honda, M.; Watanabe, K.; Saito, Y.; Kawata, S. Indium for Deep-Ultraviolet Surface-Enhanced Resonance Raman Scattering. *ACS Photonics* **2014**, *1*, 598-603.

(36) Appusamy, K.; Blair, S.; Nahata, A.; Guruswamy, S. Low-Loss Magnesium Films for Plasmonics. *Mat. Sci. Eng. B-Solid* **2014**, *181*, 77-85.

(37) Langhammer, C.; Schwind, M.; Kasemo, B.; Zorić, I. Localized Surface Plasmon Resonances in Aluminum Nanodisks. *Nano Lett.* **2008**, *8*, 1461-1471.

(38) Jérôme, M.; Jérôme, P. Fabrication of Aluminium Nanostructures for Plasmonics. *J.*

Phys. D: Appl. Phys. **2015**, *48*, 184002.

(39) Suh, J. Y.; Odom, T. W. Nonlinear Properties of Nanoscale Antennas. *Nano Today* **2013**, *8*, 469-479.

(40) Novotny, L.; Bian, R. X.; Xie, X. S. Theory of Nanometric Optical Tweezers. *Phys. Rev. Lett.* **1997**, *79*, 645-648.

(41) Jain, P. K.; El-Sayed, M. A. Plasmonic Coupling in Noble Metal Nanostructures. *Chem. Phys. Lett.* **2010**, *487*, 153-164.

(42) Nordlander, P.; Oubre, C.; Prodan, E.; Li, K.; Stockman, M. I. Plasmon Hybridization in Nanoparticle Dimers. *Nano Lett.* **2004**, *4*, 899-903.

(43) Muskens, O. L.; Giannini, V.; Sánchez-Gil, J. A.; Gómez Rivas, J. Optical Scattering Resonances of Single and Coupled Dimer Plasmonic Nanoantennas. *Opt. Express* **2007**, *15*, 17736-17746.

(44) Turkevich, J.; Stevenson, P. C.; Hillier, J. A Study of the Nucleation and Growth Processes in the Synthesis of Colloidal Gold. *Discuss. Faraday Soc.* **1951**, *11*, 55-75.

(45) Tao, A.; Sinsermsuksakul, P.; Yang, P. Polyhedral Silver Nanocrystals with Distinct Scattering Signatures. *Angew. Chem. Int. Ed. Engl.* **2006**, *45*, 4597-4601.

(46) McClain, M. J.; Schlather, A. E.; Ringe, E.; King, N. S.; Liu, L.; Manjavacas, A.; Knight, M. W.; Kumar, I.; Whitmire, K. H.; Everitt, H. O.; Nordlander, P.; Halas, N. J. Aluminum Nanocrystals. *Nano Lett.* **2015**, *15*, 2751-2755.

(47) Knight, M. W.; King, N. S.; Liu, L.; Everitt, H. O.; Nordlander, P.; Halas, N. J. Aluminum for Plasmonics. *ACS Nano* **2013**, *8*, 834-840.

(48) Knight, M. W.; Liu, L.; Wang, Y.; Brown, L.; Mukherjee, S.; King, N. S.; Everitt, H. O.; Nordlander, P.; Halas, N. J. Aluminum Plasmonic Nanoantennas. *Nano Lett.* **2012**, *12*, 6000-6004.

(49) Wen, F.; Zhang, Y.; Gottheim, S.; King, N. S.; Zhang, Y.; Nordlander, P.; Halas, N. J. Charge Transfer Plasmons: Optical Frequency Conductances and Tunable Infrared Resonances. *ACS Nano* **2015**, *9*, 6428-6435.

(50) Olivier, S.; Konstantins, J.; Ivan, S.; Christian, H.; Urs, S.; Gian-Luca, B. Helium Focused Ion Beam Fabricated Plasmonic Antennas with Sub-5 nm Gaps. *Nanotechnology* **2013**, *24*, 395301.

(51) Schade, M.; Fuhrmann, B.; Bohley, C.; Schlenker, S.; Sardana, N.; Schilling, J.; Leipner, H. S. Regular Arrays of Al Nanoparticles for Plasmonic Applications. *J. Appl. Phys.* **2014**, *115*, 084309.

(52) Haynes, C. L.; Van Duyne, R. P. Nanosphere Lithography: A Versatile Nanofabrication Tool for Studies of Size-Dependent Nanoparticle Optics. *J. Phys. Chem. B* **2001**, *105*, 5599-5611.

(53) Shumaker-Parry, J. S.; Rochholz, H.; Kreiter, M. Fabrication of Crescent-Shaped Optical Antennas. *Adv. Mater.* **2005**, *17*, 2131-2134.

(54) Chen, K.; Rajeeva, B. B.; Wu, Z.; Rukavina, M.; Dao, T. D.; Ishii, S.; Aono, M.; Nagao, T.; Zheng, Y. Moiré Nanosphere Lithography. *ACS Nano* **2015**, *9*, 6031-6040.

(55) Aizpurua, J.; Hanarp, P.; Sutherland, D. S.; Käll, M.; Bryant, G. W.; García de Abajo, F. J. Optical Properties of Gold Nanorings. *Phys. Rev. Lett.* **2003**, *90*, 057401.

(56) Chan, G. H.; Zhao, J.; Hicks, E. M.; Schatz, G. C.; Van Duyne, R. P. Plasmonic Properties of Copper Nanoparticles Fabricated by Nanosphere Lithography. *Nano Lett.* **2007**, *7*, 1947-1952.

(57) Chan, G. H.; Zhao, J.; Schatz, G. C.; Duyne, R. P. V. Localized Surface Plasmon Resonance Spectroscopy of Triangular Aluminum Nanoparticles. *J. Phys. Chem. C* **2008**, *112*, 13958-13963.

(58) Haynes, C. L.; McFarland, A. D.; Smith, M. T.; Hulteen, J. C.; Van Duyne, R. P. Angle-Resolved Nanosphere Lithography: Manipulation of Nanoparticle Size, Shape, and Interparticle Spacing. *J. Phys. Chem. B* **2002**, *106*, 1898-1902.

(59) Haynes, C. L.; Van Duyne, R. P. Dichroic Optical Properties of Extended Nanostructures Fabricated Using Angle-Resolved Nanosphere Lithography. *Nano Lett.* **2003**, *3*, 939-943.

(60) Hulteen, J. C.; Van Duyne, R. P. Nanosphere Lithography: A Materials General Fabrication Process for Periodic Particle Array Surfaces. *J. Vac. Sci. Technol. A* **1995**, *13*, 1553-1558.

(61) Fredriksson, H.; Alaverdyan, Y.; Dmitriev, A.; Langhammer, C.; Sutherland, D. S.; Zäch, M.; Kasemo, B. Hole–Mask Colloidal Lithography. *Adv. Mater.* **2007**, *19*, 4297-4302.

(62) Zorić, I.; Zäch, M.; Kasemo, B.; Langhammer, C. Gold, Platinum, and Aluminum Nanodisk Plasmons: Material Independence, Subradiance, and Damping Mechanisms. *ACS Nano* **2011**, *5*, 2535-2546.

(63) Sterl, F.; Strohfeldt, N.; Walter, R.; Griessen, R.; Tittl, A.; Giessen, H. Magnesium as Novel Material for Active Plasmonics in the Visible Wavelength Range. *Nano Lett.* **2015**, *15*, 7949-7955.

(64) Swartz, M.; Rodriguez, M.; Quast, A. D.; Cooper, C. T.; Blair, S.; Shumaker-Parry, J.

S. Aluminum Nanocrescent Plasmonic Antennas Fabricated by Copper Mask Nanosphere Template Lithography. *J. Phys. Chem. C* **2016**, *120*, 20597-20603.

(65) Cooper, C. T.; Rodriguez, M.; Blair, S.; Shumaker-Parry, J. S. Mid-Infrared Localized Plasmons through Structural Control of Gold and Silver Nanocrescents. *J. Phys. Chem. C* **2015**, *119*, 11826-11832.

CHAPTER 2

ALUMINUM NANOCRESCENT PLASMONIC ANTENNAS FABRICATED BY COPPER MASK NANOSPHERE TEMPLATE LITHOGRAPHY

Adapted from Swartz, M; Rodriguez, M.; Quast, A.; Cooper, C. T.; Blair, S.; Shumaker-Parry, J. S. *J. Phys. Chem. C.* **2016**, DOI 10.1021/acs.jpcc.6b00396, Copyright 2016, American Chemical Society. The first author conducted all experimental and characterization work reported except as indicated. Rodriguez, M. conducted all theoretical simulations. Quast, A. acquired and aided in the interpretation of the high-resolution scanning transmission electron microscopy (HR-S/TEM) images presented in Figure 2.5.

2.1 Introduction

Engineering plasmonic nanostructures for controlled light-matter interactions is essential for optimizing plasmonic systems for applications in enhanced spectroscopy, chemical and biological sensing, photovoltaics, photocatalysis, and subwavelength and nonlinear light guiding.[1-8] Aluminum as a plasmonic material exhibits optical and material properties that are advantageous as compared to the more typically used gold, silver, and copper.[9-21] Aluminum supports plasmon resonances on either side of its interband transition at 800 nm and demonstrates favorable plasmonic properties in the ultraviolet

(UV) spectral region.[22] While silver has a short wavelength interband transition relative to gold (310 nm and 500 nm, respectively), it is incapable of supporting a plasmon below this wavelength.[22] Another practical drawback of silver is that it readily oxidizes, leading to a deterioration of plasmonic behavior over time. Copper has an interband transition at 590 nm and oxidizes even more rapidly than silver.[23] While aluminum also undergoes rapid oxidation, the oxide formation is self-limiting at ~3 nm and acts as a passivating layer that protects and preserves the metal underneath.[11] The natural abundance of aluminum also is attractive for applications that require large-scale plasmonic systems integration, such as in high surface area photovoltaic systems or as active coatings for plasmon-assisted photocatalysis for chemical transformations and degradation processes. For aluminum to be adopted in commercial applications, fabrication techniques that enable large-scale production of aluminum nanostructures are required. While there are many approaches to nanostructure gold and silver, the robust oxide layer inherent to aluminum often presents a challenge in applying these fabrication methods to aluminum.

Both top-down and bottom-up strategies have been used to fabricate aluminum plasmonic antennas.[24] One approach that combines these two strategies for antenna fabrication is nanosphere lithography (NSL). This process uses close-packed polystyrene (PS) nanospheres on a surface to produce nanostructures of gold, silver, aluminum and other materials. The advantages of NSL are largely the scalability, low-cost, and versatility in the size and shapes of particles that can be fabricated.[25-27] Pioneering work by Van Duyne and co-workers have demonstrated the versatility of NSL by altering the metal deposition angle to prepare metal nanotriangles with different aspect ratios and as well as chains of nanotriangles with varying degrees of overlap.[28, 29] As this technique is

compatible with a variety of metals including silver, gold, copper, and aluminum, plasmon resonances can be tuned throughout the near-infrared (NIR), visible and UV spectral regions.[9, 23, 30, 31] NSL has been successful at producing aluminum nanotriangle arrays over large substrate areas.[9] However NSL can only produce a limited number of shapes at a fixed filling fraction.[31]

Nanosphere template lithography (NTL) is a modification of NSL that offers significant control over the size, shape, and surface density of particles. NTL also uses nanometer sized PS beads, but in NTL each bead serves as a template for an individual nanostructure.[32, 33] For NTL, the PS beads can be deposited in either a close-packed monolayer or as a dispersed submonolayer over virtually any flat surface. This fabrication method has been used to produce plasmonic ring, disk, and crescent shaped structures of gold and silver over large substrate areas with nanometer resolution.[32-34] These particles act as plasmonic nanoantennas, concentrating and amplifying the electric field component of the incident plane wave in the near field of the nanostructure. One of the challenges of NTL is the reliance on a directional etch step which can be challenging for metals that form a passivating oxide layer such as aluminum. This etching step is especially important to fabricate more complex structures such as nanocrescents in order to achieve control of the localized surface plasmon resonance (LSPR) response for specific applications.[34-36] Here we demonstrate fabrication of aluminum plasmonic antennas by incorporating a sacrificial copper mask in a simple, scalable templating process that enables control of nanostructure shape. The aluminum nanocrescent antennas exhibit multimodal plasmon resonances that can be tuned from NIR into the UV by controlling the template size.

2. 2 Materials and Methods

Copper (99.999%) and aluminum (99.999%), were purchased from K. J. Lesker (Philadelphia, PA). Polystyrene microspheres were purchased from Polysciences, Inc. (Warrington, PA). Fused quartz microscopes slides were purchased from Technical Glass Products (Painesville Twp, OH). All water used for substrate preparation was purified to 18 MΩ with a Barnstead NANOpure diamond system.

Fused quartz microscope slides were used as substrates and were cleaned by immersion in piranha acid (3:1 volume ratio of H_2SO_4: 30% H_2O_2) for 45 min. Slides were rinsed three times with nanopure water then sonicated for 60 min in 5:1:1 volume ratio H_2O: NH_4OH: 30% H_2O_2 at 60 ºC. Slides were rinsed three times with nanopure water and stored for up to one week in nanopure water or rinsed with absolute ethanol, dried with nitrogen, and used immediately. (Caution: Piranha solution is a strong oxidizing agent, which has been known to detonate spontaneously upon contact with organic material, and should be handled with extreme care.)

AlNCs were fabricated on clean fused quartz slides using copper mask nanosphere template lithography (NTL). Polystyrene microspheres were diluted to 0.05% (82±6.0 and 120±6.9 nm templates) or 0.15% (450±8 nm templates) by volume in absolute ethanol and spin coated onto dried fused quartz slides. For the 450 nm PS templates, a 50 nm film of copper metal was deposited at a rate of 1.0 Å/s onto the fused quartz substrates using an electron-beam evaporator (Denton SJ20C, Denton Vacuum USA, Moorestown, NJ). Recent publications have outlined the benefits of depositing at higher rates, however, strong LSPR resonances are still observed for Al films deposited at slower rates that enable better thickness control for thin nanostructures.[37] A 35 nm copper film was deposited for

the smaller 82 nm templates. Copper films were deposited normal (450 nm PS) to the surface and at 40˚ (82 and 120 nm PS) relative to surface normal. The substrates were then rotated 180˚ and placed on sample mounts tilted 40˚ relative to surface normal and a 25 nm aluminum film was deposited at a rate of 1.0 Å/s. Film thickness and deposition rate were monitored using a quartz crystal microbalance (XPC2, Inficon, East Syracuse, NY). The copper film was removed by quickly dipping substrates in concentrated nitric acid for 1-10 s. The aluminum film that was deposited on top of the copper was subsequently removed by sonicating the substrates in nanopure water for 5-10 min. If any aluminum film remained after sonication it was removed using tape.

AlNCs were imaged using scanning electron microscopy (FEI Nova Nano 630) in immersion mode with a Helix detector. Optical extinction measurements were collected from 200-2500 nm using a Perkin-Elmer 750 UV/Vis/Near-IR spectrophotometer with a beam probe size of 2 cm x 0.5 cm. Polarized extinction spectra were limited to wavelengths above 300 nm due to the limited transmission of the polarizer. Collection of polarized spectra are detailed elsewhere.[36]

HAADF, SE, and EDS images were collected using a JEOL-2800 S/TEM equipped with ultrafast EDS and the following settings: 1.0 nm probe size, a camera length corresponding to a detector semiangle of 62.1 mrad, and a Schottky-Type hot field emission gun (FEG) source operating at an accelerating voltage of 200 kV. The dual 100 mm^2 EDS detectors have a combined solid angle collection efficiency was 1.9 sr. The spectral regions used for mapping and quantitation were 1409-1563 and 466-584 eV for the Al and O K-lines, respectively. EDS maps shown as net counts were processed using a Kernel size of 19X19 and the Cliff-Lorimer correction method without absorbance

correction in the Thermo Scientific NORAN spectral suite (NSS 3.2). For TEM analysis AlNCs were fabricated on ultrathin carbon film on lacey carbon support film 300 mesh gold grids (Ted Pella). These AlNCs were fabricated using 505 nm PS templates with a 200 nm Cu layer and a 100 nm Al layer deposited at 10 Å/s. A faster deposition rate was used with the expectation of producing lower levels of oxidation in the bulk film, limiting oxidation to the outer layer.[37] The thicker Al layer allowed for better contrast between the Al and O in EDS mapping.

The simulations were performed using FDTD Solutions version 8.9.150 from Lumerical Solutions, Inc. The simulations were carried out on a Windows XP, 64 bit system equipped with an Intel Xeon E5520 CPU 2.26GHz, and 12 GB of RAM. The index of refraction used for aluminum and glass were fitted material properties to Palik values over the wavelength range of interest (300nm-2500nm).[38] A mesh resolution of 1nm was used in each direction of a three dimensional simulation setup.[39]

2.3 Results and Discussion

Aluminum nanocrescents (AlNCs) were fabricated over large areas by incorporation of a sacrificial copper layer in the NTL process. In contrast to the use of NSL for aluminum nanotriangles, each PS nanosphere acts as a template for a single plasmonic nanostructure in NTL. The fabrication of AlNCs is outlined in Figure 2.1A. First, PS nanospheres are deposited on a clean fused quartz substrate (Figure 2.1A I). Next, a sacrificial copper film deposited at an angle results in an elliptical shadow where the substrate is exposed (Figure 2.1A II). The deposition of aluminum from the opposing angle fills in the shadow left by the copper (Figure 2.1A III). The PS template defines the inner backbone of the nanocrescent preventing the formation of an elliptical particle. The

sacrificial layer is removed by submersing the substrate in concentrated nitric acid which quickly dissolves the copper film but leaves the aluminum intact (Figure 2.1A IV). The bulk aluminum film is removed by sonication in water, while the aluminum that is in direct contact with the substrate remains attached (Figure 2.1A V). By using a sacrificial copper layer, the bulk aluminum film can be removed without the use of argon ion milling, which damages the templates while the oxide film is removed. This preserves the PS templates throughout the process resulting in well-defined, crescent-shaped structures (Figure 2.1B).

Using the copper mask NTL process, AlNCs with polarization-dependent plasmon responses were reproducibly fabricated over the entire substrate area. Figure 2.1B shows a scanning electron microscopy (SEM) image of AlNCs fabricated using 450 nm PS templates. In order to minimize aggregation of the templates, a relatively low surface coverage has been used for the proof of principle demonstration of this modified version of NTL for preparing Al nanostructures. Ultimately, surface coverage of the AlNCs is controlled through the concentration of the PS nanosphere solution, and several publications have demonstrated methods to increase the density of PS nanospheres on a surface.[11, 32, 40] The template size determines the tip to tip distance of the resulting AlNC and the outer and inner diameters are controlled by the angles of Cu and Al deposition, respectively. While the SEM image depicts a relatively small area, the resulting particles have uniform size and orientation over the entire substrate (6.45 cm^2). The uniform orientation of the particles is evident by the polarization dependence of the LSPR response measured using UV/Vis spectroscopy (Figure 2.1C). The probe beam spot size is 1 cm^2 and even with such a large probe area the polarization-dependent plasmonic response of the AlNCs is preserved. When the electric field of the incident light is polarized along the

short axis of the nanocrescent (Figure 2.1C top) there is a coherent oscillation of electrons from the tips to the backbone.[36] By polarizing light along this axis, a dipole resonance is observed at 1200 nm. Rotating the incident light polarization 90˚ aligns the electric field with the long axis of the nanocrescent (Figure 2.1C bottom). This induces electrons to oscillate between the tips resulting in a dipole resonance at 2100 nm. Due to the limited symmetry and uniform orientation of the particles, it is possible to selectively excite multiple plasmon modes from an ensemble of similarly sized particles. Finite difference time domain (FDTD) simulations predict the polarization-dependent response of an individual AlNC. Based on previous theoretical work, the impact on the far field LSPR response is expected to be minimal. Besides a small modification of the wavelength position of the resonance due to the change in the local dielectric environments, so the oxide layer was not included in the model.[38] The short and long axis dipole resonances are in close agreement to the experimental spectra, with the long axis dipole in the simulation having a slight blue shift from the optical response of the fabricated structures. The simulations show the interband transition having a larger contribution than what is observed experimentally. Higher order modes for both long and short axis excitations are seen around 500 nm and are attributed to quadrupole resonances. The short axis quadrupole resonance is slightly blue-shifted from what the simulations predict while the long axis quadrupole overlaps very well with the response predicted by simulations.

Further tuning of the LSPR wavelength is achieved by changing the diameter of the PS templates.[35] Due to the dielectric properties of aluminum, the nanostructures are capable of supporting plasmon resonances on either side of the material's 800 nm interband transition. Here we take advantage of this property through the use of 82 nm

PS templates which result in AlNCs of similar size. Figure 2.2 presents the spectral response and SEM images of these small AlNCs. The short axis dipole resonance is situated at 375 nm (Figure 2.2A) while the long axis dipole resonance lies in the visible region at 500 nm (Figure 2.2B). The experimental spectra exhibit broadened LSPR peaks as compared to their simulated counterparts. This broadening is expected to be in part a result of a distribution of AlNC diameters that stems from variations in the template size. In addition, the model used for the simulations cannot capture all of the details of the complex nanocrescent features, so the structural properties such as grain boundaries or specific local features can also contribute to a more broadened response compared to that predicted from the model.

Previously published computational simulations of AlNCs predict higher order plasmon modes located farther into the UV region.[39] However, due to the limited transmission of the polarizer between 200-300 nm, those modes are not observed in these experiments. SEM images of the nanostructures show that the general crescent shape is preserved at this small template size (Figure 2.2C). While the tips of the structures appear dulled in comparison to the nanocrescents from 450nm templates, the radius of curvature is ~5 nm for both sizes. Again, FDTD simulations are in general agreement with both of the experimentally observed short and long axis dipole resonances. As the experimental setup was limited to wavelengths above 300 nm, simulations were not performed at the shorter UV wavelengths either. Previous simulations based on small model nanocrescent structures predicted plasmon resonances in the lower UV spectral region.[39]

The copper mask NTL is also useful for the fabrication of a range of different sized AlNCs. The compatibility of the fabrication approach with other plasmonic metals is also

demonstrated. Figure 2.3 presents a comparison of aluminum and gold nanocrescents (AuNCs) fabricated using sacrificial layer NTL. Short axis dipole (Figure 2.3A) and long axis dipole (Figure 2.3B) plasmon resonances for AlNCs are blue-shifted compared to AuNCs of similar diameter and aspect ratio. While these plots show a linear dependence of the LSPR wavelength on the particle diameter, Au particles are not able to support a plasmon below the interband transition around 500 nm. However, Al can support a UV plasmon resonance and can do so with relatively large template diameters.

The near-field enhancement maps of UV/Vis resonant AlNCs were modeled using Lumerical (Figure 2.4). Figure 2.4B shows the experimental and simulated UV/Vis spectra of AlNCs under excitation with polarization along the AlNC short axis. A near-field intensity map for 432 nm light polarized along the short axis of a 120 nm template AlNC is shown in Figure 2.4D. Regions of electromagnetic field enhancements are localized at the tips and along the backbone, consistent with electrons oscillating from the tips to the backbone when light is polarized along the short axis. Simulations and experimental data for light polarized along the long axis of the AlNCs are shown in Figure 2.4C. A dipole mode resonance is observed at 650 nm and a higher order quadrupole resonance mode is present at 325 nm. Figure 2.4E shows the near-field intensity map for 653 nm light polarized along the long axis. In contrast to the short axis dipole resonance, this long axis dipole shows enhancement primarily along the outside of the tips. This is consistent with electrons oscillating between the tips of the AlNCs. The field intensity map for a 120 nm AlNC interrogated with 325 nm light polarized along the long axis is shown in Figure 2.4F. This long axis quadrupole mode also exhibits electric field enhancement at the tips of the structure and at a similar magnitude. As this is a quadrupole mode, the intensity decays

much more rapidly than the two dipole modes. For all excitation geometries, large field enhancements are predicted at the tips of the structures which is consistent with previous simulations.[36, 39]

The oxide thickness was characterized using transmission electron microscopy (TEM) and energy-dispersive X-ray spectroscopy (EDS). Previous work characterizing the oxide layer thickness has involved only bulk type measurements using X-ray photoelectron spectroscopy (XPS) on thin films of aluminum.[11] Indirect methods, such as modelling the LSPR shift with increasing oxide thickness or doping the Al film with oxygen, have also been used to characterize the oxide thickness.[10] The combination of high-resolution imaging and spatially-resolved chemical mapping provides a direct measurement the oxide layer formed on individual AlNCs.

AlNCs were fabricated on gold TEM grids and imaged with high-resolution scanning TEM (S/TEM) and EDS (Figure 2.5). By imaging backscattered secondary electrons (Figure 2.5A), much greater detail is achieved than conventional SEM imaging.[41] At this resolution, the roughened surface of the AlNCs due to heterogeneous film growth is clearly visible. Additionally, this resolution confirms the 5 nm tip radius of curvature from the SEM images. This measurement is taken as an average of several structures, while the HAADF image in Figure 2.5 B shows a smaller radius of curvature, on average the tip radius comes out to around 5 nm. While these images have excellent surface detail, they also reveal the complications in analyzing the oxide layer present on the AlNCs.

High angle annular dark-field (HAADF) S/TEM images (Figure 2.5B) are uniquely dependent on atomic z-contrast, easily distinguishing between Al and Al_2O_3. The reduced relative concentration of Al in the oxide layer versus the pure metal NC region leads to a

thinner profile in the HAADF image when compared to either the SE image or the Al EDS map. Because z-contrast images are entirely dependent on relative scattering efficiencies in regions of constant thickness, the core close-packed Al atoms inside the alumina overlayer are best seen as the brighter regions in the HAADF image. The relative scattering efficiencies of Al to Al_2O_3 differ by a factor of ~1.6 meaning the Al_2O_3 region is only two-thirds the brightness of the Al region. This observation is important for properly understanding the plasmonic structure of these AlNCs because only the core metallic aluminum structure is capable of supporting surface plasmons that give rise to optical near field enhancements and the unavoidable oxide layer merely serves to potentially attenuate or at least modulate these fields.[39]

EDS mapping of characteristic K-line X-ray transitions of Al (Figure 2.5C) and O (Figure 2.5D) were used as a means of directly measuring the oxide layer thickness. Al is observed across the entire structure with higher concentrations in the thicker backbone. This is expected given the sloped shape of the structures observed in the SE-S/TEM images. The concentration gradient of O (Figure 2.5D) yields substantial information on the spatial distribution of the oxide layer. The overall concentration of O is much lower than Al in the bulk of the AlNC, which is composed primarily of packed Al metal. In contrast, the EDS map of O appears much more heterogeneous than that of Al. This is because O is mostly confined to the final exposed surface of rapidly deposited Al structures. The increased surface roughness seen in Figure 2.5A leads to a greater exposed surface area and therefore a much more surface structure dependent O map. Where there are grains or inhomogeneity on the surface, the concentration of O increases due to the amount of oxide in the z-direction. This is evident along the outside of the AlNC as there

is a distinct oxygen signature around the entire particle. This outside border is used to directly measure the thickness of the oxide layer of the particle. This region of the nanoparticle is more likely to have a sharp, vertical edge that extends up in the z-direction making for a more accurate oxide thickness measurement.

In order to better estimate the thickness of the oxide layer in the EDS maps, the intensity of the aluminum and oxygen peaks through a slice of the crescent are plotted (Figure 2.5E) as indicated by the arrows in Figures 2.5A-D. For an accurate measure of the oxide layer, attention was given to the outside edge of the AlNC backbone where there is a vertical edge. A sloping edge is avoided as that would broaden the resulting oxide measurement. This region is enlarged in Figure 2.5E, and a distinct region around 65 nm where there is a spike in the O content is clearly visible. As a guide to the eye, this region is highlighted by two black lines, which correspond to the start of the oxide layer and the location of maximum intensity. The distance between these two lines is 3 nm, which is in agreement with previous measurements of the oxide thickness of aluminum.[11] Furthermore, we expect the true oxide thickness to be slightly less than 3 nm because these data are a convolution of the chosen S/TEM probe of 1.0 nm and the true spatial distribution of the concentration of O along the chosen path. This analysis also confirms that the nitric acid treatment used in this modified copper mask NTL process did not produce a thicker than expected oxide layer

2.4 Conclusions

In conclusion, a modified version of NTL enables the fabrication of AlNC antennas with highly tunable LSPR responses. This fabrication method eliminates the need for etching the aluminum film through the use of a sacrificial copper mask. The resulting

AlNCs exhibit multimodal, polarization-dependent plasmon resonances in the UV, visible, and near-infrared regions of the spectrum. Current research is focused on probing the utility of these crescent-shaped particles at long and short wavelengths. At short wavelengths, the AlNCs may have applications in plasmon-enhanced fluorescence spectroscopy and resonance Raman scattering spectroscopy. At longer wavelengths, these particles are expected to be applicable in refractive index sensing and surface-enhanced infrared absorption spectroscopy. Simple variations of the copper mask NTL method, such as removing the PS templates before aluminum deposition, can be used to produce structures with a variety of shapes composed of different metals. Direct determination of the oxide overlayer is essential to understanding the spatial relationship of the optical near-field and molecules of interest in sensing platforms. Future work using electron energy loss spectroscopy (EELS) and aberration-corrected S/TEM should allow for complete deconvolution of instrumental errors in mapping and lead to a subangstrom determination of oxide overlayers.

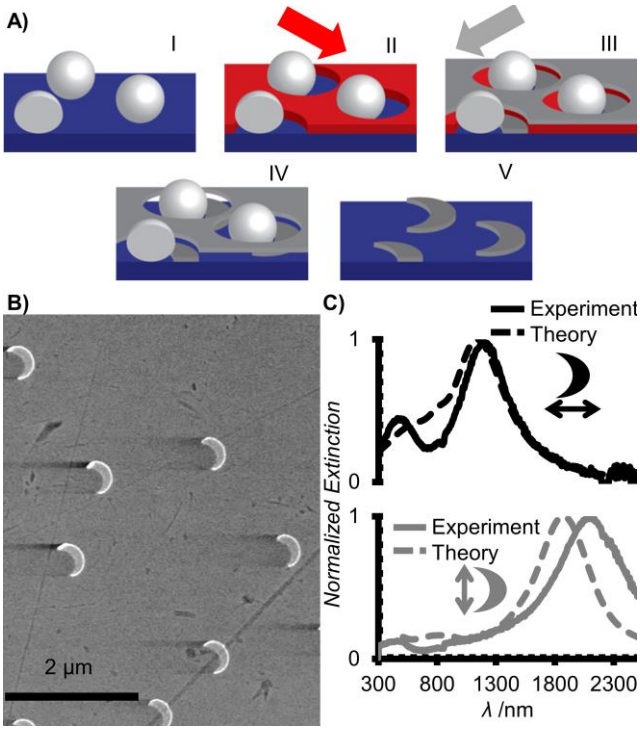

Figure 2.1 Overview of copper mask NTL and characterization of fabricated Al nanocrescents based on electron microscopy and optical response analyses. A) Cartoon showing the fabrication of aluminum plasmonic antennas using NTL and a sacrificial Cu mask. I-PS beads are deposited on a fused quartz substrate via spin coating, II-angled deposition of a Cu sacrificial layer (30-50 nm), III-angled deposition of Al from opposing direction (25 nm), IV-removal of Cu mask with concentrated nitric acid, V-PS templates and Al film removed by sonicating substrates in water. B) SEM image of 450 nm AlNCs on fused quartz. C) UV/Vis/NIR extinction spectra of 450 nm AlNCs (solid) and FDTD simulated spectra (dotted) with arrows denoting the polarization of the incident electric field. Experimental and theoretical spectra are compared using normalized extinction values.

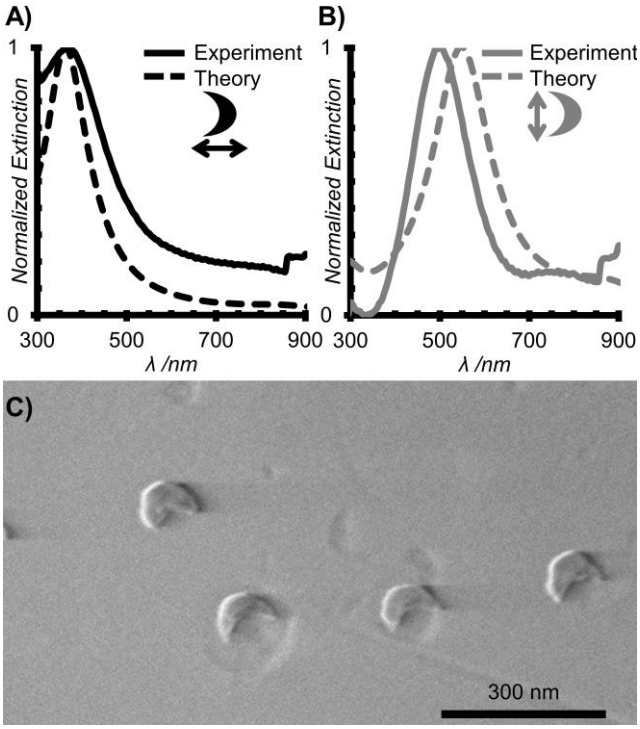

Figure 2.2 Using the modified NTL process, employing smaller PS templates produces smaller AlNCs which exhibit an LSPR response in the UV. Theoretical (dotted) and experimental (solid) UV/Vis spectra of 82 nm AlNCs with the incident electric field polarized along the short axis (A) exhibit a dipole resonance in the UV. B) Light polarized along the long axis results in a dipole resonance in the visible region. C) SEM image of 82 nm AlNCs on fused quartz.

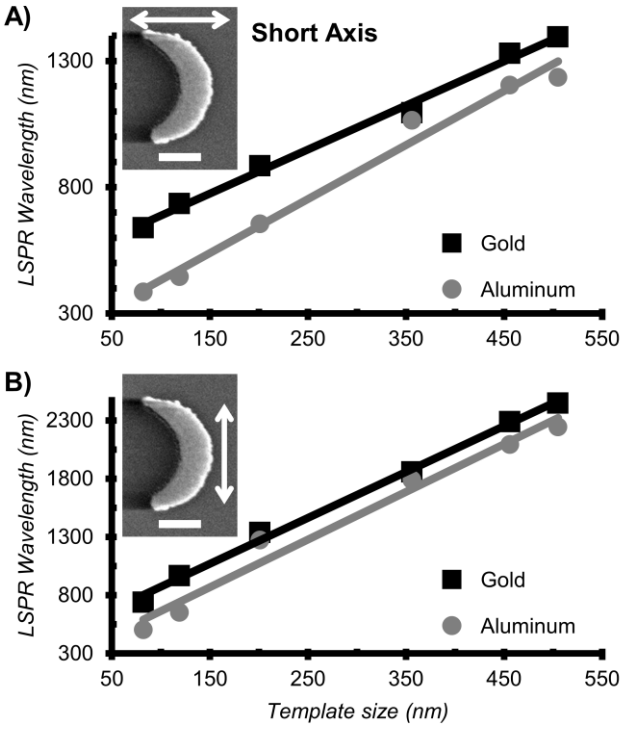

Figure 2.3 LSPR response of metal nanoparticles is dependent on particle size. Comparison of the short axis dipole (A) and long axis dipole (B) plasmon resonance modes of gold and aluminum nanocrescents fabricated using copper mask NTL. A linear regression trend line has been added for each metal. SEM inset in both panels is of a gold nanocrescent. The scale bar represents 200 nm.

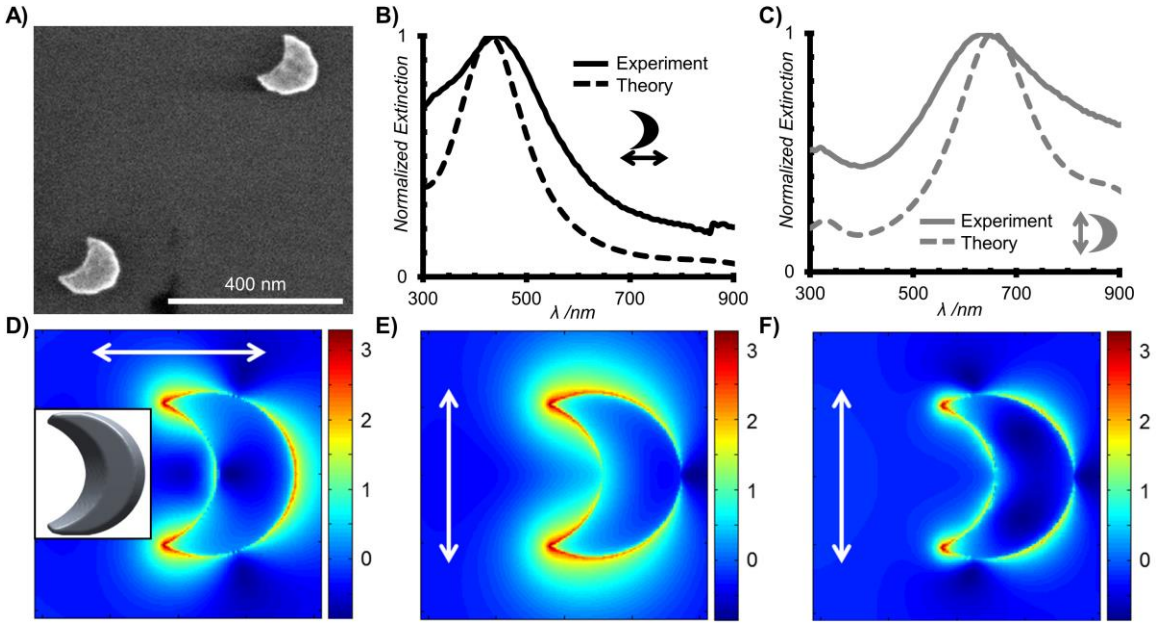

Figure 2.4 Theoretical models of AlNCs are based off of fabricated structures. A) SEM image of 120 nm diameter AlNCs fabricated using copper mask template lithography. Simulated (dotted) and experimental (solid) extinction spectra of 120 nm AlNCs with the incident electric field polarized along the short axis (B) and long axis (C). A dipole resonance is observed at 450 nm for short-axis excitation and both dipole (650 nm) and quadrupole (325 nm) resonances are observed for long-axis excitation. FDTD simulations of the electric near-field enhancement were performed at the resonance wavelength for the short axis dipole (D), long axis dipole (E), and long axis quadrupole (F). The white arrows denote the polarization of the incident electric field and the color scale represents the log of the electric field intensity, $|E|^2$.

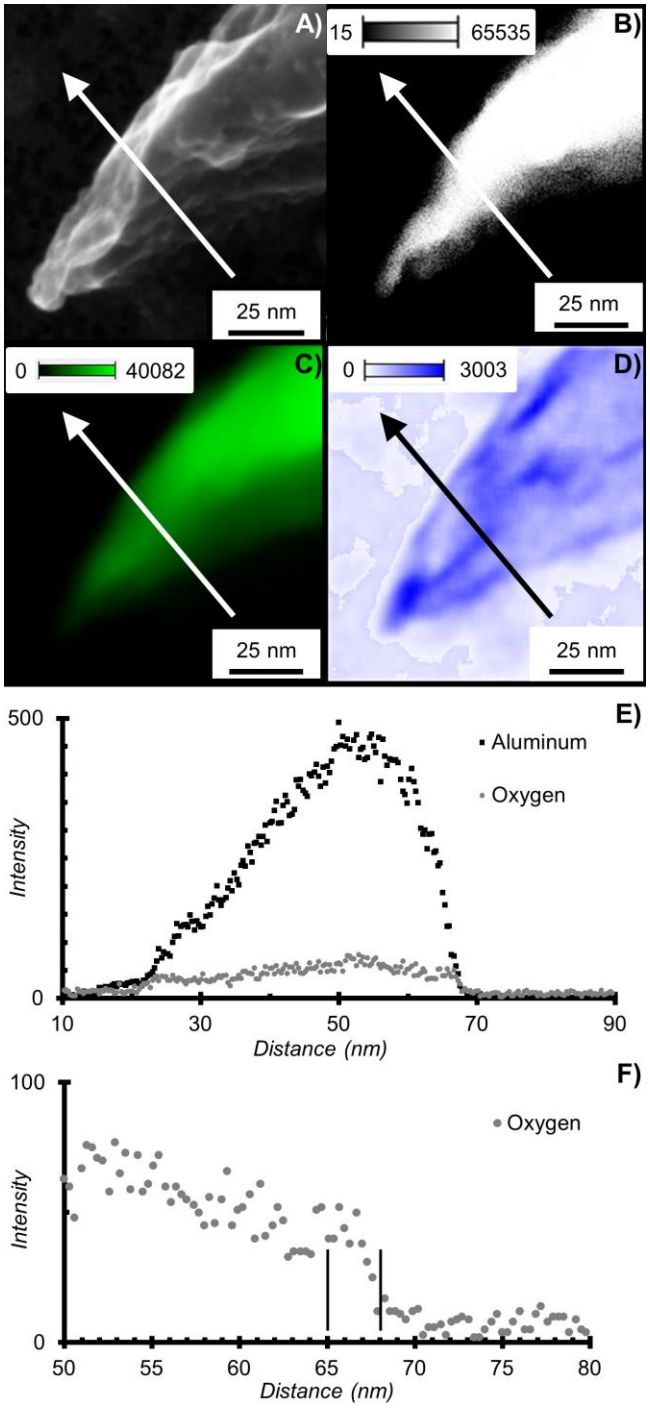

Figure 2.5 S/TEM analysis of AlNCs reveals greater topological and compositional information. A) Secondary electron S/TEM image of 100 nm thick, 500 nm diameter AlNCs. B) HAADF S/TEM shows differences in z-contrast, consequently the high density of Al appears bright. EDS mapping of the AlNCs shows the distribution of Al (C) and O (D) with color intensity corresponding to the EDS counts. E) Intensity of Al and O K peaks along the line indicated by the white (A/B) and black (C) arrows. F) Enhanced view of the outside backbone of the AlNC shows how the concentration of O changes at a vertical edge (Al data points removed for clarity). Lines indicate where oxide measurement was made.

2.5 References

(1) Li, X.; Stockman, M. I. Highly Efficient Spatiotemporal Coherent Control in Nanoplasmonics on a Nanometer-Femtosecond Scale by Time Reversal. *Phys. Rev. B* **2008**, *77*, 195109.

(2) Atwater, H. A.; Polman, A. Plasmonics for Improved Photovoltaic Devices. *Nat. Mater.* **2010**, *9*, 205-213.

(3) Chowdhury, M. H.; Ray, K.; Gray, S. K.; Pond, J.; Lakowicz, J. R. Aluminum Nanoparticles as Substrates for Metal-Enhanced Fluorescence in the Ultraviolet for the Label-Free Detection of Biomolecules. *Anal. Chem.* **2009**, *81*, 1397-1403.

(4) Mühlschlegel, P.; Eisler, H.-J.; Martin, O. J. F.; Hecht, B.; Pohl, D. W. Resonant Optical Antennas. *Science* **2005**, *308*, 1607-1609.

(5) Sagle, L. B.; Ruvuna, L. K.; Ruemmele, J. A.; Van Duyne, R. P. Advances in Localized Surface Plasmon Resonance Spectroscopy Biosensing. *Nanomedicine* **2011**, *6*, 1447-1462.

(6) Cao, J.; Sun, T.; Grattan, K. T. V. Gold Nanorod-Based Localized Surface Plasmon Resonance Biosensors: A Review. *Sens. Actuator B-Chem* **2014**, *195*, 332-351.

(7) Hutter, E.; Fendler, J. H. Exploitation of Localized Surface Plasmon Resonance. *Adv. Mater.* **2004**, *16*, 1685-1706.

(8) Castro-Lopez, M.; Brinks, D.; Sapienza, R.; van Hulst, N. F. Aluminum for Nonlinear Plasmonics: Resonance-Driven Polarized Luminescence of Al, Ag, and Au Nanoantennas. *Nano Lett.* **2011**, *11*, 4674-4678.

(9) Chan, G. H.; Zhao, J.; Schatz, G. C.; Duyne, R. P. V. Localized Surface Plasmon Resonance Spectroscopy of Triangular Aluminum Nanoparticles. *J. Phys. Chem. C* **2008**, *112*, 13958-13963.

(10) Knight, M. W.; King, N. S.; Liu, L.; Everitt, H. O.; Nordlander, P.; Halas, N. J. Aluminum for Plasmonics. *ACS Nano* **2013**, *8*, 834-840.

(11) Langhammer, C.; Schwind, M.; Kasemo, B.; Zorić, I. Localized Surface Plasmon Resonances in Aluminum Nanodisks. *Nano Lett.* **2008**, *8*, 1461-1471.

(12) McMahon, J. M.; Schatz, G. C.; Gray, S. K. Plasmonics in the Ultraviolet with the Poor Metals Al, Ga, In, Sn, Tl, Pb, and Bi. *Phys. Chem. Chem. Phys.* **2013**, *15*, 5415-5423.

(13) Olson, J.; Manjavacas, A.; Liu, L.; Chang, W.-S.; Foerster, B.; King, N. S.; Knight, M. W.; Nordlander, P.; Halas, N. J.; Link, S. Vivid, Full-Color Aluminum Plasmonic Pixels. *Proc. Natl. Acad. Sci. USA* **2014**, *111*, 14348-14353.

(14) Norek, M.; Włodarski, M.; Stępniowski, W. J. Tailoring of UV/violet Plasmonic Properties in Ag, and Cu Coated Al Concaves Arrays. *Appl. Surf. Sci.* **2014**, *314*, 807-814.

(15) Ramadurgam, S.; Lin, T.-G.; Yang, C. Aluminum Plasmonics for Enhanced Visible Light Absorption and High Efficiency Water Splitting in Core–Multishell Nanowire Photoelectrodes with Ultrathin Hematite Shells. *Nano Lett.* **2014**, *14*, 4517-4522.

(16) Martin, J.; Kociak, M.; Mahfoud, Z.; Proust, J.; Gérard, D.; Plain, J. High-Resolution Imaging and Spectroscopy of Multipolar Plasmonic Resonances in Aluminum Nanoantennas. *Nano Lett.* **2014**, *14*, 5517-5523.

(17) Knight, M. W.; Liu, L.; Wang, Y.; Brown, L.; Mukherjee, S.; King, N. S.; Everitt, H. O.; Nordlander, P.; Halas, N. J. Aluminum Plasmonic Nanoantennas. *Nano Lett.* **2012**, *12*, 6000-6004.

(18) Jha, S. K.; Ahmed, Z.; Agio, M.; Ekinci, Y.; Löffler, J. F. Deep-UV Surface-Enhanced Resonance Raman Scattering of Adenine on Aluminum Nanoparticle Arrays. *J. Am. Chem. Soc.* **2012**, *134*, 1966-1969.

(19) Xu, Q.; Liu, F.; Liu, Y.; Meng, W.; Cui, K.; Feng, X.; Zhang, W.; Huang, Y. Aluminum Plasmonic Nanoparticles Enhanced Dye Sensitized Solar Cells. *Opt. Express* **2014**, *22*, A301-A310.

(20) Yang, Z.-L.; Li, Q.-H.; Ren, B.; Tian, Z.-Q. Tunable SERS from Aluminium Nanohole Arrays in the Ultraviolet Region. *Chem. Commun.* **2011**, *47*, 3909-3911.

(21) Martin, J.; Proust, J.; Gérard, D.; Plain, J. Localized Surface Plasmon Resonances in the Ultraviolet from Large Scale Nanostructured Aluminum Films. *Opt. Mater. Express* **2013**, *3*, 954-959.

(22) Davy, G.; Stephen, K. G. Aluminium Plasmonics. *J. Phys. D: Appl. Phys.* **2015**, *48*, 184001.

(23) Chan, G. H.; Zhao, J.; Hicks, E. M.; Schatz, G. C.; Van Duyne, R. P. Plasmonic Properties of Copper Nanoparticles Fabricated by Nanosphere Lithography. *Nano Lett.* **2007**, *7*, 1947-1952.

(24) Jérôme, M.; Jérôme, P. Fabrication of Aluminium Nanostructures for Plasmonics. *J. Phys. D: Appl. Phys.* **2015**, *48*, 184002.

(25) Haynes, C. L.; Van Duyne, R. P. Nanosphere Lithography: A Versatile Nanofabrication Tool for Studies of Size-Dependent Nanoparticle Optics. *J. Phys. Chem. B* **2001**, *105*, 5599-5611.

(26) Chen, K.; Rajeeva, B. B.; Wu, Z.; Rukavina, M.; Dao, T. D.; Ishii, S.; Aono, M.; Nagao, T.; Zheng, Y. Moiré Nanosphere Lithography. *ACS Nano* **2015**, *9*, 6031-6040.

(27) Stiles, P. L.; Dieringer, J. A.; Shah, N. C.; Van Duyne, R. P. Surface-Enhanced Raman Spectroscopy. *Annu. Rev. Anal. Chem.* **2008**, *1*, 601-626.

(28) Haynes, C. L.; Van Duyne, R. P. Dichroic Optical Properties of Extended Nanostructures Fabricated Using Angle-Resolved Nanosphere Lithography. *Nano Lett.* **2003**, *3*, 939-943.

(29) Haynes, C. L.; McFarland, A. D.; Smith, M. T.; Hulteen, J. C.; Van Duyne, R. P. Angle-Resolved Nanosphere Lithography: Manipulation of Nanoparticle Size, Shape, and Interparticle Spacing. *J. Phys. Chem. B* **2002**, *106*, 1898-1902.

(30) Jensen, T. R.; Malinsky, M. D.; Haynes, C. L.; Van Duyne, R. P. Nanosphere Lithography: Tunable Localized Surface Plasmon Resonance Spectra of Silver Nanoparticles. *J. Phys. Chem. B* **2000**, *104*, 10549-10556.

(31) Hulteen, J. C.; Van Duyne, R. P. Nanosphere lithography: A Materials General Fabrication Process for Periodic Particle Array Surfaces. *J. Vac. Sci. Technol. A* **1995**, *13*, 1553-1558.

(32) Aizpurua, J.; Hanarp, P.; Sutherland, D. S.; Käll, M.; Bryant, G. W.; García de Abajo, F. J. Optical Properties of Gold Nanorings. *Phys. Rev. Lett.* **2003**, *90*, 057401.

(33) Shumaker-Parry, J. S.; Rochholz, H.; Kreiter, M. Fabrication of Crescent-Shaped Optical Antennas. *Adv. Mater.* **2005**, *17*, 2131-2134.

(34) Bukasov, R.; Shumaker-Parry, J. S. Silver Nanocrescents with Infrared Plasmonic Properties As Tunable Substrates for Surface Enhanced Infrared Absorption Spectroscopy. *Anal. Chem.* **2009**, *81*, 4531-4535.

(35) Bukasov, R.; Shumaker-Parry, J. S. Highly Tunable Infrared Extinction Properties of Gold Nanocrescents. *Nano Lett.* **2007**, *7*, 1113-1118.

(36) Cooper, C. T.; Rodriguez, M.; Blair, S.; Shumaker-Parry, J. S. Polarization Anisotropy of Multiple Localized Plasmon Resonance Modes in Noble Metal Nanocrescents. *J. Phys. Chem. C* **2013**, *118*, 1167-1173.

(37) McPeak, K. M.; Jayanti, S. V.; Kress, S. J. P.; Meyer, S.; Iotti, S.; Rossinelli, A.; Norris, D. J. Plasmonic Films Can Easily Be Better: Rules and Recipes. *ACS Photonics* **2015**, *2*, 326-333.

(38) Palik, E. D. *Handbook of Optical Constants of Solids*; Academic Press: Waltham, MA, USA, **2012**.

(39) Rodriguez, M.; Furse, C.; Shumaker-Parry, J. S.; Blair, S. Scaling the Response of Nanocrescent Antennas into the Ultraviolet. *ACS Photonics* **2014**, *1*, 496-506.

(40) Zorić, I.; Zäch, M.; Kasemo, B.; Langhammer, C. Gold, Platinum, and Aluminum Nanodisk Plasmons: Material Independence, Subradiance, and Damping Mechanisms. *ACS Nano* **2011**, *5*, 2535-2546.

(41) Williams, D. B.; Carter, C. B. *Transmission Electron Microscopy*; Springer US: New York, NY, USA, **2009**; p 522-523.

CHAPTER 3

ARRAYED ALUMINUM PLASMONIC ANTENNAS FOR SURFACE-ENHANCED INFRARED ABSORPTION

3.1 Introduction

Aluminum as a plasmonic material has garnered significant attention in the past several years due to its ability to support plasmons in the ultraviolet (UV) region.[1, 2] While traditional plasmonic metals, such as Ag and Au are excellent for visible and near-infrared plasmonics, the interband transitions for these materials occur at lower wavelengths, preventing them from supporting plasmons in the UV.[3] Alternatively, Al is capable of supporting plasmons from the UV all the way to IR wavelengths (with the exception of 800 nm where it has an interband transition).[4] While most groups have used Al for low wavelength applications, some have started seeing the utility of Al as an attractive metal for IR plasmonics.[5]

In addition to its optical properties, Al has a few chemical and economical properties that make it favorable as a plasmonic material. Au is typically the favored plasmonic metal due to its low loss over the IR wavelength range and the fact that it is inert, but still easily functionalized using thiol chemistry. While Ag can also be functionalized using thiol chemistry, it is susceptible to oxidation over time, thus quenching its plasmonic properties. Alternatively, the oxide that forms over the surface of Al develops rapidly and is self-limiting.[6, 7] In addition to a self-limiting oxide layer, Al is

significantly cheaper than Ag or Au and is complementary metal oxide semiconductor (CMOS) compatible; hence incorporating Al into many commercial applications would be a more cost-effective material. There is active interest in the surface-enhanced Raman spectroscopy (SERS) capabilities of Al particles, especially at low wavelengths.[8-11] However, comparatively little work has been done using Al with surface-enhanced infrared absorption spectroscopy (SEIRA), despite having optical properties that are comparable to Au at long wavelengths.[5]

Initial research of SEIRA involved studying the enhancing effects of metal island films of Au and Ag.[12-16] More recent work with SEIRA has involved the design of specific nanostructures that yield greater field enhancements when compared to these films.[17-20] Designer nanoparticle systems focus on the production of either sharp tips or small, nanoparticle size gaps that lead to large field enhancements.[5, 15, 16, 18, 19, 21-23] Although Al has been recently used at long wavelengths for SEIRA, these nanoparticles were fabricated using electron beam lithography (EBL) which is not a scalable fabrication technique.[5] Here, we demonstrate a way to make a high concentration of aluminum nanoparticle antennas with polarization-dependent resonances that can be used at long wavelengths for SEIRA.

3.2 Materials and Methods

3.2.1 Materials and instrumentation

Copper (99.999%), aluminum (99.999%), and gold (99.999%) pellets were purchased from Kurt J. Lesker. Aldehyde functionalized polystyrene beads and tetrahydrofuran (THF) were purchased from ThermoFisher. Ethanol (200 proof) was purchased from Decon Labs. Octadecanthiol (ODT) and octadecylphosphonic acid

(ODPA) were purchased from Sigma-Aldrich. All water used was purified to 18 MΩ using a Barnstead NANOpure diamond system. UV/Vis/NIR measurements were collected using a Perkin Elmer Lambda 750. FT-IR spectra were acquired using a Spectrum 100. For FT-IR, 100 scans were averaged together using a 4 cm^{-1} J-stop aperture. SEM images were acquired using a FEI NovaNano 630 in immersion mode with a Helix detector.

3.2.2 Substrate preparation

Glass microscope slides were cleaned for 45 min in piranha acid (3:1 volume ratio H_2SO_4: H_2O_2) and rinsed three times with water. Slides were then cleaned for one hour in a 5:1:1 volume ratio H_2O: NH_4OH: H_2O_2 solution at 60˚C. Cleaned microscope slides were then rinsed with water three times and stored under water until use. CaF_2 slides (Optocity) were rinsed three times with isopropanol and dried under a stream of nitrogen, then cleaned for 5 min in a UV/Ozone chamber (Jelight Co.) and used immediately.

3.2.3 Polystyrene deposition

Disperse nanoparticles were fabricated by spin coating a solution of 0.5% (by volume in ethanol) onto clean substrates that were dried under N_2. Arrays of nanoparticles were made by first depositing a hexagonally close-packed monolayer of polystyrene beads onto the substrate. This was accomplished by previously published methods but will be described briefly here to account for slight deviations.[24] Clean substrates were placed in a petri dish angled at 5° and covered with water. A 50:50 volume mixture of stock aldehyde functionalized polystyrene microspheres and 200 proof ethanol were introduced to the petri dish using a syringe pump placed on a clean glass slide that was angled into the water (Figure 3.1). The PS beads collected at the air-water interface and the syringe pump was

stopped once a close-packed monolayer had formed, as determined by visual inspection. The water was then slowly pumped out of the petri dish using a peristaltic pump. As the water receded the close-packed monolayer was transferred onto the substrate.

3.2.4 Particle fabrication

Aluminum and gold nanoparticles were fabricated using copper mask nanosphere template lithography (Figure 3.1).[7] The use of close-packed polystyrene beads required the use of an oxygen plasma to create gaps between templates, allowing for metal to be deposited on the substrate and conform to the template shape. For crescent particles, a 50-nm copper film was deposited at a 20˚ relative to surface normal, forming a copper hole array. The plasmonic metal was then deposited on the opposite side of the templates, filling in the crescent shape shadows in the mask layer. Disks were fabricated by depositing the copper film normal to the surface, the polystyrene beads were removed using tape and the slides were cleaned using an oxygen plasma. The plasmonic metal was then deposited in the copper hole array. The sacrificial layer was removed using nitric acid and the film from the plasmonic metal was removed using sonication in water and tape. Aluminum was deposited to a thickness of 25 nm at a rate of at least 10 Å/s in a Denton SJ20C electron beam evaporator.[25] For gold nanostructures, a 2-nm Cr adhesion layer was deposited first followed by a 25-nm film of Au at a rate of 1-2 Å/s.

3.2.5 SAM functionalization

Gold and aluminum structures were coated with a self-assembled monolayer for SEIRA studies. Au nanoparticles were cleaned for 5 min in a UV/Ozone chamber and then immediately immersed in a 1 mM octadecanethiol in ethanol for 14 h. Al nanoparticles

were cleaned for 1 min in a Harrick plasma chamber (PDC-32G) and immediately placed immersed in a 2 mM solution of octadecylphosphonic acid (ODPA) in tetrahydrofuran for 14 h. Samples were carefully rinsed in either ethanol or THF, dried under nitrogen, and FT-IR measurements collected immediately after.

3.3 Results and Discussion

3.3.1 AlNC array fabrication

Aluminum plasmonic nanocrescent arrays were fabricated using nanosphere template lithography and a sacrificial copper layer.[7] Previous work demonstrated fabrication of aluminum antennas with polarization-dependent dipole and quadrupole resonances that were tuned from the UV through NIR wavelengths by changing template size. Using a sacrificial copper mask layer eliminated the need for an argon plasma etch step and the associated secondary sputtering.[26] Figure 3.1 shows the fabrication process and resulting AlNCs arrays and their optical properties. A close-packed monolayer of PS templates was deposited onto flat substrates using a monolayer transfer process (Figure 3.1A I).[24] The PS templates are reduced in size using an oxygen plasma (Figure 3.1A II). The plasma etch time must be long enough to create sufficient gaps between PS templates, as insufficient etch times results in the PS template forming shadow in the backbone of the adjacent particle. Conversely, etching the PS templates too long destroys the template integrity, leading to poorly defined nanostructures. PS templates that are reduced to 50-80% of their original size yield work well for the fabrication of NC particles. A sacrificial copper layer is deposited normal to the surface (Figure 3.1A III), followed by an angled deposition of the plasmonic metal (Figure 3.1A IV). The copper template is removed by submerging the samples briefly in concentrated nitric acid (Figure 3.1A V). Scotch tape

removal of the plasmonic metal film results in NC on the desired substrate (Figure 3.1A VI). The resulting NCs are highly concentrated and uniformly oriented on the substrate (Figure 3.1B). The optical response of these particles is dependent on the size, metal, and dielectric environment. The unpolarized UV/Vis/NIR spectrum of AlNCs with tip to tip diameters of 475 nm is shown in Figure 3.1C. Extinction measurements are a result of light that is both absorbed and scattered by the particles. These AlNCs have polarization-dependent short and long axis dipole resonances at 1365 nm and 2130 nm, respectively. Additionally, these particles exhibit a resonance at 480 nm that is attributed to the long axis quadrupole mode.

3.3.2 Optical effects of close-packed AlNCs

The fabrication of an array of AlNCs significantly increases the optical signal as compared to dispersed structures (Figure 3.2). Disperse AlNCs are fabricated by spin coating a PS template solution onto a substrate, resulting in a low-density of particles on the surface.[7] Depositing the PS templates in a hexagonally close-packed array maximizes the surface density of the AlNCs. To accurately compare the effect that AlNC density has on the optical properties, disperse and array AlNCs were prepared using 500 nm PS templates and etched simultaneously. The resulting AlNCs had a tip-to-tip diameter of 350 (±11) nm for arrays and 370 (±9) nm for dispersed; both sets had backbone thicknesses of 100 nm (Figure 3.2A/B). The total extinction of these two sets of particles is as expected: by increasing the density of particles on the surface, a considerable increase in the total extinction is observed (Figure 3.2C). Here the total extinction increases from ~0.02 for disperse particles to 0.2 for an array. These values can be used to estimate the difference in concentration, as particle arrays have ~100 times higher concentration of particles. Since

the enhancement of NCs is localized to a small volume around the tips, a large number of particles would aid in improving the ability to observe spectroscopic enhancement by using an ensemble measurement.

The fabrication of an array drastically reduces the separation distance between AlNCs possibly introducing dipolar coupling to the system. When two plasmonic structures are separated by 20 nm or less, the near field enhancement is greatly increased.[27, 28] This coupling is observed in far-field measurements as a red-shift of the LSPR and an increase in extinction.[27, 29-31] At separations larger than 20 nm, dipolar coupling is still present, and has a large effect on the refractive index sensitivity.[32, 33] This long-range dipole coupling is observed as a either a red or blue shift of the main LSPR peaks depending on separation distance and particle size.[33]

AlNCs do not exhibit a LSPR shift when the separation distance is reduced. The polarized extinction spectra of arrayed and dispersed AlNCs of approximately similar size were normalized and compared (Figure 3.2D). The short axis and long axis dipoles of the array and disperse AlNCs are nearly identical (Figure 3.2D). In addition to the lack of observed shift in the LSPR dipole resonance, as the AlNC separation is decreased, there is no broadening/narrowing of the peak linewidth. Previous work has shown that as the spacing between nanoparticles decreases, a broadening of the LSPR peak is observed.[32] The lack of a concerted shift in the LSPR to either longer or shorter wavelengths may be explained by the variability in the spacing of the AlNCs. When the PS templates are arranged in a close-packed array, there is not a single orientation over the entire substrate surface. Due to variations in the PS template size breaks occur in the packing order of the array. When AlNCs are fabricated on these multifaceted arrays, there is a multitude of

orientations of the AlNCs relative to one another. This leads to a large variation in the separation between AlNCs, and since the optical spectra are ensemble-based measurements, all of these variations are averaged out. Additionally, tuning of the separation distance by longer etch times is accompanied by a change in the diameter of the AlNCs. Consequently, this fabrication technique is not well suited to study the effect that nanoparticle spacing has on dipole coupling. Regardless, this fabrication technique does result in a high surface density of AlNCs with resonances that can be tuned over a wide range of wavelengths.

3.3.3 UV resonant AlNCs

AlNCs with average diameters of 140 nm resulted in resonances in the UV and visible wavelength range (Figure 3.3). This size is convenient as Rodriguez et. al simulated 140 nm diameter in their previous work, and the experimental spectra from these samples is consistent with their results.[34] The unpolarized spectrum of 140 nm AlNCs shows 5 peaks at 230 nm, 260nm, 460 nm, 690 nm, and 900nm (Figure 3.3B). The two peaks at 690 and 900 nm are both from the long axis dipole resonance, but this resonance is split by the interband transition of Al. Since Al will not support a plasmon at 800 nm, the extinction is reduced at this wavelength. The shoulder at 490 nm corresponds to a short axis dipole, and the two resonances at 230 nm and 260 nm are a result of higher order resonances. Polarized extinction spectra for the 140 nm diameter AlNCs are shown in Figure 3.3C/E and compared to previously published simulations (Figure 3.3 D/F). The short axis dipole at 490 nm is blue-shifted and broader compared to the simulated spectrum (Figure 3.3D/E). Broadening is most likely due to large variations in the backbone diameter and thickness that were not accounted for in the model, but are visible in the SEM image (Figure 3.3A).

The higher order modes at 230nm and 260 nm are present in both experimental and simulated spectra of the 140 nm AlNCs, although their relative intensities are substantially different. In the experimental results, these higher order modes have a much larger intensity in relation to the short axis dipole than what is predicted by the simulations, indicating that these higher order modes may be stronger than initially predicted. As for the long axis excitation, the simulations predict a quadrupole mode at 400 nm that is not observed in our experimental sample (Figure 3.3E/F). However, the higher order modes at 230nm and 260 nm are present in the experimental samples. In the simulations, the intensity of the resonance at 230 nm is larger than the 260 nm resonance, however, that is not the case in the experimental samples. Despite these discrepancies, the predicted response of 140 nm AlNCs aligns moderately well, considering the experimental samples have a much larger amount of heterogeneity in terms of size and shape than what can be accounted for in the simulations. This theoretical work shows that higher order resonant modes may be useful for surface-enhanced fluorescence and Raman spectroscopies. In this work, we are interested in seeing if AlNCs would be efficient for surface-enhanced absorption spectroscopies, as Al has not been used extensively for this application.

3.3.4 IR resonant AlNC

In order to study the SEIRA properties of AlNCs, arrays were fabricated with LSPR in the IR. Figure 3.4 shows the combined UV/Vis/NIR (200-2500 nm) and FT-IR (2500-6500 nm) spectra for large (>550 nm) AlNCs on calcium fluoride substrates. Unlike small AlNC fabricated with UV resonances, these particles are much more uniform as the large PS templates shrink more consistently (Figure 3.4B). Long axis dipoles were tuned to 2200 nm, 2415 nm, 3644 nm, and 3840 nm for AlNCs with diameters of 580 nm, 670 nm, 1140

nm, and 1240 nm, respectively. Short axis dipoles for these AlNCs reside in the NIR wavelength range with resonances at 1310 nm, 1430 nm, 2150 nm, and 2250 nm for AlNCs with diameters of 580 nm, 670 nm, 1140 nm, and 1240 nm, respectively. In addition to strong dipole resonances in the NIR/IR wavelength range, these AlNCs have higher order resonance modes in the UV/visible range. The 580 nm and 670 nm diameter AlNCs exhibit long and short axis quadrupole modes at 750 nm and 315 nm, respectively (Figure 3.4C). The 1140 nm AlNCs exhibit long and short axis quadrupole modes at 1130 nm and 495 nm, respectively (Figure 3.4D). These AlNCs samples exhibit LSPR over a wide wavelength range and potentially could be used to enhance the spectroscopic signal of molecules at several different wavelength ranges. This study focuses on the SEIRA enhancing properties of IR resonant dipoles.

3.3.5 Extinction efficiency of large Au and Al NCs

As relatively little work has been done using Al at IR wavelengths, the extinction efficiency of Al and Au NC with similar LSPR wavelengths was examined Table 3.1. Au is known to interact favorably in the IR wavelength range (although not as well as Ag) and has been successfully used for SEIRA.[18, 21, 22] By comparing the extinction efficiency of Al and Au NCs with similar LSPR frequencies, we may gain an understanding of how efficiently these AlNC antennas interact at longer wavelengths.[35, 36] The extinction cross-section of the long and short axis dipole resonances were calculated for Al and Au NCs by dividing the extinction ($\varepsilon = 2\text{-}\log_{10}[\%T]$) by the particle density (N, particles/nm^2) as previously reported.[37] As expected, the extinction cross section of the NCs increases with increasing size. This is expected as larger particles will scatter light more than smaller particles, and consequently have higher extinction cross-sections. It is interesting that Al

and Au particles of equivalent size have similar extinction cross-sections. AlNCs with a diameter of 670 nm have extinction cross-sections of 16 x 10^4 and 28 x 10^4 for their short and long axis dipoles, respectively. AuNCs of a similar size (610 nm) have extinction cross-sections of 18 x 10^4 and 22 x 10^4 for their short and long axis dipoles, respectively. While AuNCs can access longer wavelengths resonances at smaller sizes, it appears as though the two metals have similar cross-sections at similar sizes. This indicates that AlNCs is absorbing light as efficiently as AuNCs. Since light scattering increases with increasing particle size, Al and AuNCs of similar size are expected to scatter light similarly.

3.3.6 SEIRA of Al and Au NCs

Combining NTL with arrayed templates, we can fabricate a large surface density of AlNCs with resonances that can be tuned into the IR. To gain insight into the near-field enhancement of these large IR resonant AlNCs, we investigated their ability to enhance a molecule's spectroscopic signal. SEIRA relies, in part, on large electric fields to enhance the vibrational modes of molecules and can be measured using a simple transmission FT-IR measurement.[15] Al and Au NCs were functionalized with ODPA and ODT, respectively, to measure their efficacy in SEIRA. Thiols are known to preferentially adsorb to gold and long chain thiols like ODT form ordered monolayers.[21] However, thiol chemistry is not compatible with Al. Consequently, a different functional group must be chosen. Phosphonic acid modification of alumina is well documented and was chosen to functionalize our AlNCs. ODPA has the same chain length as ODT, and has been shown to form ordered monolayers over alumina.[38-43] In these experiments we are enhancing the symmetric and asymmetric methylene stretches. Consequently the functional group should not have a significant impact on the observed enhancement. Al and AuNCs with long axis

dipole resonances around 3390 nm (2950cm^{-1}) were used to measure the SEIRA enhancement of methylene symmetric and antisymmetric stretching modes (Figure 3.5). The addition of an ODT SAM on AuNCs results in a slight red shift of the LSPR peak (Figure 3.5A/B). AlNCs show a similar LSPR shift upon OPDA binding (Figure 3.5 C, D). There is a surprising amount of enhancement occurring on the particles that are off-resonance from the vibrational modes of interest for both Al and Au. One striking difference between the Au and Al enhancement is the shape of the vibrational peak. For the AuNCs, especially the on resonance particles, the vibrational modes take a very asymmetric peak shape that resembles a fano resonance. These peak shapes are consistent with previously reported peak shapes for Ag NCs and gold nanoantenna.[19, 44, 45] The enhancement peaks from the Al particles is unlike the AuNCs or other published work of SEIRA on Al.[5] The enhanced methylene vibrational modes on AlNCs do not exhibit a fano lineshape seen previously on Ag NCs, nor are the peaks inverted as seen on the asymmetric Al work published by Halas et. al.[5, 19] Instead, all the vibrational modes show an increased extinction and an asymmetric lineshape that slopes towards the LSPR maxima.

The enhancements of Al and Au NCs relative to a functionalized, continuous metal film were compared using previously published methods (Table 3.2).[19] The reflectivity of a monolayer of ODT or ODPA on a 25 nm thick continuous film of Au or Al, respectively, was converted to transmittance using the method described by Enders and Pucci.[46] The ratio of the IR transmission signal of the NC substrate to the transmission of the continuous film is reported as the enhancement in Table 3.2. As expected, when the LSPR overlaps with the methylene absorption at 2850cm^{-1} a larger enhancement is observed. This

observation holds true for both Al and Au NCs. To make a fair comparison to previously reported SEIRA values of AgNCs, the surface area normalized enhancement factor is also reported. These enhancement values are lower than Ag NCs reported earlier by an order of magnitude.[19] This discrepancy can be accounted for in the calculation of the portion of the substrate covered in nanoparticles. Previously reported SEIRA enhancements were done using disperse AgNCs, and calculating the portion of substrate covered with NCs can be difficult as the surface coverage can vary widely depending on what portion of the substrate is being examined. Using arrays of NCs, we have uniform surface coverage over the entire substrate, making our calculation of surface coverage significantly easier. This issue of surface area calculation may also explain the discrepancy seen in the extinction efficiency of the AuNCs reported here, and those reported previously (Table 3.1).[37] The extinction cross-section of the particles fabricated in this report are similar to those reported earlier, however, when incorporating the surface are coverage, our values are an order of magnitude lower.

From Table 3.2 it is appears that gold exhibits a larger SEIRA enhancement for both on and off resonant NC particles. While Au is expected to have slightly better optical properties at these long wavelengths, the calculated extinction efficiencies for these particles are approximately similar. An alternative explanation for this discrepancy is the different adhesion chemistries employed. Thiols chemistry on gold is well established and it may be assumed that all of the thiols on the AuNCs are attached to the metal in the same fashion, giving a uniform alkyl chain orientation. AlNCs may be a mix of bidentate and tridentate ligand binding.[40] This mixture of ligand binding may have an effect on the orientation of the alkyl chain relative to the enhanced electric field. SEIRA, much like

SERS, is sensitive to the orientation of the adsorbed molecule to the metal surface, and consequently, this mixing of binding modes may contribute to a slight decrease in the observed enhancement.[12-15]

3.4 Conclusion

Here we demonstrate the ability to fabricate a high concentration of plasmonic antennas on a surface by close-packing the polystyrene templates and subsequent template shrinking with an oxygen plasma. The resulting AlNC arrays have dipole resonances that can be tuned from the NIR to IR wavelength ranges with extinction efficiencies similar to AuNCs. The fabrication of an array of NC does not lead to coupling between structures, as no red shifting of the long axis dipole is observed. SEIRA measurements of Al and Au NC arrays were functionalized with ODPA and ODT, respectively. Particle arrays were fabricated with resonances on and off the asymmetric methylene vibrational modes. The different metals exhibited different enhancing peak shapes, with Au displaying enhancement profile similar to ODT on AgNC. The ODPA monolayers on AlNCs were unlike previously reported enhancements for large Al structures, potentially owing to the different packing order of ODPA versus stearic acid. It was shown that Al had slightly lower enhancement than Au structures at similar wavelengths. This discrepancy may be from the intrinsic optical properties of the two metals, or a difference in the binding mode of ODT on Au vs OPDA on Al, or a combination of the two.

Table 3.1 Extinction efficiencies of NIR and IR resonant Al and AuNCs

Particle diameter (nm)	λ_{MAX} (nm)	Extinction cross section (10^4 nm^2)	Extinction efficiency
Al 580 ± 31	*SA-1310*	*10*	*1.3*
	LA-2200	16	2.0
Al 670 ± 50	*SA-1430*	*16*	*1.9*
	LA-2415	26	3.0
Al 1140 ± 133	*SA-2150*	*29*	*1.3*
	LA-3644	46	2.0
Au 610 ± 35	*SA-1645*	*18*	*2.0*
	LA-2763	22	2.6
Au 800 ± 29	*SA-1920*	*19*	*1.6*
	LA-3263	38	3.2
Au 950 ± 31	*SA-2140*	*38*	*1.7*
	LA-3573	52	2.4

Table 3.2 SEIRA enhancements of Al and AuNCs

Size	Metal	LSPR (cm^{-1})	Enhancement	Surface-area normalized
670 nm	Al	4140	23	419
1140 nm	Al	2744	121	1231
610 nm	Au	3619	85	928
800 nm	Au	3064	253	4347

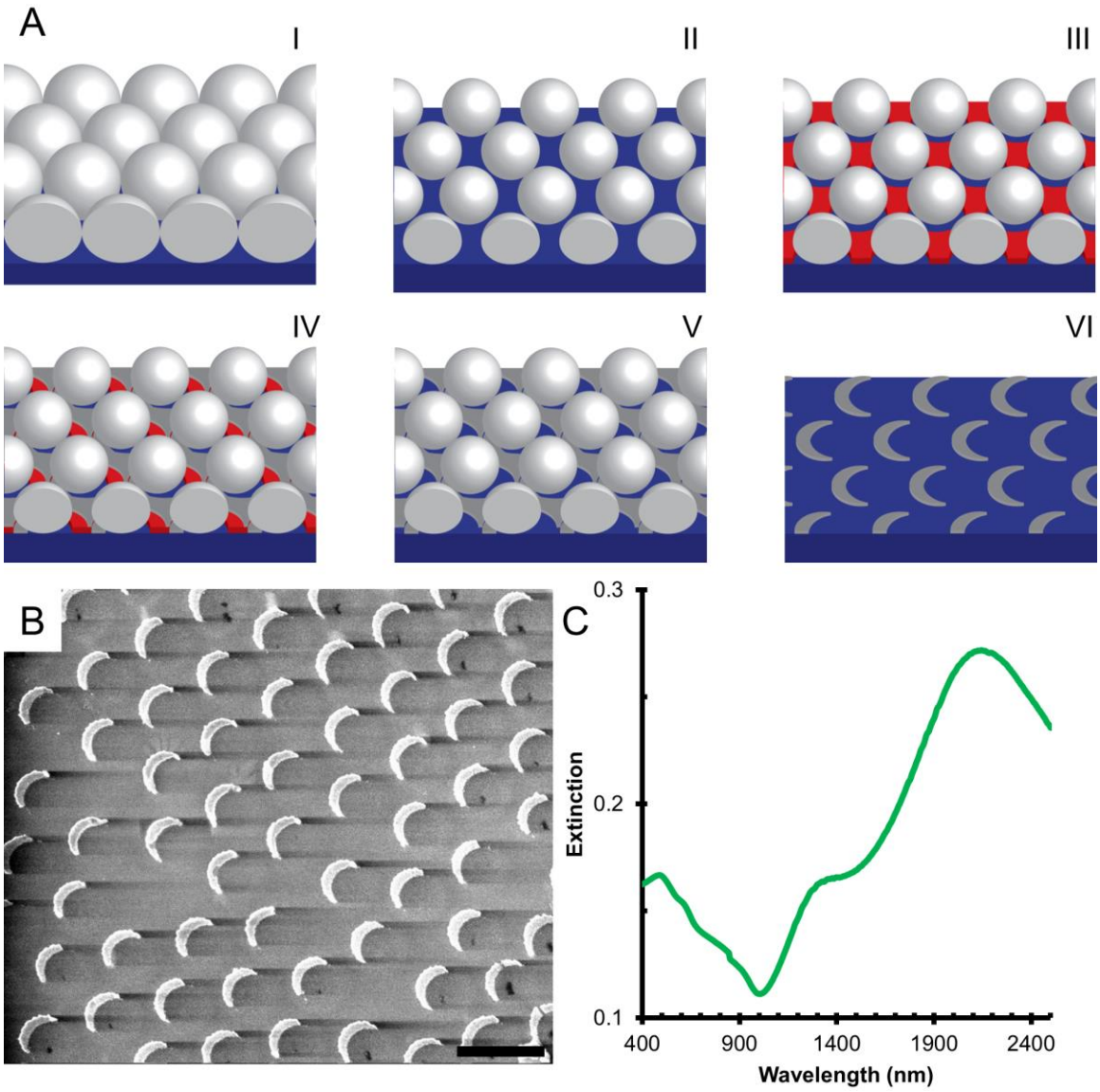

Figure 3.1 Overview of the fabrication of arrays of AlNCs. A) Close-packed PS templates are deposited on a clean, flat surface (I), and then shrunk using an O_2 plasma (II). A sacrificial copper layer (III) is deposited followed by the plasmonic metal (IV), Al or Au. The sacrificial layer is removed using nitric acid (V) and the film and templates are removed by sonication and tape (VI). The result is a high surface density of particles as seen by SEM (B) with high extinction values (C). Scale bar represents 1 μm.

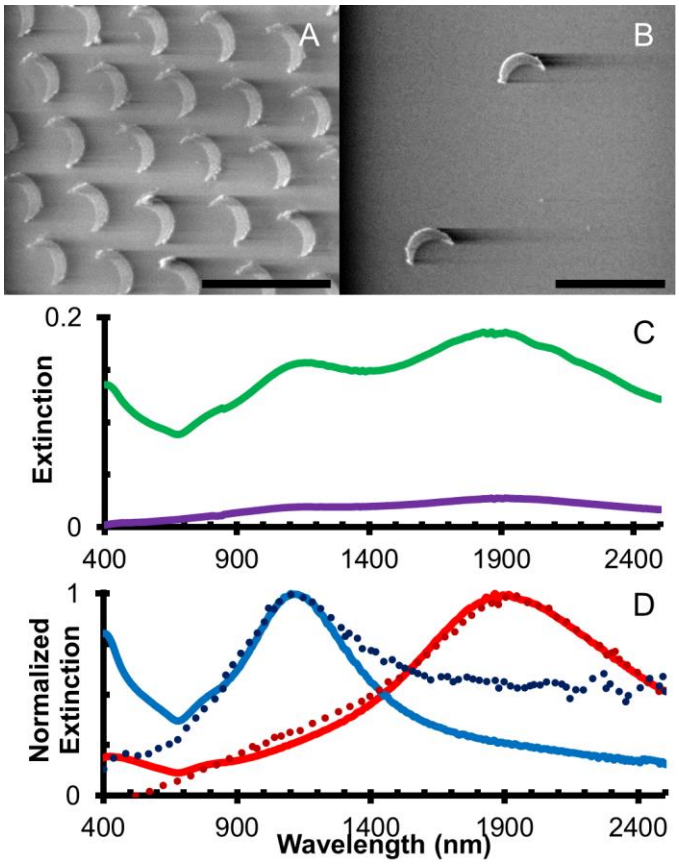

Figure 3.2 Arrayed and disperse AlNCs have similar optical responses. A) SEM images showing arrays of AlNCs (351 ± 11 nm) with an interparticle separation of 127 ± 21 nm and (B) disperse AlNCs (372 ± 9 nm) of similar size. Scale bars represent 1μm. C) UV Vis spectra of disperse (purple) and arrayed (green) AlNCs shows difference in extinction that accompanies the increase is particles. D) Polarized UV Vis spectra show the long axis (red) and short axis (blue) dipoles maintain their LSPR for a given size regardless of being arrayed (solid line) or dispersed (dotted line).

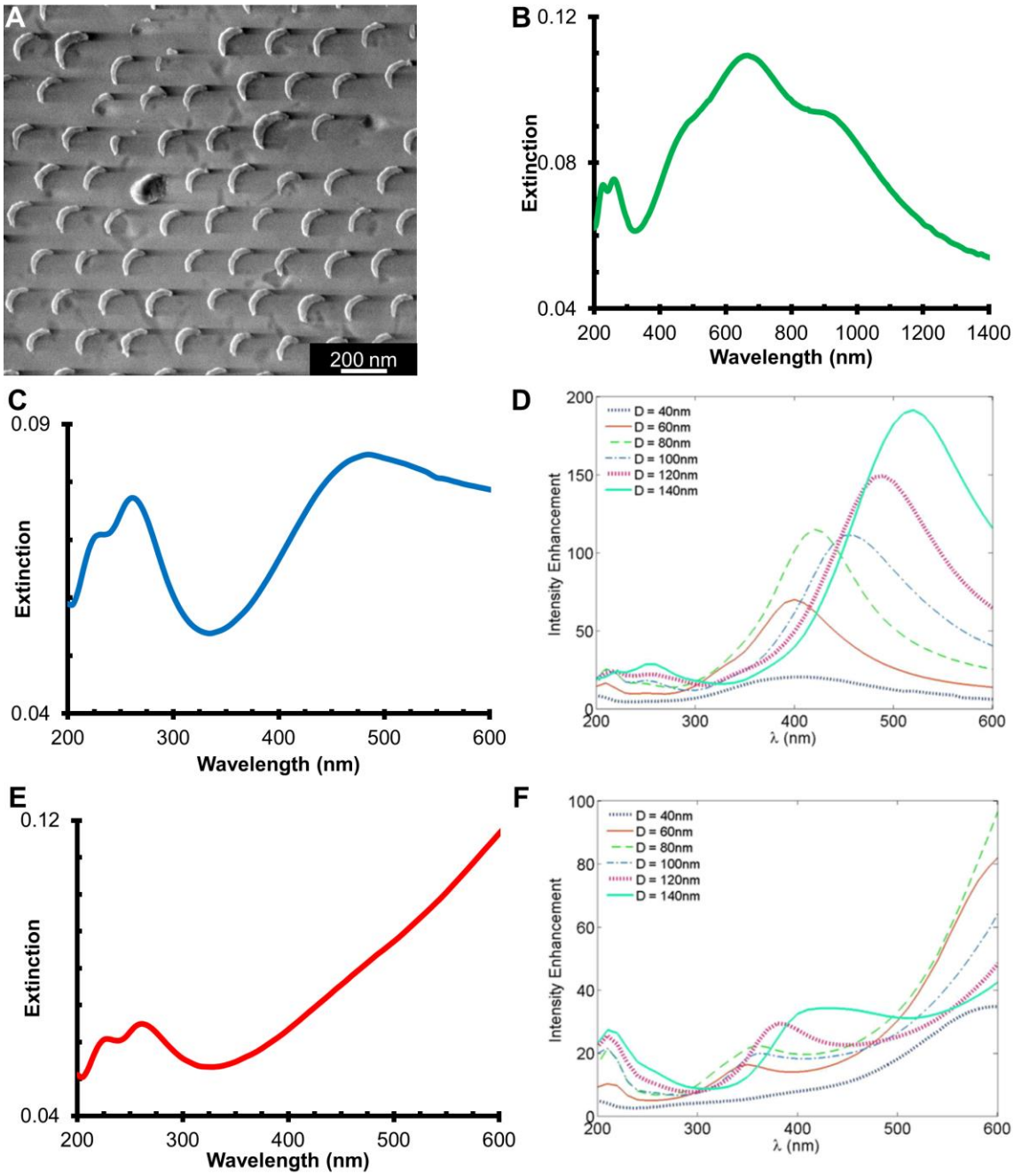

Figure 3.3 AlNCs arrays have optical responses that were predicted in previous work. A) SEM image of 140 nm diameter AlNCs and their corresponding unpolarized UV/Vis response (B). Polarized spectra show the short (C) and long axis (E) dipoles and their simulated response (D, F). (D, F are reprinted with permission from Rodriguez, M.; Furse, C.; Shumaker-Parry, J. S.; Blair, S. ACS Photonics 2014, 1(6), 496-506, Figure 7 Copyright 2014 American Chemical Society).

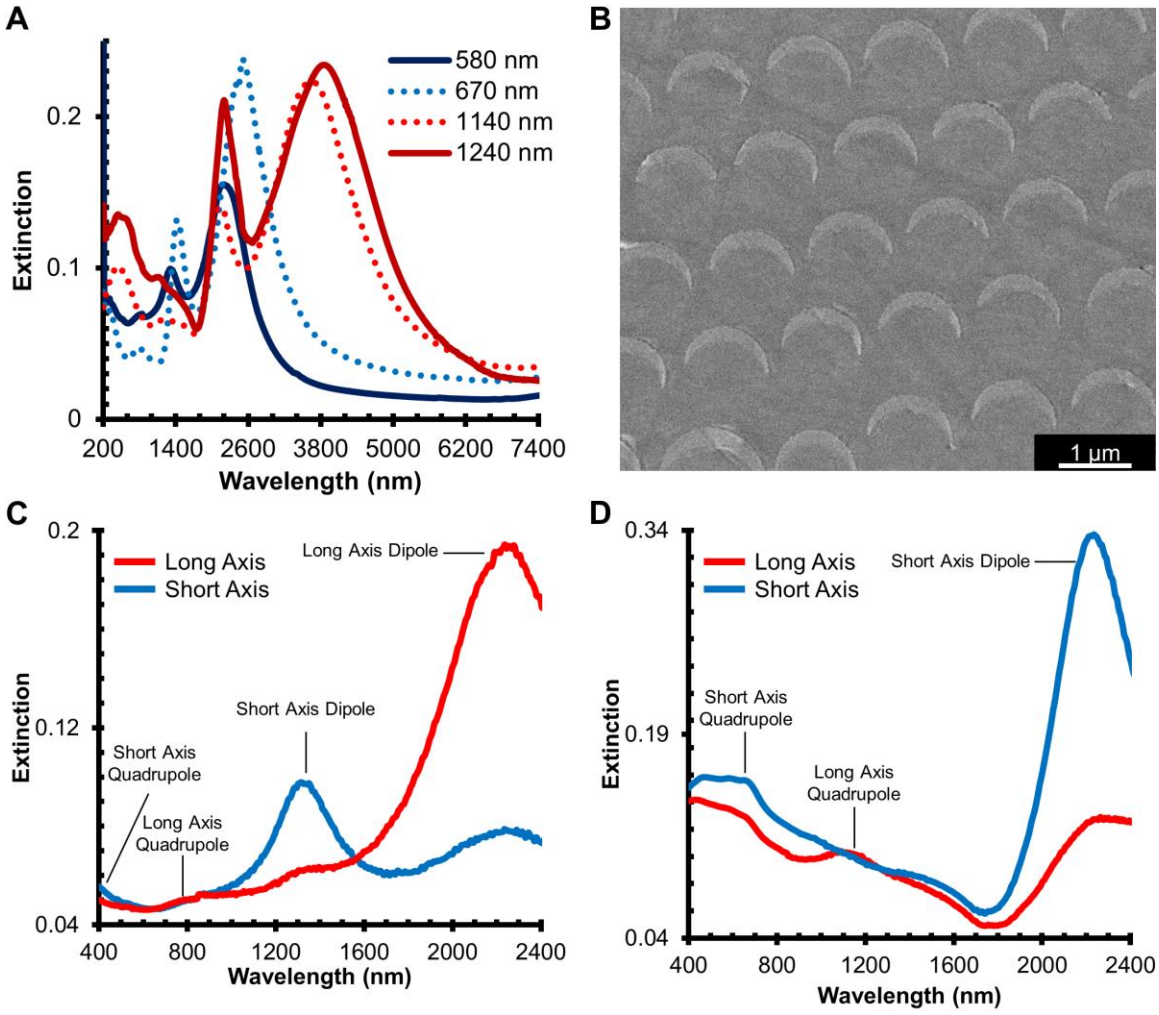

Figure 3.4 AlNCs are capable of supporting LSPR in IR wavelengths. A) Unpolarized UV/Vis/NIR/IR spectra of large (>550 nm) AlNCs on CaF_2. By increasing the template size the LSPR can be tuned into the IR wavelengths. B) SEM images reveal these particles have sharp, field enhancing tips that effectively enhance the electric near-field. The polarized Vis/NIR spectra of 580 nm (C) and 1160 nm (D) diameter AlNCs were used to identify short and long axis dipole and quadrupole modes.

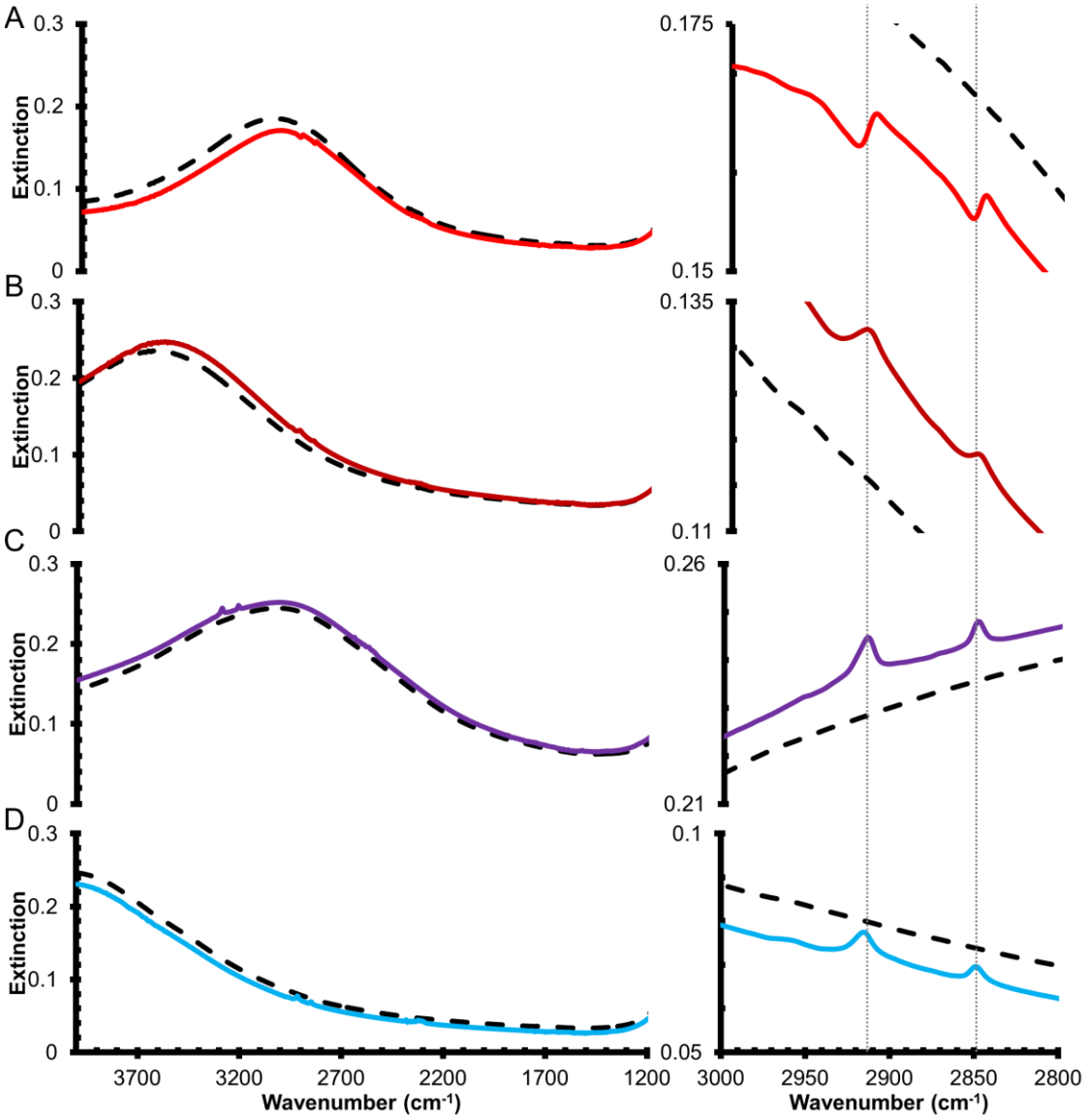

Figure 3.5 SEIRA enhancements of Al and Au NCs. FT-IR spectra for 800 nm (A) and 610 nm (B) AuNC functionalized with 1 mM ODT (solid lines). The FT-IR spectra of 1140 nm (C) and 670 nm (D) AlNCs functionalized with 2 mM ODPA are shown (solid lines). The AlNCs are corrected for the signal of ODPA on clean CaF_2.

3.5 References

(1) Chowdhury, M. H.; Ray, K.; Gray, S. K.; Pond, J.; Lakowicz, J. R. Aluminum Nanoparticles as Substrates for Metal-Enhanced Fluorescence in the Ultraviolet for the Label-Free Detection of Biomolecules. *Anal. Chem.* **2009**, *81*, 1397-1403.

(2) Ekinci, Y.; Solak, H. H.; Löffler, J. F. Plasmon Resonances of Aluminum Nanoparticles and Nanorods. *J. Appl. Phys.* **2008**, *104*, 083107.

(3) McMahon, J. M.; Schatz, G. C.; Gray, S. K. Plasmonics in the Ultraviolet with the Poor Metals Al, Ga, In, Sn, Tl, Pb, and Bi. *Phys. Chem. Chem. Phys.* **2013**, *15*, 5415-5423.

(4) Davy, G.; Stephen, K. G. Aluminium Plasmonics. *J. Phys. D: Appl. Phys.* **2015**, *48*, 184001.

(5) Cerjan, B.; Yang, X.; Nordlander, P.; Halas, N. J. Asymmetric Aluminum Antennas for Self-Calibrating Surface-Enhanced Infrared Absorption Spectroscopy. *ACS Photonics* **2016**, *3*, 354-360.

(6) Langhammer, C.; Schwind, M.; Kasemo, B.; Zorić, I. Localized Surface Plasmon Resonances in Aluminum Nanodisks. *Nano Lett.* **2008**, *8*, 1461-1471.

(7) Swartz, M.; Rodriguez, M.; Quast, A. D.; Cooper, C. T.; Blair, S.; Shumaker-Parry, J. S. Aluminum Nanocrescent Plasmonic Antennas Fabricated by Copper Mask Nanosphere Template Lithography. *J. Phys. Chem. C* **2016**, *120*, 20597-20603.

(8) Jha, S. K.; Ahmed, Z.; Agio, M.; Ekinci, Y.; Löffler, J. F. Deep-UV Surface-Enhanced Resonance Raman Scattering of Adenine on Aluminum Nanoparticle Arrays. *J. Am. Chem. Soc.* **2012**, *134*, 1966-1969.

(9) Yang, Z.-L.; Li, Q.-H.; Ren, B.; Tian, Z.-Q. Tunable SERS from Aluminium Nanohole Arrays in the Ultraviolet Region. *Chem. Commun.* **2011**, *47*, 3909-3911.

(10) Mogensen, K. B.; Guhlke, M.; Kneipp, J.; Kadkhodazadeh, S.; Wagner, J. B.; Espina Palanco, M.; Kneipp, H.; Kneipp, K. Surface-Enhanced Raman Scattering on Aluminum Using Near Infrared and Visible Excitation. *Chem. Commun.* **2014**, *50*, 3744-3746.

(11) Sigle, D. O.; Perkins, E.; Baumberg, J. J.; Mahajan, S. Reproducible Deep-UV SERRS on Aluminum Nanovoids. *J. Phys. Chem. Lett.* **2013**, *4*, 1449-1452.

(12) Osawa, M.; Ataka, K.-I.; Yoshii, K.; Nishikawa, Y. Surface-Enhanced Infrared Spectroscopy: The Origin of the Absorption Enhancement and Band Selection Rule in the Infrared Spectra of Molecules Adsorbed on Fine Metal Particles. *Appl. Spectrosc.* **1993**, *47*, 1497-1502.

(13) Merklin, G. T.; Griffiths, P. R. Influence of Chemical Interactions on the Surface-

Enhanced Infrared Absorption Spectrometry of Nitrophenols on Copper and Silver Films. *Langmuir* **1997**, *13*, 6159-6163.

(14) Merklin, G. T.; Griffiths, P. R. Effect of Microscopic Surface Roughness in Surface-Enhanced Infrared Absorption Spectrometry. *J. Phys. Chem. B* **1997**, *101*, 5810-5813.

(15) Osawa, M. Surface-Enhanced Infrared Absorption. In *Near-Field Optics and Surface Plasmon Polaritons*; Kawata, S., Ed. Springer Berlin Heidelberg: Berlin, Heidelberg, 2001; pp 163-187.

(16) Jensen, T. R.; Duyne, R. P. V.; Johnson, S. A.; Maroni, V. A. Surface-Enhanced Infrared Spectroscopy: A Comparison of Metal Island Films with Discrete and Nondiscrete Surface Plasmons. *Appl. Spectrosc.* **2000**, *54*, 371-377.

(17) Le, F.; Brandl, D. W.; Urzhumov, Y. A.; Wang, H.; Kundu, J.; Halas, N. J.; Aizpurua, J.; Nordlander, P. Metallic Nanoparticle Arrays: A Common Substrate for Both Surface-Enhanced Raman Scattering and Surface-Enhanced Infrared Absorption. *ACS Nano* **2008**, *2*, 707-718.

(18) Chae, J.; Lahiri, B.; Centrone, A. Engineering Near-Field SEIRA Enhancements in Plasmonic Resonators. *ACS Photonics* **2016**, *3*, 87-95.

(19) Bukasov, R.; Shumaker-Parry, J. S. Silver Nanocrescents with Infrared Plasmonic Properties As Tunable Substrates for Surface Enhanced Infrared Absorption Spectroscopy. *Anal. Chem.* **2009**, *81*, 4531-4535.

(20) Adato, R.; Yanik, A. A.; Amsden, J. J.; Kaplan, D. L.; Omenetto, F. G.; Hong, M. K.; Erramilli, S.; Altug, H. Ultra-Sensitive Vibrational Spectroscopy of Protein Monolayers with Plasmonic Nanoantenna Arrays. *Proc. Natl. Acad. Sci. USA* **2009**, *106*, 19227-19232.

(21) Brown, L. V.; Yang, X.; Zhao, K.; Zheng, B. Y.; Nordlander, P.; Halas, N. J. Fan-Shaped Gold Nanoantennas above Reflective Substrates for Surface-Enhanced Infrared Absorption (SEIRA). *Nano Lett.* **2015**, *15*, 1272-1280.

(22) Brown, L. V.; Zhao, K.; King, N.; Sobhani, H.; Nordlander, P.; Halas, N. J. Surface-Enhanced Infrared Absorption Using Individual Cross Antennas Tailored to Chemical Moieties. *J. Am. Chem. Soc.* **2013**, *135*, 3688-3695.

(23) Novotny, L.; Bian, R. X.; Xie, X. S. Theory of Nanometric Optical Tweezers. *Phys. Rev. Lett.* **1997**, *79*, 645-648.

(24) Chen, K.; Rajeeva, B. B.; Wu, Z.; Rukavina, M.; Dao, T. D.; Ishii, S.; Aono, M.; Nagao, T.; Zheng, Y. Moiré Nanosphere Lithography. *ACS Nano* **2015**, *9*, 6031-6040.

(25) McPeak, K. M.; Jayanti, S. V.; Kress, S. J. P.; Meyer, S.; Iotti, S.; Rossinelli, A.; Norris, D. J. Plasmonic Films Can Easily Be Better: Rules and Recipes. *ACS Photonics*

2015, *2*, 326-333.

(26) Aizpurua, J.; Hanarp, P.; Sutherland, D. S.; Käll, M.; Bryant, G. W.; García de Abajo, F. J. Optical Properties of Gold Nanorings. *Phys. Rev. Lett.* **2003**, *90*, 057401.

(27) Jain, P. K.; El-Sayed, M. A. Plasmonic Coupling in Noble Metal Nanostructures. *Chem. Phys. Lett.* **2010**, *487*, 153-164.

(28) Kinkhabwala, A.; Yu, Z.; Fan, S.; Avlasevich, Y.; Mullen, K.; Moerner, W. E. Large Single-Molecule Fluorescence Enhancements Produced by a Bowtie Nanoantenna. *Nat. Photon.* **2009**, *3*, 654-657.

(29) Suh, J. Y.; Odom, T. W. Nonlinear Properties of Nanoscale Antennas. *Nano Today* **2013**, *8*, 469-479.

(30) Muskens, O. L.; Giannini, V.; Sánchez-Gil, J. A.; Gómez Rivas, J. Optical Scattering Resonances of Single and Coupled Dimer Plasmonic Nanoantennas. *Opt. Express* **2007**, *15*, 17736-17746.

(31) Hentschel, M.; Utikal, T.; Giessen, H.; Lippitz, M. Quantitative Modeling of the Third Harmonic Emission Spectrum of Plasmonic Nanoantennas. *Nano Lett.* **2012**, *12*, 3778-3782.

(32) Haynes, C. L.; McFarland, A. D.; Zhao, L.; Van Duyne, R. P.; Schatz, G. C.; Gunnarsson, L.; Prikulis, J.; Kasemo, B.; Käll, M. Nanoparticle Optics: The Importance of Radiative Dipole Coupling in Two-Dimensional Nanoparticle Arrays. *J. Phys. Chem. B* **2003**, *107*, 7337-7342.

(33) Vazquez-Mena, O.; Sannomiya, T.; Villanueva, L. G.; Voros, J.; Brugger, J. Metallic Nanodot Arrays by Stencil Lithography for Plasmonic Biosensing Applications. *ACS Nano* **2011**, *5*, 844-853.

(34) Rodriguez, M.; Furse, C.; Shumaker-Parry, J. S.; Blair, S. Scaling the Response of Nanocrescent Antennas into the Ultraviolet. *ACS Photonics* **2014**, *1*, 496-506.

(35) Evanoff, D. D.; Chumanov, G. Size-Controlled Synthesis of Nanoparticles. 2. Measurement of Extinction, Scattering, and Absorption Cross Sections. *J. Phys. Chem. B* **2004**, *108*, 13957-13962.

(36) Kelly, K. L.; Coronado, E.; Zhao, L. L.; Schatz, G. C. The Optical Properties of Metal Nanoparticles: The Influence of Size, Shape, and Dielectric Environment. *J. Phys. Chem. B* **2003**, *107*, 668-677.

(37) Bukasov, R.; Shumaker-Parry, J. S. Highly Tunable Infrared Extinction Properties of Gold Nanocrescents. *Nano Lett.* **2007**, *7*, 1113-1118.

(38) Ramsier, R. D.; Henriksen, P. N.; Gent, A. N. Adsorption of Phosphorus Acids on Alumina. *Surf. Sci.* **1988**, *203*, 72-88.

(39) Messerschmidt, C.; Schwartz, D. K. Growth Mechanisms of Octadecylphosphonic Acid Self-Assembled Monolayers on Sapphire (Corundum): Evidence for a Quasi-equilibrium Triple Point. *Langmuir* **2001**, *17*, 462-467.

(40) Luschtinetz, R.; Seifert, G.; Jaehne, E.; Adler, H.-J. P. Infrared Spectra of Alkylphosphonic Acid Bound to Aluminium Surfaces. *Macromol. Symp.* **2007**, *254*, 248-253.

(41) Liakos, I. L.; McAlpine, E.; Chen, X.; Newman, R.; Alexander, M. R. Assembly of Octadecyl Phosphonic Acid on the α-Al2O3 (0 0 0 1) Surface of Air Annealed Alumina: Evidence for Termination Dependent Adsorption. *Appl. Surf. Sci.* **2008**, *255*, 3276-3282.

(42) Giza, M.; Thissen, P.; Grundmeier, G. Adsorption Kinetics of Organophosphonic Acids on Plasma-Modified Oxide-Covered Aluminum Surfaces. *Langmuir* **2008**, *24*, 8688-8694.

(43) Thissen, P.; Valtiner, M.; Grundmeier, G. Stability of Phosphonic Acid Self-Assembled Monolayers on Amorphous and Single-Crystalline Aluminum Oxide Surfaces in Aqueous Solution. *Langmuir* **2010**, *26*, 156-164.

(44) Cataldo, S.; Zhao, J.; Neubrech, F.; Frank, B.; Zhang, C.; Braun, P. V.; Giessen, H. Hole-Mask Colloidal Nanolithography for Large-Area Low-Cost Metamaterials and Antenna-Assisted Surface-Enhanced Infrared Absorption Substrates. *ACS Nano* **2012**, *6*, 979-985.

(45) Neubrech, F.; Pucci, A.; Cornelius, T. W.; Karim, S.; García-Etxarri, A.; Aizpurua, J. Resonant Plasmonic and Vibrational Coupling in a Tailored Nanoantenna for Infrared Detection. *Phys. Rev. Lett.* **2008**, *101*, 157403.

(46) Enders, D.; Pucci, A. Surface Enhanced Infrared Absorption of Octadecanethiol on Wet-Chemically Prepared Au Nanoparticle Films. *Appl. Phys. Lett.* **2006**, *88*, 184104.

CHAPTER 4

HOMO- AND HETEROMETALLIC DIMER NANOCRESCENT ANTENNAS

4.1 Introduction

The fabrication and design of plasmonic nanostructures continues to be an active are of research, mainly due to the difficulty in consistently producing features at the nanometer length scale. For surface-enhanced Raman (SERS), fluorescence (SEF), and infrared absorption (SEIRA) spectroscopies, there is interest in plasmonic structures that produce large field enhancements. At optical frequencies, this goal is achieved through the fabrication of sharp tips or small gaps.[1-7] Sharp tips are defined as having a radius of curvature of around 5 nm and have shown to be useful in tip-enhanced Raman spectroscopy.[3, 8, 9] Plasmonic coupling occurs when two structures are separated by distances of 2-20 nm, and subsequently, large field enhancements are produced in this gap.[6, 10-12]

One common approach for the production of plasmonic gaps is through the asymmetric functionalization of synthesized nanoparticles. Nanoparticles made by the reduction of a metal salt are selectively functionalized with either thiol ligands or DNA, and through ligand chemistry dimer particles with tunable gap distances can be produced.[12-18] Although DNA is a great spacer ligand that allows for highly tunable gap distances, these particles are produced in solution, and orientation control of these particles is

impossible. Dimer gap systems exhibit strong field enhancements when the incident electric field polarization is parallel to the dimer axis; this is desirable in certain applications.[7, 14, 19] Electron beam lithography (EBL) has been used to fabricate nanoparticle gap systems that have uniform orientation and small gap sizes.[11, 20] This technique allows for thorough investigation of fundamental properties of nanogap systems but cannot be used to produce structures on a large scale. Nanosphere lithography is a cost-effective method that has been used to produce nanogap structures, however, these particles are arranged in a radial patterns and consequently lack polarization dependence.[21]

NTL has been successfully used to produce plasmonic structures of gold (Au), silver (Ag), and aluminum (Al) with sharp tips that have shown large theoretical field enhancements.[22-24] However, this method has, until recently, been incapable of producing nanometer scale gaps between particles. Here, we utilize the native oxide that forms over Al to define the gap between two nanostructures. Previous work utilized angled metal deposition over a well hole to determine the gap distance between two ellipses.[2] This approach leads to large errors in the gap distance, whereas the native alumina layer that forms over Al metal is consistently in the 2-4nm range.[22, 25]

4.2 Materials and Methods

4.2.1 Materials

Pellets of Cu (99.999%), Al (99.999%), and Au (99.999%) were purchased from Kurt J. Lesker. Water was purified using a Barnstead NANOpure Diamond system to a resistance of 18 MΩ. Aldehyde-functionalized polystyrene microspheres were purchased from Life Technology. Ethanol (200 proof) was purchased from Decon Labs. Glass microscope slides were first cleaned for 45 min in piranha acid; 3:1 volume ratio H_2SO_4:

30% H_2O_2. The glass was then rinsed three times with water and then placed in a sonication bath at 60 ˚C for 60 min in a solution of 5:1:1 volume ratio H_2O: NH_4OH: 30 % H_2O_2. Slides were rinsed three times and stored under water for up to one week. CaF_2 disks were purchased from OptoCity and cleaned by rinsing with isopropanol (99.5 %, Sigma) and drying under N_2 followed by UV/Ozone (Jelight Co.) cleaning for 5 min. CaF_2 disks were used immediately after cleaning.

4.2.2 Dimer nanocrescent fabrication

Nanosphere template lithography is a simple method for producing nanoparticles over large areas of a substrate.[26, 27] Crescent antennas were fabricated in accordance with previously published procedures.[22] Slight modifications to established protocols were used to fabricate dimer nanocrescents (DNCs) and are described here briefly. Polystyrene templates were deposited as a close-packed monolayer using a method adapted from Chen and Moitra.[28, 29] In this process, cleaned substrates are placed in a petri dish and covered with water; the dish is then elevated slightly at one end. A close-packed monolayer of aldehyde functionalized polystyrene microspheres (Life Technologies) is formed on the air-water interface. Microspheres are introduced to the surface using a syringe pump and a clean glass slide that is placed at an angle into the water. Microspheres are pumped until a close-packed monolayer covers the entire water surface, as observed by visual inspection of a complete iridescent film. The water is then removed from the petri dish at a slow, constant rate using a peristaltic pump. As the water is removed, the close-packed monolayer is transferred to the cleaned substrate.

For the fabrication of DNCs, gaps between the microspheres were created by shrinking the templates with an oxygen plasma. This allows for the deposition of metal on

the surface around the spherical templates, as opposed to the fabrication of various triangles.[5, 30-32] A 70 nm sacrificial layer of copper was deposited normal to the surface using an electron beam evaporator (Denton, New Jersey) at a rate of 2-10 Å/s and at pressures around 5.0 x 10^{-6} Tor. While these conditions are not optimal for the production of a quality plasmonic Cu film, the layer will not be used for plasmonics, hence, we only need to deposit a continuous metal film that can later be removed.[33] Al was deposited at a 40˚ angle to the surface normal using an e-beam evaporator at a pressure of 1 x 10^{-6} Tor and at rates exceeding 10 Å/s to achieve a 25 nm film thickness. The chamber was then vented and the substrates were rotated ~180˚ relative to the source of the metal. A second, 25 nm film, of plasmonic metal was then deposited, again at an angle of 40˚ relative to surface normal. For preparing Au structures, Au was deposited at a rate of 1-2 Å/s and at pressures below 2 x 10^{-6} Tor. A 3nm Cr layer was deposited prior to Au deposition to promote adhesion to the substrate. The sacrificial copper layer is removed by rapidly submersing the substrates in concentrated nitric acid followed by a water rinse. The remaining gold or aluminum film is removed using 3M scotch tape, leaving behind plasmonic structures on the substrate.

4.3 Results and Discussion

4.3.1 Aluminum nanocrescents

Here we demonstrate that coupling between crescent shaped nanoparticles can be achieved by fabricating two structures facing each other (Figure 4.1). Previous work has demonstrated that aluminum plasmonic antennas may be fabricated by combining nanosphere template lithography with a sacrificial copper layer.[22] These aluminum nanocrescents (AlNCs) have polarization-dependent dipole resonances that can be tuned

from the UV to NIR wavelengths by changing template size. The incorporation of the sacrificial layer was shown to be necessary as Al oxidizes rapidly under atmospheric conditions to form a 3 nm protective layer of Al_2O_3.[25] Once again, we take advantage of this oxide layer to create a gap between two NC particles. Nanoparticles have been shown to couple with each other at distances from 2 to several hundred nanometers.[7, 34-36] When nanoparticles are within 20 nm of one another, coupling leads to large near field enhancement as well as a red-shift of the LSPR.[36-38] By fabricating two NCs facing each other, we are able to create a gap between the structures that is defined by the native oxide of Al. This is accomplished by fabricating an AlNCs array, venting the chamber allowing the Al to oxidize and depositing a second set of NCs facing the original structures (Figure 4.1).

For reference, an array of AlNCs with a tip to tip distance of 350 nm and a backbone thickness of 100 nm was fabricated on a glass substrate. The SEM image and unpolarized optical response of this AlNC array are shown in Figure 4.2 A/B. These structures show distinct resonances in the NIR region that correspond to dipole resonances. The short axis dipole (1095 nm) and long axis dipole (1900 nm) are the two most prominent features in the spectrum. The long axis dipole shows a larger extinction value presumably because of the increased scattering associated with this excitation geometry. Previous publications have demonstrated the polarization-dependent response of these dipole modes, and by changing the incident polarization these modes may be selectively inducing.[22, 39-41] In addition to these dipole modes, a quadrupole resonance is observed at 400 nm. When the light is polarized along the short axis, there is a stronger extinction at 400 nm indicating that this mode is dominated by a short axis quadrupole (data not shown). When the incident

light is polarized along the long axis the extinction at 400 nm is reduced, but still present. Indicating the extinction at 400 may be due to higher order modes from both long and short axis excitations. Alternatively, this resonance may be due to an out of plane dipole that has been observed in large AuNCs.[40]

4.3.2 Homometallic DNCs

Coupling two AlNCs to each other through a nm scale gap leads to drastic changes in the optical response (Figure 4.2C). Controlling nm scale gaps is challenging with any nanoparticle assembly or fabrication technique, but here we have found a way to maintain a minimum separation between two NC structures. By depositing an array of AlNCs on a substrate and venting the chamber, the Al film is allowed to form a native ~3nm oxide layer.[25] This oxide layer acts as the nanometer spacer for when the second set of AlNCs are deposited on the opposite side of the template. The result is two AlNCs that overlap at their tips, but maintain a nanometer gap separation due to the native oxide (Figure 4.2D). This simple geometry modification leads to a large shift in the unpolarized optical response (Figure 4.2C). Instead of two distinct dipole resonances, one broad LSPR response is centered at 1385 nm. This resonance lies between both the long and short axis dipole resonances observed in single AlNCs (Figure 4.2A). Previous studies of dipolar coupling would explain the drastic red-shifting that is observed due to the close proximity of the two structures.[36]

In addition to the strong, broad peak in the NIR, a weaker mode is observed at 490 nm for the homodimer structures. This LSPR response may be a quadrupole mode that is present in the DNC. While quadrupole fields decay more rapidly than dipole fields, $1/r^5$ and $1/r^3$, respectively, (with r being distance from the particle), it may still be feasible for

a coupling of the quadrupole modes to occur.[36] El Sayed and co-workers showed that at interparticle gaps smaller than 0.5D (with D being the particle diameter) multipolar interactions begin to play a role in the coupling.[36] With DNC diameters of ~350 nm and gap distances between 3-6 nm, the effect of quadrupolar and potentially even octupolar modes cannot be ruled out.

The SEM of these particles shows the crescents are not perfectly symmetric relative to each other (Figure 4.2D). At one end, there is a clear 5-10nm gap separating the tips of the two particles. Opposite this gap, it appears as though tips of the crescent particles are overlapping. It should be noted that the aluminum oxide layer is approximately 3 nm thick, regardless of whether the film oxidized under atmospheric conditions or due to exposure to concentrated nitric acid.[22, 25] The oxidation of an Al film even occurs on the substrate side of the film and is responsible for Al's adhesion to glass.[42] Consequently, where there is a distinct gap observable in the SEM images, the separation between plasmonic materials is expected to be ~6nm larger. Also, where the tips of the two crescent structures overlap, there is an Al_2O_3 layer separating the two structures of 3-6nm.

A more detailed analysis of the optical response of these Al/Al DNC structures is obtained by looking at their response to polarized light (Figure 4.3). For reference, the polarization of the incident light relative to the NCs is indicated in the SEM image of the sample (Figure 4.3C). Long axis and short axis refer to the orientation of the polarization relative to the entire DNC structures, with the long axis defined as the axis that is parallel to the line running from the two tips while the short axis is defined as the line from the backbones (the yellow and light blue arrows, respectively) to the center of the dimer structure. From the polarized optical spectra, it can be seen that the broad resonance

centered at 1385 nm is actually composed of two LSPR modes (Figure 4.3A). When the incident light is polarized at 40°, a strong response at 1385 nm is observed. Changing the incident polarization to 130° leads to a relatively weak response at 1205 nm as well as an increased extinction at wavelengths that are beyond the transmission of the substrate (>2400 nm). Surprisingly, these two polarizations are offset 30° from the short (100°) and long (190°) axis geometries of the Al/Al DNCs. When light is polarized along the 100° axis and 190° axis an extinction maximum is observed at 1385 nm, although the magnitude and broadness of the extinction is markedly different. As the 100° polarization is aligned with the short axis of the DNC, the broadening and red-shifting relative to the short axis dipole resonance of a single AlNC may be indicative of dipole coupling. The 190° polarization is blue-shifted from the long axis dipole of a single AlNC. Consequently, the observed spectra are more complex than a simple dipole coupling model and higher order modes may be involved.

Additionally, the resonance in the visible wavelength range exhibits a strong polarization-dependent response. The LSPR mode at 490 nm increases in amplitude when light is polarized at 130° and reaches a minimum at the perpendicular excitation (40°). Again, these polarization angles are 30° offset from the long and short axis of the Al/Al DNC. What is notable is that the 100° polarization has a high extinction at this wavelength, which is associated with the short axis of the Al/Al DNC. Additionally, the 160° excitation, which aligns more closely with the long axis of the Al/Al DNC, exhibits a similar extinction value.

Seeing a coupling effect in both the long and short axis excitation is not surprising. Previous simulations have shown that when a single NC (Al, Au, or Ag) is excited, the tip

regions experience the greatest field enhancements.[22, 23, 41] Consequently, we would expect to see a plasmonic coupling effect occur when light is polarized along either the long or short axis. In a simple model, this coupling would be manifested by a red-shift of both long axis and short axis excitations. However, what is observed is more complex than simple dipole coupling and may be the result of higher order modes. This is plausible as the separation distance in the DNC system is much smaller that the diameter of the particles.[36] Theoretical work of this particular nanoparticle system is required to gain a better understanding of the observed optical spectra. Additionally, theoretical models would help to predict near field enhancements patterns. If this DNC system has more regions of enhancement they might be preferable for surface-enhanced spectroscopies.

4.3.3 Heterometallic DNCs

As the native oxide over aluminum provides a definitive minimum gap distance, this fabrication technique allows for the creation of DNC structures with different metals. By using a metal that does not oxidize, like Au, the gap distance may theoretically be shortened. Heterogeneous DNC were fabricated by first depositing a 25 nm AlNC array. On the opposing side of the template, a 3 nm Cr adhesion layer was deposited followed by the deposition of 25 nm of Au, resulting in an AlNC and an AuNC facing each other (Figure 4.4C). The particles were then characterized using UV/Vis absorption spectroscopy and SEM (Figure 4.4). For comparison, the unpolarized optical spectrum of a 350 nm AuNC is shown in Figure 4.3A. All of the peaks for the AuNCs are red-shifted relative to the LSPR response of 350 nm AlNCs shown in Figure 4.2A. For the AuNC array, short axis and long axis dipole resonances appear at 1335 nm and 2040 nm, respectively. The LSPR mode at 675 shows a strong extinction when light is polarized along the short axis of the

AuNC array, and is weaker when the light is polarized along the long axis (data not shown). This mode has been attributed to an out of plane dipole in previous work.[40] The absorbance starting around 450 nm is due to the interband transition of gold and is not from a plasmon resonance.

Again, separating two NCs by a small gap introduces drastic changes to the optical response of this heterodimer structure. In the unpolarized UV/Vis spectrum, a broad LSPR is observed at 1610 nm, with a less intense higher order mode at 700 nm (Figure 4.4B). To aid in the visualization of the heterogeneous DNC structures, SEM images were false colored to help distinguish between the Au and Al (Figure 4.4C). The diameter and backbone thicknesses of these structures are nearly identical to the Al/Al DNC structures; additionally, the slight asymmetric overlap is very similar as well. The similar shape and structures allows us to analyze the effect that exchanging the metal has on the plasmonic properties of the structure.

The polarized UV/Vis/NIR spectra of an Al/Au DNC array is presented in Figure 4.5 and reveals a significant change in the plasmonic behavior of the structure. To aid in the correlation of polarized extinction spectra with Al/Au DNC geometry, the polarization angles have been overlaid on an SEM image (Figure 4.5C). The long axis of the Al/Au DNC refers to axis that splits the structure where the tips overlap (light red arrow). The short axis is the perpendicular axis (dark blue). As with the Al/Al DNC, the heterogeneous Al/Au DNC exhibits two strong dipoles in the NIR region that can be selected by the changing the incident polarization. A maximum extinction at 1835 nm is excited by 130˚ polarized light. A second prominent LSPR mode at 1430 nm is excited with 40˚ polarized light. If the 130˚ polarized light is attributed to a “long axis” mode, then it is blue-shifted

relative to a AuNC long axis mode (2040 nm). Attributing the 40˚ polarization to a "short axis" mode, this LSPR is red-shifted relative to a AuNC short axis mode (1335 nm). Relative to an array of Al/Al DNCs, both these modes are red-shifted.

The true long (100˚) and short (190˚) axis polarization of the Al/Au DNC exhibit broad LSPR modes at 1575 nm and 1760 nm, respectively. Compared to the Al/Al DNC array, all of the observed LSPR modes have red-shifted. The red-shift of the LSPR wavelength is most likely due to the changing of plasmonic metal and not a change in the gap distance separation.

A more complicated relationship between polarization angle, wavelength maxima, and extinction is observed in the visible region of the spectra (Figure 4.5B). The 40˚, 160˚, and 190˚ polarization angles all exhibit a LPSR response at 700 nm and are within 30˚ of the short axis of the Al/Au DNC structure. The 130˚ polarization angle shows a weak extinction at 755 nm, this extinction continues to decrease in intensity as the polarization angle overlaps with the long axis of the Al/Au DNC (100˚). The 130˚ polarization shows little extinction in the 500-1100 nm range. At shorter wavelengths (<500 nm), every polarization angle exhibits an increased extinction. Au will absorb light below this wavelength because of its interband transition, but its absorption would not depend on the incident polarization. There is a distinct polarization-dependent response at wavelengths below 500 nm that must be the result of the Al portion of the Al/Au DNC.

So far the evidence for a gap separated heterometallic and homometallic plasmonic structures is purely based off of spectroscopic data. However, a case may still be made that what we are observing is the result of plasmonic coupling. There is a clear shift in LSPR wavelength in a DNC array system versus a typical NC array (regardless of metal

composition).[36] A significant broadening of the LSPR is observed, which is also indicative of plasmonic coupling.[34, 35] Admittedly, more data is required to support this assertion. Energy dispersion spectroscopy (EDS) in a scanning transmission electron microscope would provide microscopic evidence for gap separated structures. Additionally, finite difference time domain (FDTD) simulations would help to understand what is happening in the near field enhancement.

4.4 Conclusions

NTL was used to successfully produce gap separated plasmonic structures. Using a copper mask template, lithography homoplasmonic and heteroplasmonic nanocrescent dimer structures were fabricated over large substrate areas. These dimer nanocrescents had a gap separation defined by the native alumina layer that forms over the Al metal, resulting in gap distances of ~3nm. The DNC structures resulted in complex polarization-dependent optical responses that were highly dependent on the metal composition of the system. Al/Al DNC structures exhibited dipole and quadrupole LSPR modes that were significantly red-shifted relative to a single AlNC system. These plasmonic modes exhibited predictable polarization-dependent optical responses. A heterometallic DNC composed of Au and Al exhibits complex polarization-dependent optical response. Due to the small gap size, these particles are predicted to have large electric field enhancements that can be tuned using the incident polarization.

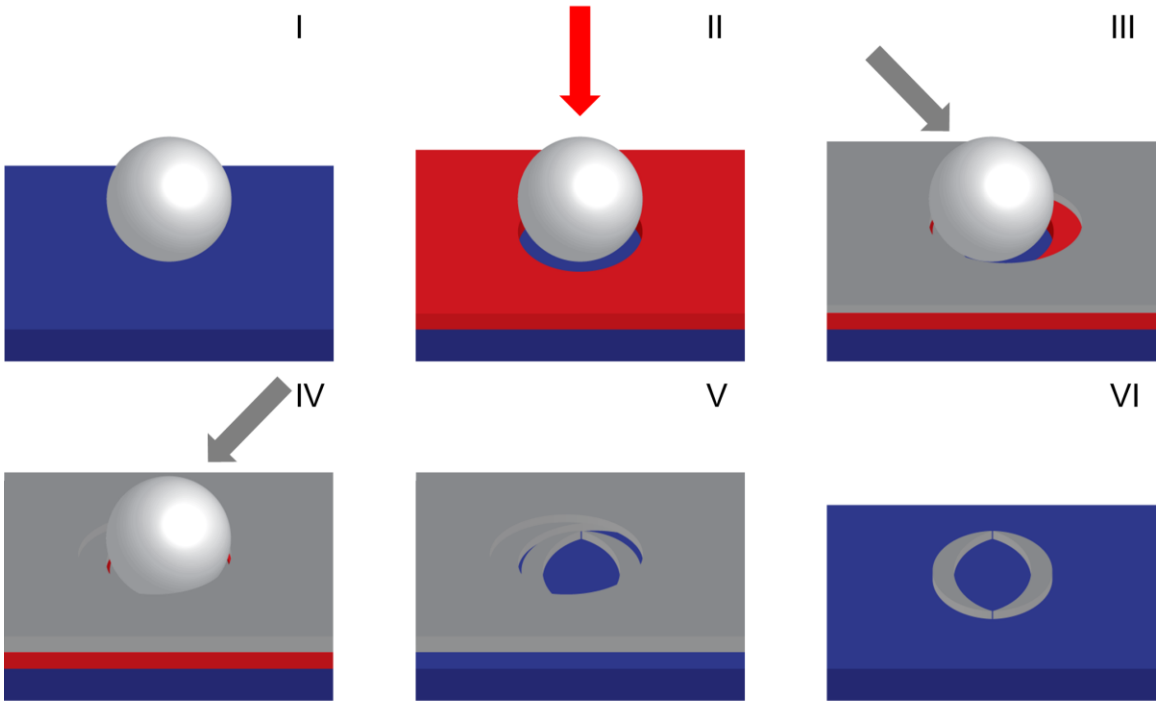

Figure 4.1 Schematic representation of the dimer nanocrescent fabrication process. I) PS templates are deposited on a substrate, II) followed by 60 nm of copper normal to the surface. III) A 25 nm aluminum film is deposited at a 40˚ relative to surface normal. IV) A second 25 nm metallic film is deposited on the opposing side of the PS template, at an angle 40˚ relative to surface normal. For hetero metallic DNCs this second metal film is Au (with a Cr adhesion layer). V) The copper film is removed by quickly submersing the substrates in nitric acid. VI) The films of Al (or Al and Au) are removed via sonication and scotch tape removal resulting in dimer nanocrescent structures.

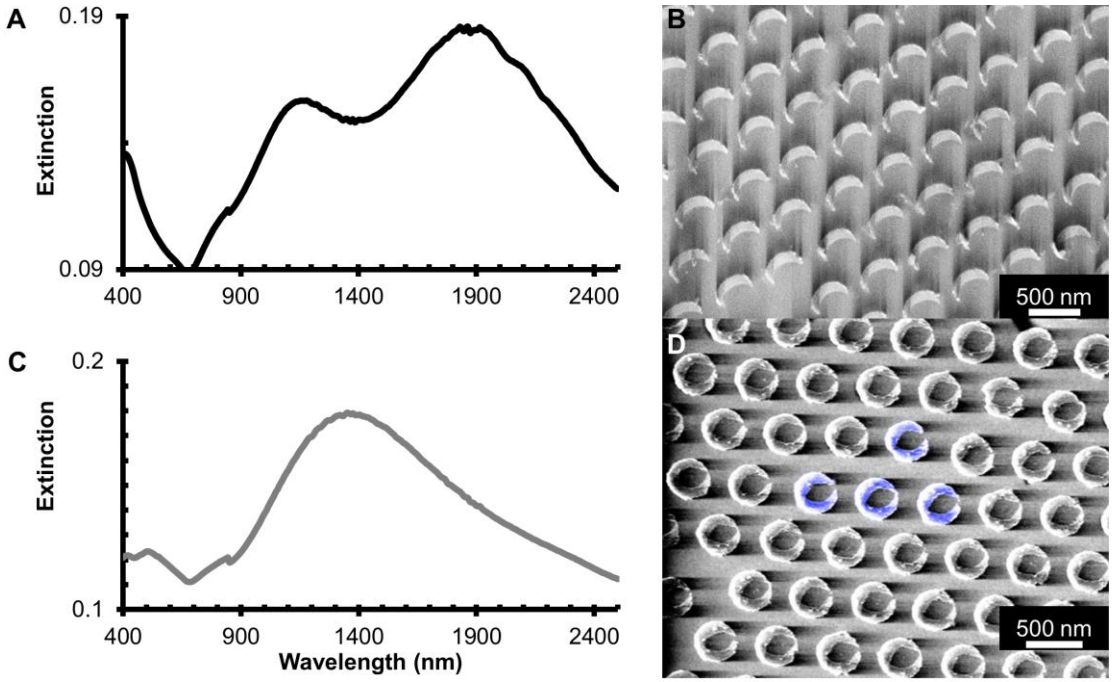

Figure 4.2 DNC arrays exhibit a drastically different optical response than AlNC arrays. A) Unpolarized UV/Vis spectrum of 350 nm AlNCs showing two distinct dipoles corresponding to short (1095 nm) and long (1900 nm) axis resonances and accompanying SEM (B). C) Unpolarized UV/Vis spectrum of 350 nm DNC fabricated such that their tips overlap as seen in the SEM (D).

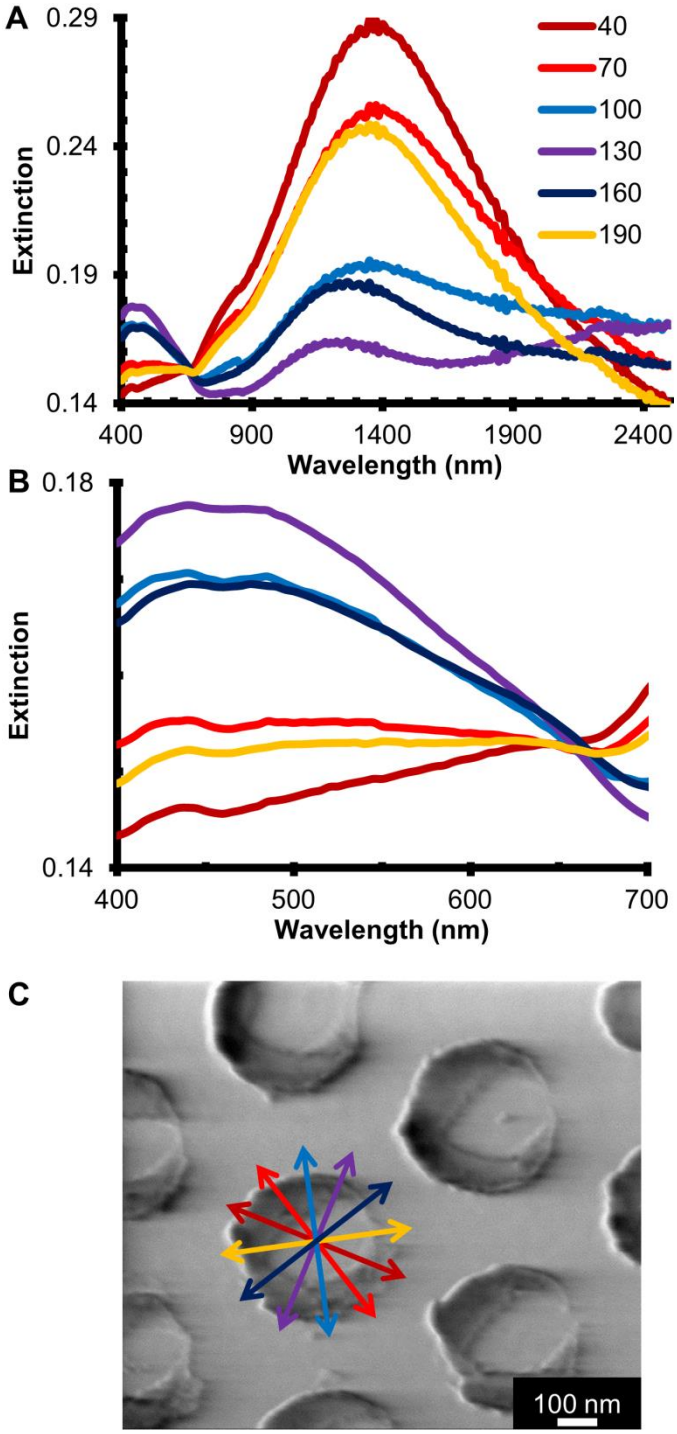

Figure 4.3 Polarized spectra of DNC arrays shows their complex optical response. A/B) Polarized Vis/NIR spectra of 350nm Al/Al DNC showing the polarization dependence of the different resonant modes. C) SEM image with the polarization angles from the UV/Vis/NIR spectra overlaid on top.

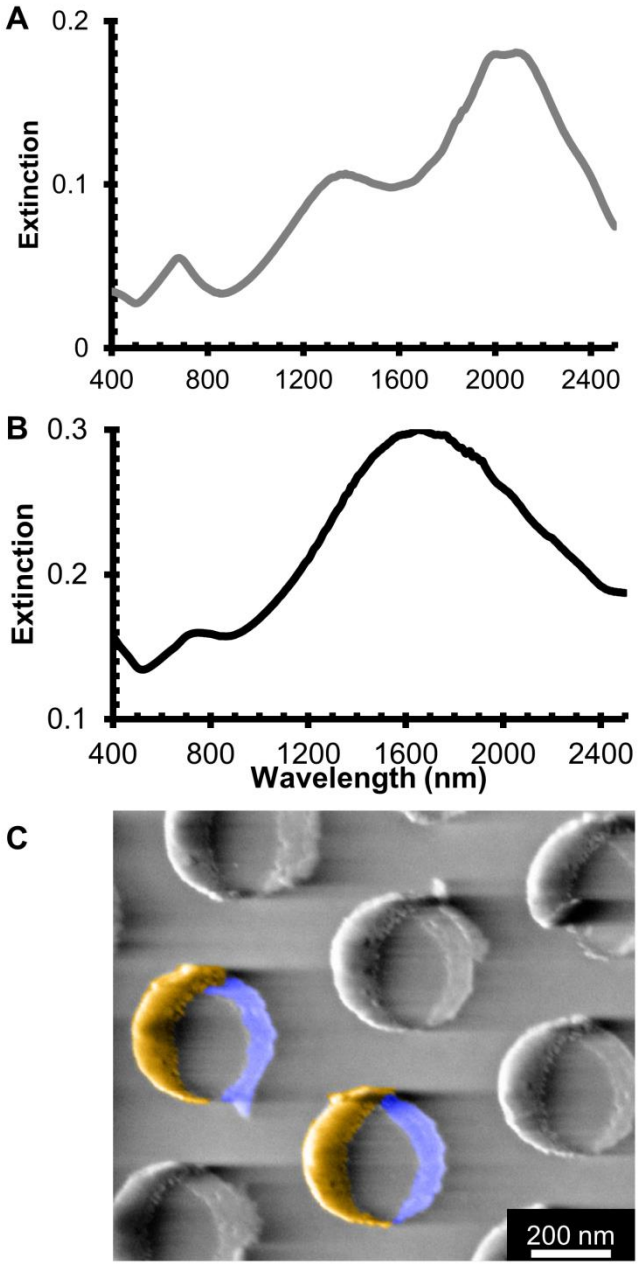

Figure 4.4 Heterometallic DNC structures are easily fabricated using NTL. A) Vis/NIR spectrum of an array of AuNCs with a 350 nm tip-to-tip diameter, a long and short axis dipole at 1335 nm and 2040 nm, respectively, are clearly present. B) Unpolarized Vis/NIR spectrum of an array of Al/Au DNC structures. C) SEM of Al/Au DNC with a diameter of 350 nm, false coloring used to distinguish Al (blue) from Au (yellow) nanoparticle.

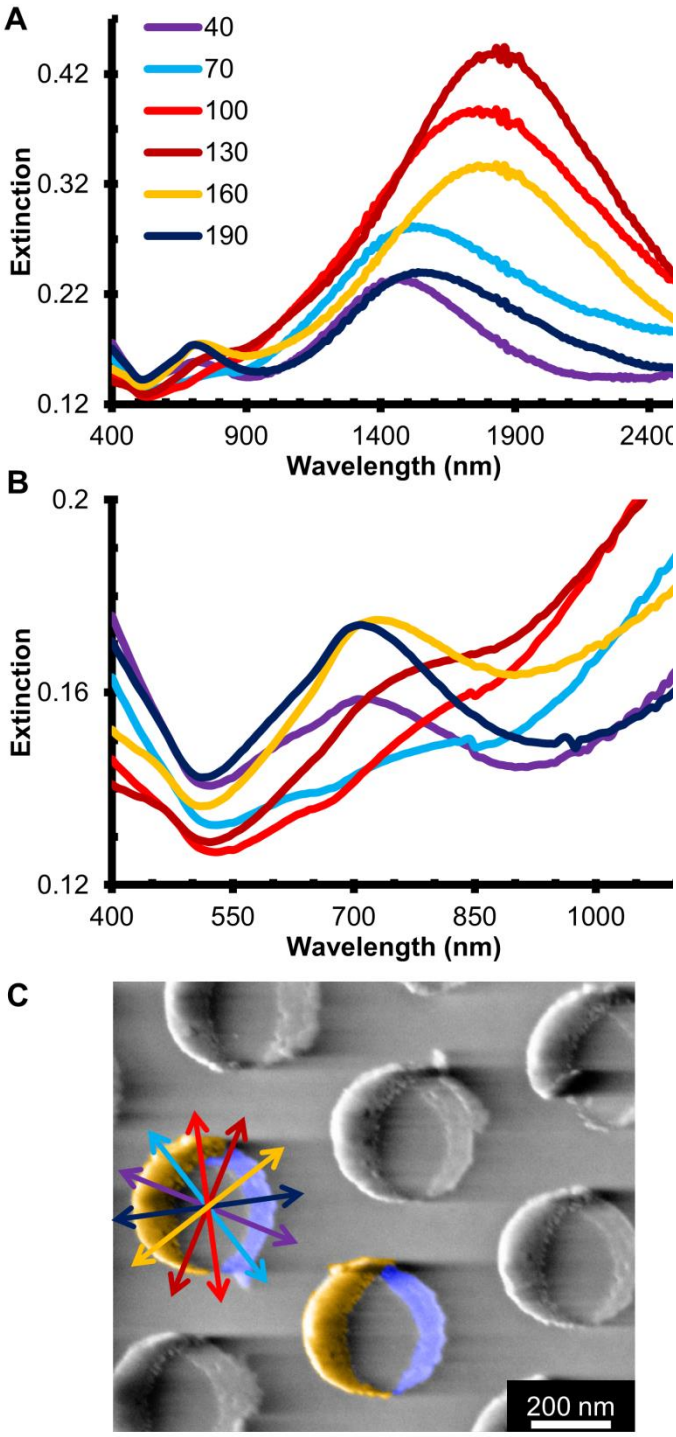

Figure 4.5 Polarized optical response of heterometallic DNC reveals complex higher order modes. A/B) Polarized Vis/NIR spectra of a 350 nm diameter Al/Au DNC array shows a complex relationship between polarization angle and LSPR wavelength especially at visible wavelengths (B). The polarization angles from the UV/Vis/NIR overlaid onto the SEM image is shown in (C).

4.5 References

(1) Novotny, L.; Bian, R. X.; Xie, X. S. Theory of Nanometric Optical Tweezers. *Phys. Rev. Lett.* **1997**, *79*, 645-648.

(2) Zhang, M.; Large, N.; Koh, A. L.; Cao, Y.; Manjavacas, A.; Sinclair, R.; Nordlander, P.; Wang, S. X. High-Density 2D Homo- and Hetero- Plasmonic Dimers with Universal Sub-10-nm Gaps. *ACS Nano* **2015**, *9*, 9331-9339.

(3) Berweger, S.; Atkin, J. M.; Olmon, R. L.; Raschke, M. B. Light on the Tip of a Needle: Plasmonic Nanofocusing for Spectroscopy on the Nanoscale. *J. Phys. Chem. Lett.* **2012**, *3*, 945-952.

(4) Lermusiaux, L.; Sereda, A.; Portier, B.; Larquet, E.; Bidault, S. Reversible Switching of the Interparticle Distance in DNA-Templated Gold Nanoparticle Dimers. *ACS Nano* **2012**, *6*, 10992-10998.

(5) Haynes, C. L.; McFarland, A. D.; Smith, M. T.; Hulteen, J. C.; Van Duyne, R. P. Angle-Resolved Nanosphere Lithography: Manipulation of Nanoparticle Size, Shape, and Interparticle Spacing. *J. Phys. Chem. B* **2002**, *106*, 1898-1902.

(6) Wustholz, K. L.; Henry, A.-I.; McMahon, J. M.; Freeman, R. G.; Valley, N.; Piotti, M. E.; Natan, M. J.; Schatz, G. C.; Duyne, R. P. V. Structure−Activity Relationships in Gold Nanoparticle Dimers and Trimers for Surface-Enhanced Raman Spectroscopy. *J. Am. Chem. Soc.* **2010**, *132*, 10903-10910.

(7) Suh, J. Y.; Odom, T. W. Nonlinear Properties of Nanoscale Antennas. *Nano Today* **2013**, *8*, 469-479.

(8) Behr, N.; Raschke, M. B. Optical Antenna Properties of Scanning Probe Tips: Plasmonic Light Scattering, Tip−Sample Coupling, and Near-Field Enhancement. *J. Phys. Chem. C* **2008**, *112*, 3766-3773.

(9) Berweger, S.; Nguyen, D. M.; Muller, E. A.; Bechtel, H. A.; Perkins, T. T.; Raschke, M. B. Nano-Chemical Infrared Imaging of Membrane Proteins in Lipid Bilayers. *J. Am. Chem. Soc.* **2013**, *135*, 18292-18295.

(10) Thacker, V. V.; Herrmann, L. O.; Sigle, D. O.; Zhang, T.; Liedl, T.; Baumberg, J. J.; Keyser, U. F. DNA Origami Based Assembly of Gold Nanoparticle Dimers for Surface-Enhanced Raman Scattering. *Nat. Commun.* **2014**, *5*.

(11) Zhou, X.; Deeb, C.; Kostcheev, S.; Wiederrecht, G. P.; Adam, P.-M.; Béal, J.; Plain, J.; Gosztola, D. J.; Grand, J.; Félidj, N.; Wang, H.; Vial, A.; Bachelot, R. Selective Functionalization of the Nanogap of a Plasmonic Dimer. *ACS Photonics* **2015**, *2*, 121-129.

(12) Bidault, S.; Devilez, A.; Ghenuche, P.; Stout, B.; Bonod, N.; Wenger, J. Competition

between Förster Resonance Energy Transfer and Donor Photodynamics in Plasmonic Dimer Nanoantennas. *ACS Photonics* **2016**, *3*, 895-903.

(13) Busson, M. P.; Rolly, B.; Stout, B.; Bonod, N.; Larquet, E.; Polman, A.; Bidault, S. Optical and Topological Characterization of Gold Nanoparticle Dimers Linked by a Single DNA Double Strand. *Nano Lett.* **2011**, *11*, 5060-5065.

(14) Cha, H.; Yoon, J. H.; Yoon, S. Probing Quantum Plasmon Coupling Using Gold Nanoparticle Dimers with Tunable Interparticle Distances Down to the Subnanometer Range. *ACS Nano* **2014**, *8*, 8554-8563.

(15) Dewi, M. R.; Gschneidtner, T. A.; Elmas, S.; Ranford, M.; Moth-Poulsen, K.; Nann, T. Monofunctionalization and Dimerization of Nanoparticles Using Coordination Chemistry. *ACS Nano* **2015**, *9*, 1434-1439.

(16) Hofmann, A.; Schmiel, P.; Stein, B.; Graf, C. Controlled Formation of Gold Nanoparticle Dimers Using Multivalent Thiol Ligands. *Langmuir* **2011**, *27*, 15165-15175.

(17) Kühler, P.; Roller, E.-M.; Schreiber, R.; Liedl, T.; Lohmüller, T.; Feldmann, J. Plasmonic DNA-Origami Nanoantennas for Surface-Enhanced Raman Spectroscopy. *Nano Lett.* **2014**, *14*, 2914-2919.

(18) Lee, D.; Yoon, S. Gold Nanocube–Nanosphere Dimers: Preparation, Plasmon Coupling, and Surface-Enhanced Raman Scattering. *J. Phys. Chem. C* **2015**, *119*, 7873-7882.

(19) Yang, S.-C.; Kobori, H.; He, C.-L.; Lin, M.-H.; Chen, H.-Y.; Li, C.; Kanehara, M.; Teranishi, T.; Gwo, S. Plasmon Hybridization in Individual Gold Nanocrystal Dimers: Direct Observation of Bright and Dark Modes. *Nano Lett.* **2010**, *10*, 632-637.

(20) Aeschlimann, M.; Bauer, M.; Bayer, D.; Brixner, T.; Garcia de Abajo, F. J.; Pfeiffer, W.; Rohmer, M.; Spindler, C.; Steeb, F. Adaptive Subwavelength Control of Nano-Optical Fields. *Nature* **2007**, *446*, 301-304.

(21) Haynes, C. L.; Van Duyne, R. P. Dichroic Optical Properties of Extended Nanostructures Fabricated Using Angle-Resolved Nanosphere Lithography. *Nano Lett.* **2003**, *3*, 939-943.

(22) Swartz, M.; Rodriguez, M.; Quast, A. D.; Cooper, C. T.; Blair, S.; Shumaker-Parry, J. S. Aluminum Nanocrescent Plasmonic Antennas Fabricated by Copper Mask Nanosphere Template Lithography. *J. Phys. Chem. C* **2016**, *120*, 20597-20603.

(23) Bukasov, R.; Shumaker-Parry, J. S. Highly Tunable Infrared Extinction Properties of Gold Nanocrescents. *Nano Lett.* **2007**, *7*, 1113-1118.

(24) Bukasov, R.; Shumaker-Parry, J. S. Silver Nanocrescents with Infrared Plasmonic

Properties As Tunable Substrates for Surface Enhanced Infrared Absorption Spectroscopy. *Anal. Chem.* **2009**, *81*, 4531-4535.

(25) Langhammer, C.; Schwind, M.; Kasemo, B.; Zorić, I. Localized Surface Plasmon Resonances in Aluminum Nanodisks. *Nano Lett.* **2008**, *8*, 1461-1471.

(26) Aizpurua, J.; Hanarp, P.; Sutherland, D. S.; Käll, M.; Bryant, G. W.; García de Abajo, F. J. Optical Properties of Gold Nanorings. *Phys. Rev. Lett.* **2003**, *90*, 057401.

(27) Shumaker-Parry, J. S.; Rochholz, H.; Kreiter, M. Fabrication of Crescent-Shaped Optical Antennas. *Adv. Mater.* **2005**, *17*, 2131-2134.

(28) Moitra, P.; Slovick, B. A.; li, W.; Kravchencko, I. I.; Briggs, D. P.; Krishnamurthy, S.; Valentine, J. Large-Scale All-Dielectric Metamaterial Perfect Reflectors. *ACS Photonics* **2015**, *2*, 692-698.

(29) Chen, K.; Rajeeva, B. B.; Wu, Z.; Rukavina, M.; Dao, T. D.; Ishii, S.; Aono, M.; Nagao, T.; Zheng, Y. Moiré Nanosphere Lithography. *ACS Nano* **2015**, *9*, 6031-6040.

(30) Chan, G. H.; Zhao, J.; Hicks, E. M.; Schatz, G. C.; Van Duyne, R. P. Plasmonic Properties of Copper Nanoparticles Fabricated by Nanosphere Lithography. *Nano Lett.* **2007**, *7*, 1947-1952.

(31) Chan, G. H.; Zhao, J.; Schatz, G. C.; Duyne, R. P. V. Localized Surface Plasmon Resonance Spectroscopy of Triangular Aluminum Nanoparticles. *J. Phys. Chem. C* **2008**, *112*, 13958-13963.

(32) Haynes, C. L.; Van Duyne, R. P. Nanosphere Lithography: A Versatile Nanofabrication Tool for Studies of Size-Dependent Nanoparticle Optics. *J. Phys. Chem. B* **2001**, *105*, 5599-5611.

(33) McPeak, K. M.; Jayanti, S. V.; Kress, S. J. P.; Meyer, S.; Iotti, S.; Rossinelli, A.; Norris, D. J. Plasmonic Films Can Easily Be Better: Rules and Recipes. *ACS Photonics* **2015**, *2*, 326-333.

(34) Haynes, C. L.; McFarland, A. D.; Zhao, L.; Van Duyne, R. P.; Schatz, G. C.; Gunnarsson, L.; Prikulis, J.; Kasemo, B.; Käll, M. Nanoparticle Optics: The Importance of Radiative Dipole Coupling in Two-Dimensional Nanoparticle Arrays. *J. Phys. Chem. B* **2003**, *107*, 7337-7342.

(35) Vazquez-Mena, O.; Sannomiya, T.; Villanueva, L. G.; Voros, J.; Brugger, J. Metallic Nanodot Arrays by Stencil Lithography for Plasmonic Biosensing Applications. *ACS Nano* **2011**, *5*, 844-853.

(36) Jain, P. K.; El-Sayed, M. A. Plasmonic Coupling in Noble Metal Nanostructures. *Chem. Phys. Lett.* **2010**, *487*, 153-164.

(37) Muskens, O. L.; Giannini, V.; Sánchez-Gil, J. A.; Gómez Rivas, J. Optical Scattering Resonances of Single and Coupled Dimer Plasmonic Nanoantennas. *Opt. Express* **2007**, *15*, 17736-17746.

(38) Hentschel, M.; Utikal, T.; Giessen, H.; Lippitz, M. Quantitative Modeling of the Third Harmonic Emission Spectrum of Plasmonic Nanoantennas. *Nano Lett.* **2012**, *12*, 3778-3782.

(39) Cooper, C. T.; Rodriguez, M.; Blair, S.; Shumaker-Parry, J. S. Polarization Anisotropy of Multiple Localized Plasmon Resonance Modes in Noble Metal Nanocrescents. *J. Phys. Chem. C* **2013**, *118*, 1167-1173.

(40) Cooper, C. T.; Rodriguez, M.; Blair, S.; Shumaker-Parry, J. S. Polarization Anisotropy of Multiple Localized Plasmon Resonance Modes in Noble Metal Nanocrescents. *J. Phys. Chem. C* **2014**, *118*, 1167-1173.

(41) Rodriguez, M.; Furse, C.; Shumaker-Parry, J. S.; Blair, S. Scaling the Response of Nanocrescent Antennas into the Ultraviolet. *ACS Photonics* **2014**, *1*, 496-506.

(42) Benjamin, P.; Weaver, C. The Adhesion of Evaporated Metal Films on Glass. *P. Roy. Soc. Lond. A MAT.* **1961**, *261*, 516-531.

CHAPTER 5

INFLUENCE OF ALUMINUM CONTENT ON PLASMONIC BEHAVIOR OF MG-AL ALLOY THIN FILMS

The following work is the result of collaboration in the Materials Science Research Engineering Center (MRSEC) and is reprinted with permission from Appusamy, K.; Swartz, M.; Nahata, A.; Shumaker-Parry, J.; Guruswamy, S. *Opt. Mater. Express* **2016**, DOI 10.1364/OME.6.003180. The experimental work was carried out by Dr. Appusamy and myself. The deposition of magnesium and aluminum as well as characterization of the films by ellipsometry and atomic force microscopy (AFM) was performed by Dr. Appusamy. Preparation of the polystyrene templates as well as characterization and interpretation of spectroscopic data of the nanotriangles was performed by me. The introduction, conclusion, methods, results and discussion section pertaining to the deposition of the metal films and their characterization by ellipsometry were written by Dr. Appusamy. While the methods, results, and discussion section relating to the nanotriangles were written by me.

5.1 Abstract

The influences of deposition rate and alloying with aluminum (0 to 65 at.%) on the structure and optical properties of magnesium films on quartz are examined. Results show that increasing the deposition rate improves the plasmonic figure of merit (FOM) values,

and decreases the surface roughness and grain size. Addition of Al to Mg blue shifts the localized surface plasmon (LSP) figure of merit peak position and improves LSP FOM values over portions of the ultraviolet (UV) region. Nanotriangles (NTs) of Mg and Mg-Al on quartz were fabricated using colloidal lithography. Mg-Al NTs show improved LSP resonance (LSPR) response compared to Mg particles due to improved structural integrity.

5.2 Introduction

The use of plasmonics in the UV spectral range has often been overlooked, but is of interest as many important chemical/biochemical reaction steps are associated with these energies. UV plasmonic structures are therefore very attractive for use in enhanced chemical synthesis and other photochemical processes in addition to UV spectroscopy for sensing and detection as well as energy harvesting applications.[1] Al is often considered the best plasmonic metal across the UV range due to its high plasma frequency and absence of interband transitions in this region.[2] However, Al suffers from drawbacks including a large electron damping factor and the formation of a very stable oxide layer that is of concern in both fabrication and applications. In our earlier work[3, 4], it was demonstrated that Mg also has potential as an alternative plasmonic material in the UV region from 280-400 nm. For instance, the figure of merit of localized surface plasmons using Mg films is more than 50% higher than with Al films at near-UV wavelengths.

Researchers[5, 6] have proposed that alloying metals (like Cu, Ag, Au) with a small volume fraction of another metal modifies the metal's reflection and absorption properties as observed by spectral characterization. Alloying of monovalent metals such as Ag and Au with bivalent or trivalent metals increases the free electron density. This raises the Fermi level which in turn increases the d→sp transition energy. Using Finite-Difference

Time-Domain (FDTD) calculations, Chowdhury et al.[7] showed shifting of the interband transition in Ag by the addition of trivalent metal Al. Bobb et al.[8] have shown shifts in interband transitions in Au by alloying with bivalent transition metals (e.g. Cd, Zn).[8] Cd and Zn contribute one extra electron to the free-electron plasma in Au thereby increasing the electron density. In the case of noble metal alloy thin-films, the dielectric function can be manipulated by tuning the concentration of two individual metals, which in turn modifies the strength of the polarization (ε_1) induced by an external electric field and the losses (ε_2) in the material due to absorption.[9] In addition, researchers[10-12] have shown that by adding small amounts of Al into Ag, the morphology and optical properties of ultrathin Ag films can be significantly improved. In this work, the influence of alloying Mg with Al on the structural characteristics and the optical behavior of Mg is examined. This work also examined the localized surface plasmon resonance (LSPR) response of Mg-Al alloy nanotriangles on quartz substrates compared to pure Mg and pure Al nanotriangles.

5.3 Experimental Section

Mg-Al alloy thin films were deposited on fused quartz substrates by co-sputtering of Mg and Al using magnetron sputtering in an ultrahigh vacuum (UHV) chamber. Air Products Research grade argon gas (>99.9995% purity) was used for the sputtering process. The Mg target was machined from 99.99+% purity Mg discs that had a diameter of 50 mm and thickness of 6.25 mm. The Al sputtering target, with a diameter of 50 mm, thickness of 6.25 mm, and a purity of 99.9995%, was obtained from Alfa Aesar.

The sputtering chamber was evacuated using a turbo pump to a base vacuum level of $< 3 \times 10^{-7}$ Torr. Argon gas was then introduced at a flow rate of 3.0×10^{-2} cc/min and maintained for 3 hours with the turbo pump on. The sputtering was then carried out at a

pressure of 2.5 x 10^{-3} Torr. Al and Mg films were co-sputtered using an Advanced Energy 500 W DC sputtering power supply and a 500 W RF power supply, respectively. The targets were sputter cleaned for 5 minutes prior to each deposition to remove the oxide film on the target surface. Mg-Al films were deposited on optically smooth surfaces, 25 mm × 25 mm polished fused quartz substrates. The compositions of the alloys were controlled by varying the power for Al and Mg sputtering.

The samples were retained in the deposition chamber under vacuum until their transfer to the ellipsometry measurement system. For transfer, the samples were removed from the deposition chamber and sealed in polyethylene bags under an argon atmosphere. The transfer time was typically ~30 minutes. The optical measurements were then carried out using a Variable Angle Spectroscopic Ellipsometer (VASE) made by J.A. Woollam Co.[13, 14] Since the samples were briefly exposed to atmosphere before and during the VASE measurement, we expect the formation of a few nm thick MgO-Al_2O_3 on the thin metal film surface. We used a Drude model for fitting the optical properties and considered the Mg alloy film and substrate in the model. Measurements in this work were made over the wavelength range of 250 to 1700 nm at incident angles of 70° and 75°.

The surface morphology of the films was analyzed using a high-resolution FEI Nova Nano 630 Scanning Electron Microscope (Nova NanoSEM™). The surface roughness of the films was analyzed using a Bruker Dimension ICON-PT atomic force microscope (AFM), which was used in the contact mode with a nominal tip radius of curvature of 2 nm. The average compositions of the alloy thin films were analyzed using Energy Dispersive Spectroscopy (EDS) in a Nova NanoSEM™. The standardless quantification routine of the EDAX Genesis software was used for the analysis. Three

measurements were made on each of the samples in adjacent location to obtain standard deviation of the measured composition. Three measurements were made on the sample in adjacent location to obtain standard deviation of the measured composition. The crystalline structure and crystallographic texture were analyzed using X-ray diffraction measurements using a Siemens D5000 X-ray diffractometer.

5.3.1 Fabrication of nanostructures

From the optical constant measurements, it was observed that Mg-Al alloy films have improved LSP figure of merit values compared to Al in some portions of the UV range. To examine the localized surface plasmon (LSP) response of Mg-Al alloy films, nanotriangles were fabricated using nanosphere lithography[15], also commonly known as colloidal lithography. Unlike electron beam lithography (EBL), it is inexpensive and is easily applied over large substrate areas. This fabrication method also involves a very limited number of steps, lowering the risk of oxidation of the Mg film. Nevertheless, the alloy films would be compatible with other patterning methods making use of a lift-off step, such as electron beam lithography.

5.3.1.1 Preparation of close-packed polystyrene (PS) beads

Water with a resistivity of about 18 MΩ obtained after passing through a Barnstead NANOpure® Diamond filtration system was used. Chemicals used were reagent grade and purchased from Fisher Scientific unless otherwise noted. Fused silica (quartz) slides were first cleaned in piranha acid, 3:1 concentrated sulfuric acid (Macron Fine Chemicals), 30% H_2O_2, for 45 min followed by sonication in a basic solution (5:1:1 water, concentrated ammonium hydroxide, 30% H_2O_2) for 1 hour at 60°C. Slides were then placed under water

in a petri dish that was elevated by 5°. Aldehyde functionalized polystyrene (PS) macrospheres (Life Technologies) were diluted 50:50 in 200 proof ethanol (Decon) and introduced into the petri dish using a microliter syringe pump. Once a monolayer of PS beads was formed at the air-water interface, the water was pumped out of the petri dish using a peristaltic pump, leaving behind a close-packed monolayer on the clean quartz slides and the slides were left to dry in an ambient environment.[16, 17] *(Caution: Piranha solution is a strong oxidizing agent, which has been known to detonate spontaneously upon contact with organic material, and should be handled with extreme care.)*

5.3.1.2 Fabrication of nanotriangles (NTs)

After drying, a thin film of required material (Mg or Al) of thickness 50 nm was magnetron sputter deposited (described in section 2) on the quartz slides containing a monolayer of close-packed PS beads of desired size. The PS beads were selectively removed using adhesive tape. The resulting size of the nanotriangles was varied by using different sizes of the PS beads.[18]

5.4 Results and Discussion

5.4.1 Influence of deposition rate

Mg films were deposited at different deposition rates (1.8, 5.2, and 7.0 Å/s) on fused quartz substrates. The nominal thicknesses of the Mg films were 100 nm as measured using stylus profilometry. Various deposition rates were achieved by changing the RF sputtering power for Mg deposition from 30 to 84 W. Figure 5.1 shows AFM images of Mg films prepared with different deposition rates of (a) 1.8, (b) 5.2, and (c) 7.0 Å/s. The RMS roughness (R_q) values observed for Mg films with different deposition rates (1.8, 5.2,

and 7.0 Å/s) are 3.7, 2.7, 2.3 nm, respectively. R_q values are the standard deviations from the mean plane and represent the roughness. The result suggests that surface roughness values tend to decrease as the deposition rate increases.

Quantification of the grain size was difficult because of the change in morphology of the film structure at the higher deposition rate, but a decrease in the grain size of the Mg film with an increase in the deposition rate could be qualitatively seen (Figure 5.1). Other work on metallic thin films has shown that a decrease in grain size can be attained by (i) faster deposition rate of the metallic film which reduces the time that metal atoms can diffuse on the substrate and leads to smaller grains, especially when the substrate is at ambient temperature conditions[19, 20], and (ii) the presence of residual gas molecules present in the deposition chamber, especially for metals with high reactivity like Al and Mg, which tend to reduce grain growth. Here the depositions of Mg films were carried out in a UHV chamber with a base pressure of $< 2 \times 10^{-7}$ Torr, so the probability of the formation of an oxide layer and pinning of the grain boundaries is very low.[21]

Figure 5.2(a) and (b) shows the optical constants ε_1 and ε_2 for the Mg films as a function of incident wavelength, where ε_1 (Eq. 5.1) and ε_2 (Eq. 5.2) are the real and imaginary parts of the direction function (Eq. 5.3).[13, 14, 22] A more meaningful measure of the utility of a specific metal for plasmonics applications at optical frequencies can be obtained by considering a figure of merit (FOM) that is relevant for the specific application. In the case of localized surface plasmon (LSP) implementations, this is commonly given by $FOM_{LSP} = -\varepsilon_1/\varepsilon_2$, while for surface plasmon polaritons (SPP) applications, it is given by $FOM_{SPP} = \beta_1/\beta_2$, where β (Eq. 5.4) is the complex propagation constant of the SPP at the metal/air interface, and β_1 and β_2 are the real and imaginary components, respectively.[24]

$$\varepsilon_1 = n^2 - k^2 \tag{5.1}$$

$$\varepsilon_2 = 2nk \tag{5.2}$$

$$\varepsilon = \varepsilon_1 + i\varepsilon_2 \tag{5.3}$$

$$\beta = \sqrt{\frac{\varepsilon_1 + i\varepsilon_2}{(\varepsilon_1 + i\varepsilon_2) + 1}} \tag{5.4}$$

With increasing deposition rate, ε_1 does not vary significantly. In the case of ε_2, the Mg films prepared with deposition rates of 5.2 and 7.0 Å/s, show lower losses when compared to the Mg film with a deposition rate of 1.8 Å/s. Reduction in grain size increases the area of grain boundaries which act as electron scattering centers.[25, 26] On the contrary, in the case of Figure 5.2 (b), the Mg films with finer grain size (5.2 and 7.0 Å/s) seem to have lower losses when compared to the film with bigger grain size (1.8 Å/s). However, there is a reduction in surface roughness of the films which contributes to the improvement in the FOM_{LSP} values.

Figure 5.2(c) shows a plot of FOM_{LSP} versus wavelength and Figure 5.2(d) shows a plot of FOM_{SPP} versus wavelength observed in the case of Mg films deposited at different rates. The Mg film prepared with a 7.0 Å/s deposition rate gives higher FOM_{LSP} of about 8.3 at 370 nm, when compared to 7.9 at 380 nm (5.2 Å/s) and 6.6 at 360 nm (1.8 Å/s). FOM_{SPP} values are also significantly improved for films with higher deposition rates (5.2 and 7.0 Å/s) when compared to the lower deposition rate (1.8 Å/s) especially at wavelengths beyond 300 nm (Figure 5.2(d)).

5.4.2 Optical response of Mg-Al alloy thin films

The optical responses of Mg-Al alloy films are presented in this section. For the purpose of analysis, the Mg-Al alloy thin films were divided into two categories: (i) Mg-rich (Mg > 50 at.%) and (ii) Al-rich (Al > 50 at.%). The nominal thicknesses of all the Mg alloy thin films were 100 nm.

5.4.3 Mg-Al alloy thin films

Two intermetallic compound phases are observed in the Al-Mg binary system, namely Al_3Mg_2 (β), and $Al_{12}Mg_{17}$ (γ). Al_3Mg_2 has a Cd_2Na type structure while the $Al_{12}Mg_{17}$ phase has an α-Mn (A12) type structure (Table 5.1).[27] Preparation of Al_3Mg_2 and $Al_{12}Mg_{17}$ films of exact stoichiometry using the co-sputtering approach required several trials and was challenging. In this work, Mg-Al films with Al content in the 0 to 65 at.% range were examined. The films were prepared by varying relative sputtering powers used for Mg and Al sputtering. Table 5.2 shows the compositions of various films obtained and the sputtering powers used for Mg and Al. Figure 5.3 shows the XRD patterns of both Mg-rich and Al-rich Mg-Al alloy films on quartz substrates.

At room temperature, the Mg-65 at.% Al film composition lies in the Al (α) and Al_3Mg_2 (β) two phase region and the film is expected to contain predominantly the Al_3Mg_2 (β) (~90%). The Mg-59 at.% Al film composition lies in the Al_3Mg_2 (β) single phase region. The XRD patterns (Figure 5.3) for both Mg-65 at.% Al (35Mg-65 Al) and Mg-59 at.% Al (41 Mg- 59 Al) alloys do not show any peak corresponding to the Al_3Mg_2 (β) phase likely due to preferred orientation present in the sample where the grain orientations are such that the Bragg condition is not satisfied in the θ-2θ scan configuration. While it is possible that growth is preferred along distinct directions, even with small deviation of this

preferred growth direction from film normal, peak intensity can be dramatically reduced with relatively small film thickness levels. The other possibility is that the film is amorphous. For films examined with Mg content from 48 to 59 at.%, a two phase mixture containing Al_3Mg_2 (β) and $Al_{12}Mg_{17}$ (γ) is expected. In this composition range, the amount of $Al_{12}Mg_{17}$ (γ) phase increases to ~95% as Mg content increases to 58 at.%. In the XRD patterns for alloys in this composition range of 48 to 59 at.% Mg, a peak at 2θ value of 35.36° is observed. This peak corresponds to (400) peak from the $Al_{12}Mg_{17}$ (γ) phase grains with its intensity increasing as Mg content is increased. This suggests strong (400) preferred orientation of the γ phase which is based on bcc type Bravais lattice. For films examined with Mg contents from 70 to 97 at.%, two phase mixture of $Al_{12}Mg_{17}$ (γ) and Mg (α) phase is expected, with the amount of γ phase decreasing and consequently the decrease in the intensity of (400) peak of the γ phase as Mg content increases. At these high Mg contents, peaks at 34.71º which corresponds to the (0002) peak of Mg phase and its position is close to that of the (400) peak of the γ phase is observed. At Mg contents close to 97 at.%, the film mainly consists of pure Mg phase and peak count rates for the (0002) are similar to the observed values for [0002] textured pure Mg films.

5.4.4 Structure and optical responses of Mg-rich Mg-Al films

Figure 5.4 shows the AFM images of Mg-rich Mg-Al alloy films on fused quartz substrates. The RMS roughness values observed for Mg-rich alloy films are also shown in Figure 5.4. The surface roughness does not seem to vary significantly. For the purpose of analysis, Mg-rich Mg-Al alloy films are grouped into two categories (group 1 and 2) based on their deposition rates as highlighted in Table 5.2. Group 1 has 51Mg-49Al, 58Mg-42Al, and 70Mg-30Al and group 2 has 81Mg-19Al, 86Mg-14Al, 91Mg-9Al, and 97Mg-3Al.

Figure 5.5(a) and (b) show the optical constants ε_1 and ε_2 as a function of incident wavelength for group 1 Mg-rich Mg-Al alloy thin films. Figure 5.5(a) shows that the ε_1 values for group 1 Mg-rich Mg-Al alloy films lie between those of pure Al and Mg films. The same trend is seen for the ε_2 values for wavelengths above 300 nm (Figure 5.5(b)). Figure 5.5(c) shows a plot of the FOM_{LSP} versus wavelength and Figure 5.5(d) shows a plot of the FOM_{SPP} versus wavelength. FOM_{LSP} values increases with an increase in Mg content and the peak in the FOM_{LSP} curve blue shifts from 360 nm for pure Mg (1.8 Å/s) to 320 nm (a shift of about 40 nm) for 70Mg-30Al film. Both 58Mg-48Al and 70Mg-30Al alloy films have slightly higher FOM_{LSP} than pure Mg film at the short wavelengths (below about 300 nm) due to the blue shift even though the FOM_{LSP} peak is lowered. FOM_{SPP} values for the group 1 Mg-rich alloy films show no significant improvement and the value decreases after about 340 nm. Both 51Mg-48Al and 58Mg-42Al thin films show a strong (400) peak corresponding to the γ phase ($Al_{12}Mg_{17}$) (Figure 5.3). The results suggest that these intermetallic phases also improve FOM_{LSP} values at the short wavelengths (below about 290 nm) when compared to either pure Al or pure Mg (Figure 5.5(c)).

Figure 5.6(a) and (b) show the optical constants ε_1 and ε_2 as a function of wavelength for group 2 Mg-rich Mg-Al alloy thin films. Figure 5.6(a) shows that the ε_1 values for group 2 Mg-rich Mg-Al alloy films lie between those of pure Al and Mg films, and the same trend is seen for the ε_2 values (Figure 5.6(b)). Figure 5.6(c) presents a plot of the FOM_{LSP} versus wavelength and Figure 5.6(d) shows a plot of the FOM_{SPP} versus wavelength. FOM_{LSP} values increase with an increase in Mg content and the peak in the FOM_{LSP} curve blue shifts from 380 nm for pure Mg (5.2 Å/s) to about 330 nm (a shift of about 40 nm) for 81Mg-19Al. Like group 1 Mg-rich Mg-Al alloy films, Group 2 alloy

films also have slightly higher FOM_{LSP} than pure Mg film at the short wavelengths due to the blue shift even though the FOM_{LSP} peak is lowered. FOM_{SPP} values for the group 2 Mg-rich alloy films lie between those of pure Al and Mg films but 91Mg-9Al and 97Mg-3Al alloy films have higher FOM_{SPP} than either Mg or Al beyond 600 nm (Figure 5.6(c)). Figure 5.7 shows the plot of FOM_{LSP} value and peak position as a function of composition for Mg-rich Mg-Al alloy films. The FOM_{LSP} value of Mg-rich Mg-Al alloy films increases from 4.1 to 7.9 (pure Mg) with increase in Mg concentration. As discussed earlier, the addition of Al to Mg blue shifts the FOM_{LSP} peak position of Mg. However, increase in Mg content beyond about 70 at.% red shifts the FOM_{LSP} peak position towards the peak position for pure Mg.

5.4.5 Al-rich Mg-Al alloy thin films

Figure 5.8(a) and (b) show the optical constants ε_1 and ε_2 as a function of incident wavelength for Al-rich Mg-Al alloy thin films. Figure 5.8(a) shows that the ε_1 values for Al-rich Mg-Al alloy films lie between pure Al and Mg films. However, wavelengths from ~350 to 650 nm, Al-rich Mg-Al alloy films suffer higher losses (higher ε_2 values) when compared to both pure Al and Mg as shown in Figure 5.8(b). Figure 5.8(c) shows a plot of the FOM_{LSP} versus wavelength and Figure 5.8(d) shows a plot of the FOM_{SPP} versus wavelength. FOM_{LSP} values increases with the increase in Al content and the FOM_{LSP} curve of pure Al blue shifts from 330 nm to 280 nm (a shift of about 50 nm) for 65Al-35Mg film when compared to pure Al film but the values are still lower than pure Mg. FOM_{SPP} values for the alloy films show no improvement and value decreases after about 340 nm.

5.4.6 Transmission measurements of nanotriangles

Transmission measurements of nanotriangle arrays were performed using a Perkin Elmer Lambda 750 UV/Vis/NIR spectrophotometer with a cleaned quartz slide as a reference over a wavelength range of 200−2500 nm in air with a spot size of 1 cm.[2] Plots of ε_1, ε_2, and FOM_{LSP} as a function of wavelength (250 to 1700 nm) for pure Mg, pure Al, 81Mg-19Al, and 91Mg-9Al alloy films are shown in Figure 5.9(a), (b), and (c). For the fabrication of NTs, large PS bead templates were used to investigate the effect that alloying has on the LSPR response. These particles exhibit multiple LSPR modes from the UV to the NIR wavelengths as shown in Figure 5.9(d). As expected, Mg has poor plasmonic properties at these long wavelengths compared to pure Al. The Mg nanotriangles exhibit a broad, low intensity LSPR peak around 1250 nm attributed to a dipole mode as well as a broad shoulder in the visible wavelength that may be associated with a higher order quadrupole mode. Both a lack of structural integrity and LSPR coupling also may contribute to the broadness of the dipole peak. Pure Al nanotriangles exhibit multiple sharp LSPR peaks in the visible and NIR (near-infrared) wavelength range attributed to both dipole and quadrupole resonance modes.[18] The spectral response for the Al nanotriangles is relatively featureless in the UV.

By alloying Mg with Al, considerable improvement is seen in the LSPR response versus pure Mg particles, especially at longer wavelengths. In addition to the sharp dipole resonance at 1200 nm, the alloyed structures exhibit a smaller response at 700 (assigned to a quadrupole mode) and longer wavelength response centered at 1750 nm attributed to LSPR coupling between NTs.

While Mg has excellent plasmonic properties as a film, it may not be an ideal metal

for structuring at the nanoscale. However, the film studies show that alloying Mg with Al improves the plasmonic properties in the UV-Vis range, the addition of Al may also have an added benefit of helping the Mg to form better defined structures at nanometer sizes. Figure 5.10 shows SEM images comparing nanotriangles of Al, Mg, and 91Mg-9Al fabricated using 1400 nm PS templates. These images clearly show the Mg particles are much less defined and have a considerable variation in shape when compared to Al NTs fabricated in a similar fashion. As expected, this lack of definition leads to a severe broadening of the LSPR response of pure Mg as shown in Figure 5.9(d). However, alloying Mg with Al results in well-defined triangular shaped particles (Figure 5.10(c)), when compared to pure Mg. In addition, relatively sharp LSPR peaks are observed in the extinction spectra (Figure 5.9(d)). Addition of Al to Mg would tend to form MgO-Al_2O_3 spinel oxide which also stabilizes the shape of nanotriangles. In addition to rigorous structural studies, a thorough theoretical analysis would also be required to elucidate the contributions that shape and metal composition have on the observed LSPR response.

5.5 Conclusions

In summary, the results show that on increasing the deposition rate from 1.8 to 7.0 Å/s, the FOM_{LSP} of Mg films was found to increase. This could be attributed to the reduced surface roughness of the film which dominates the optical response when compared to electron scattering by grain size. The addition of Al to Mg tends to blue shift the FOM_{LSP} peak, resulting in small regions in the UV where an increased FOM can be realized. In the case of nanotriangle fabrication, addition of Al to Mg leads to considerable improvement in the LSPR response versus pure Mg particles, especially at longer wavelengths. Alloying

results in well-defined triangular shaped particles when compared to pure Mg, which produces relatively sharp LSPR peaks in the extinction spectra.

Table 5.1 Phases present in Al-Mg system at room temperature (based on [26]).

Composition Range	Equilibrium Phase Region(s) at Room Temperature	Crystal Structure / Space Group
0 to ~1 at.% Mg	Al solid solution (α)	FCC / *Fm3m*
~1 to 38.5 at.% Mg	α + Al_3Mg_2	-
38.5 to 40.3 at.% Mg	Al_3Mg_2 (β)	Cd_2Na type / $Fd3m(0_h^7)$
40.3 to ~60 at.% Mg	β + $Al_{12}Mg_{17}$	-
~60 at.% Mg	$Al_{12}Mg_{17}$ (γ)	α-Mn type / *I43m*
~60 to 99 at.% Mg	$Al_{12}Mg_{17}$ + Mg solid solution	-
~99 to 100 at.% Mg	Mg solid solution	HCP / $P6_3/mmc$

Table 5.2 Average composition of various Mg-Al alloy thin films.

Alloy	Sputter Power (W)		Mg (at.%)	Al (at.%)	Std. Dev.	Deposition Rate (Å/s)
	RF (Mg)	DC (Al)				
Pure Al	25	-	-	100	-	~4
35Mg -65Al	19	36	34.9	65.1	±0.5	1.8[(a)]
41Mg-59 Al	19	30	41.1	58.9	±0.5	1.8[(a)]
48Mg-52Al	19	27	48.3	51.7	±0.3	1.9[(a)]
51Mg-49Al	38	30	51.0	49.0	±0.3	2.4[(a)]
58Mg-42Al	25	15	57.6	42.4	±0.7	2.1[(a)]
70Mg-30Al	34	15	70	30	±0.5	2.1[(a)]
81Mg-19Al	60	13	81.3	18.7	±0.3	4.8[(a)]
86Mg-14Al	60	10	86.2	13.8	±1.3	5.4[(a)]
91Mg-9Al	60	8	90.6	9.4	±0.5	5.3[(a)]
97Mg-3Al	60	5	96.6	3.4	±0.2	5.2[(a)]
Pure Mg	60	-	100	-	-	5.2

Increasing Al Content ↑ / Increasing Mg Content ↓

[(a)] Relative deposition rates since the thickness monitor was set for Mg

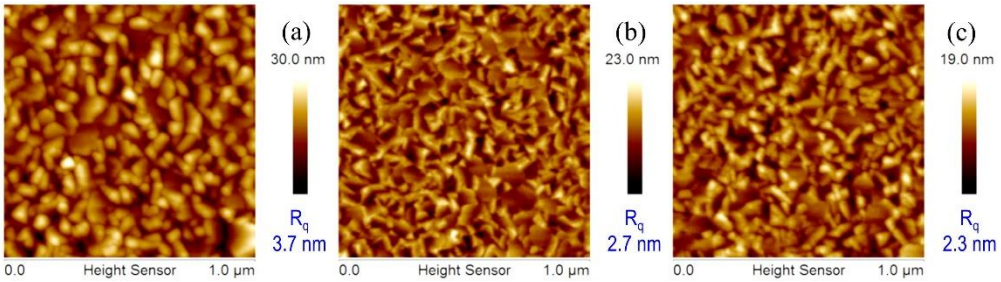

Figure 5.1 Surface roughness changes depending on deposition rate. AFM images of 100 nm thick Mg films on quartz with various deposition rates: (a) 1.8, (b) 5.2, and (c) 7.0 Å/s.

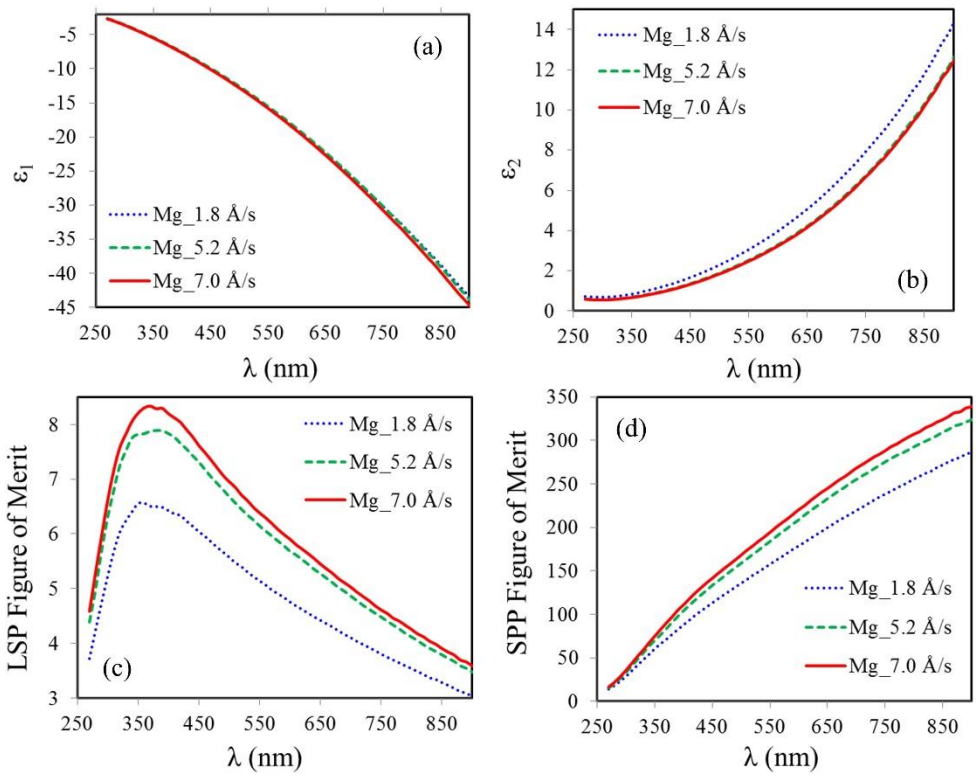

Figure 5.2 Optical response of Mg thin films deposited at different rates. Plots of (a) ε_1, (b) ε_2, (c) LSP figure of merit, and (d) SPP figure of merit as a function of wavelength for pure Mg films on quartz.

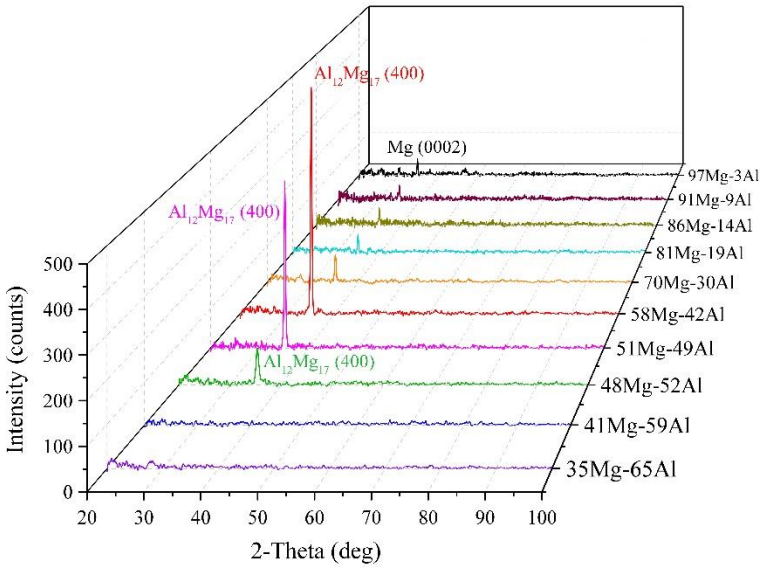

Figure 5.3 XRD patterns of Mg-Al alloy films on quartz substrate.

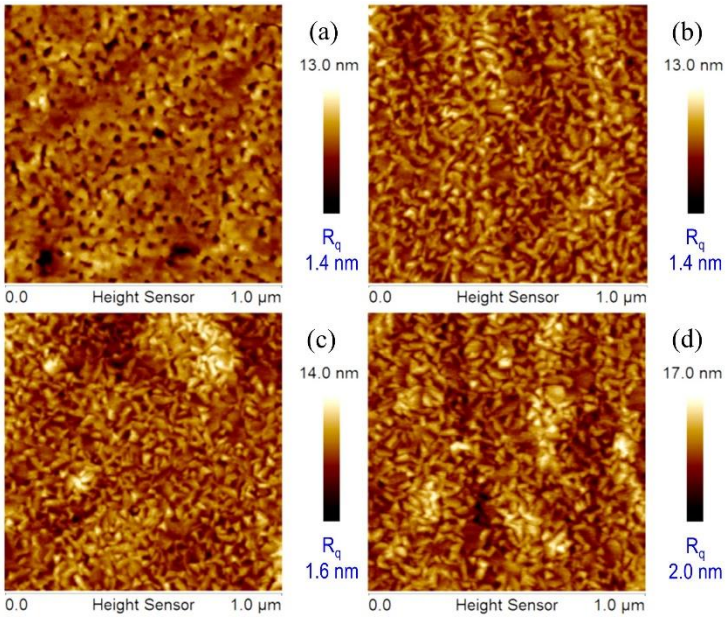

Figure 5.4 Surface roughness is dependent on alloy composition. AFM images of Mg-rich Mg-Al alloy films on quartz substrate: a) 58Mg-42Al, b) 86Mg-14Al, c) 91Mg-9Al, and d) 97Mg-3Al.

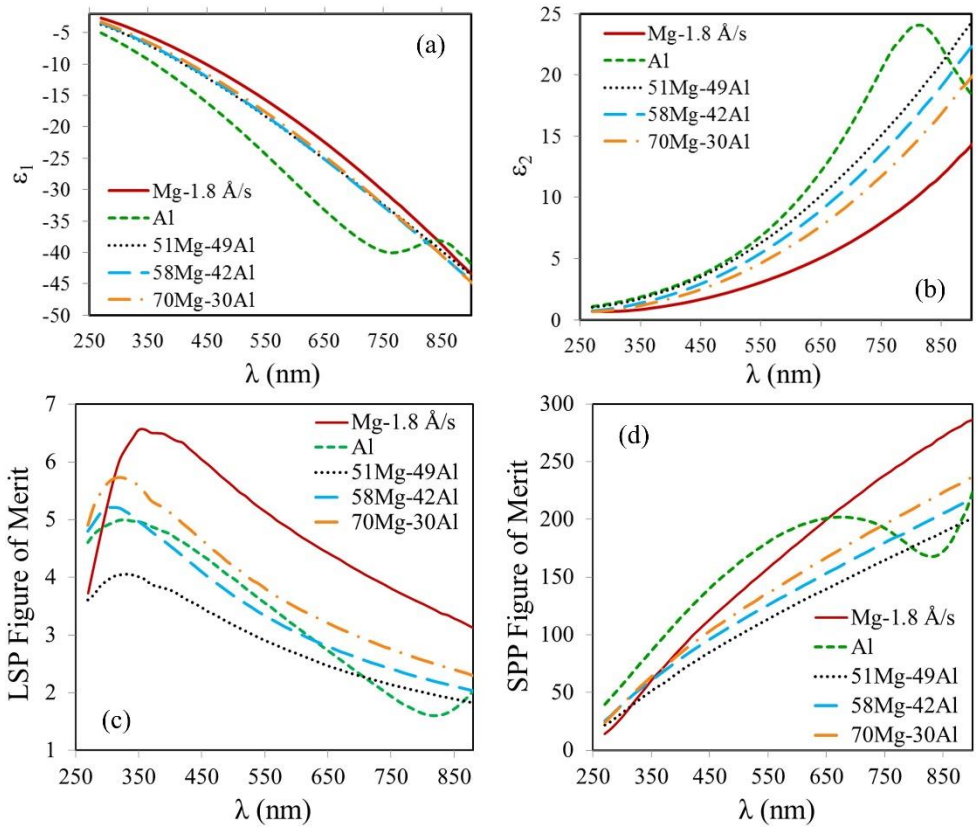

Figure 5.5 Optical response of thin alloy films that are predominantly Mg. Plots of (a) ε_1, (b) ε_2, (c) LSP figure of merit, and (d) SPP figure of merit as a function of wavelength for group 1 Mg-rich Mg-Al alloy films on quartz. (The deposition rates for the various thin films in this image are shown in Table 5.2.)

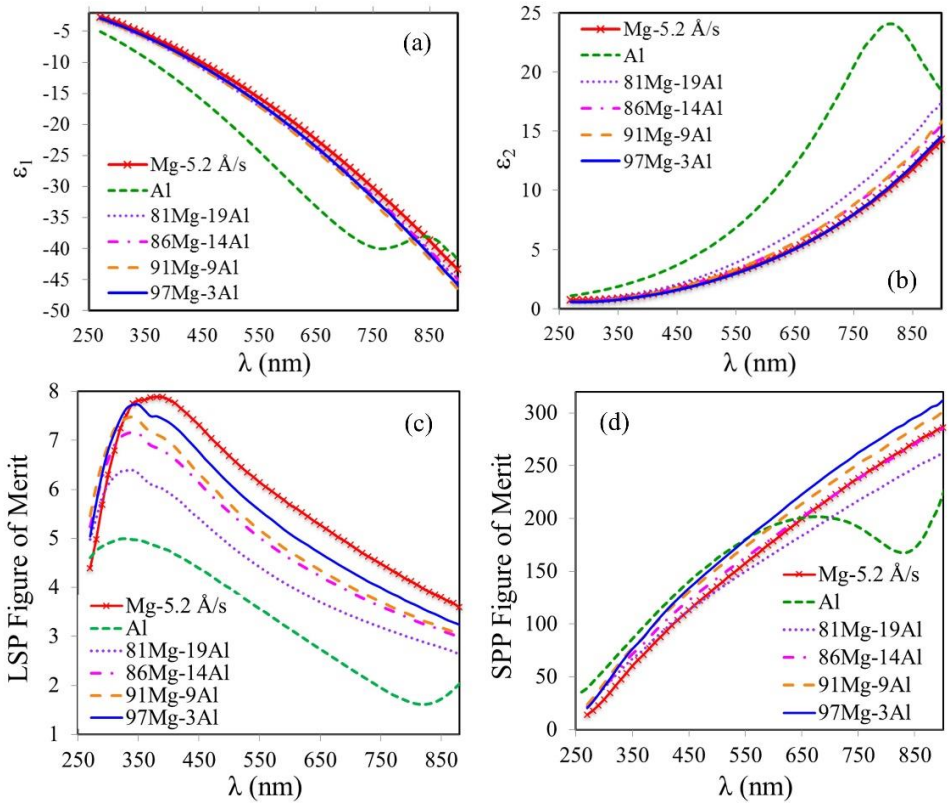

Figure 5.6 Optical response of thin alloy films rich in Al. Plots of (a) ε_1, (b) ε_2, (c) LSP figure of merit, and (d) SPP figure of merit as a function of wavelength for group 2 Mg-rich Mg-Al alloy films on quartz. (The deposition rates for the various thin films in this image are shown in Table 5.2.)

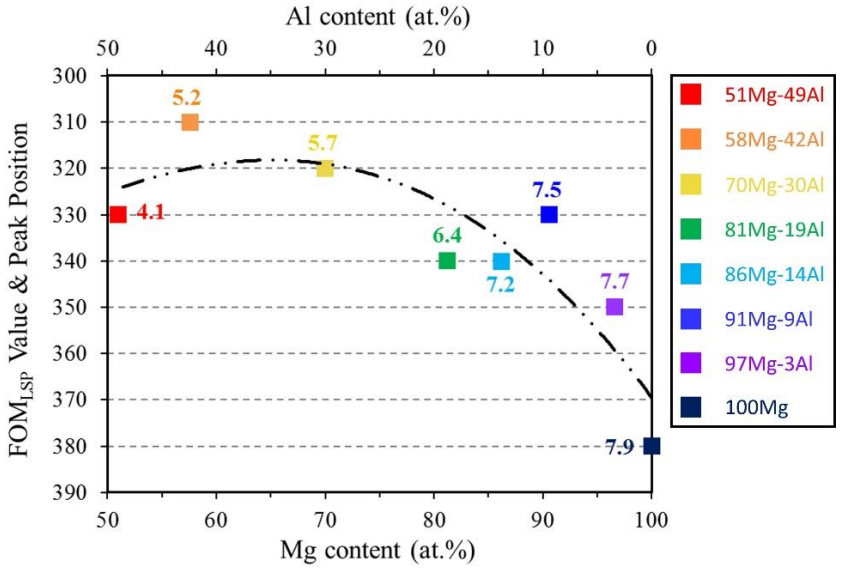

Figure 5.7 Plot of FOM_{LSP} value and its peak position (square) as a function of composition for Mg-rich Mg-Al alloy films.

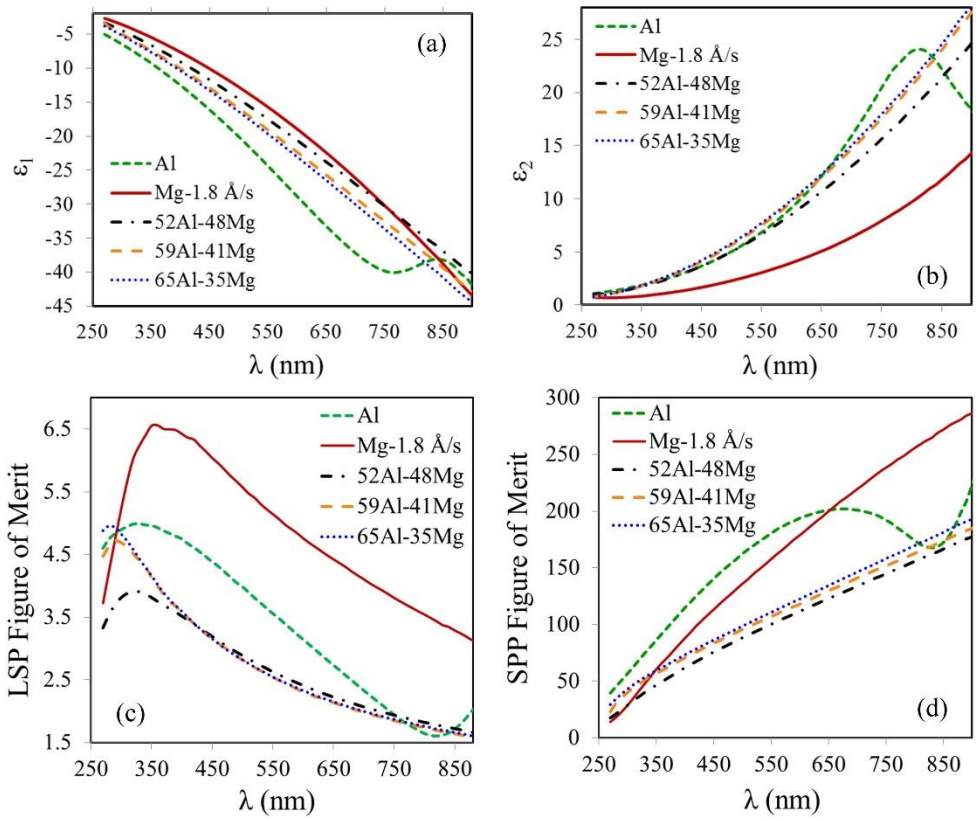

Figure 5.8 Optical response of thin alloy films rich in Al. Plots of (a) ε_1, (b) ε_2, (c) LSP figure of merit, and (d) SPP figure of merit as a function of wavelength for Al-rich Mg-Al alloy films on quartz.

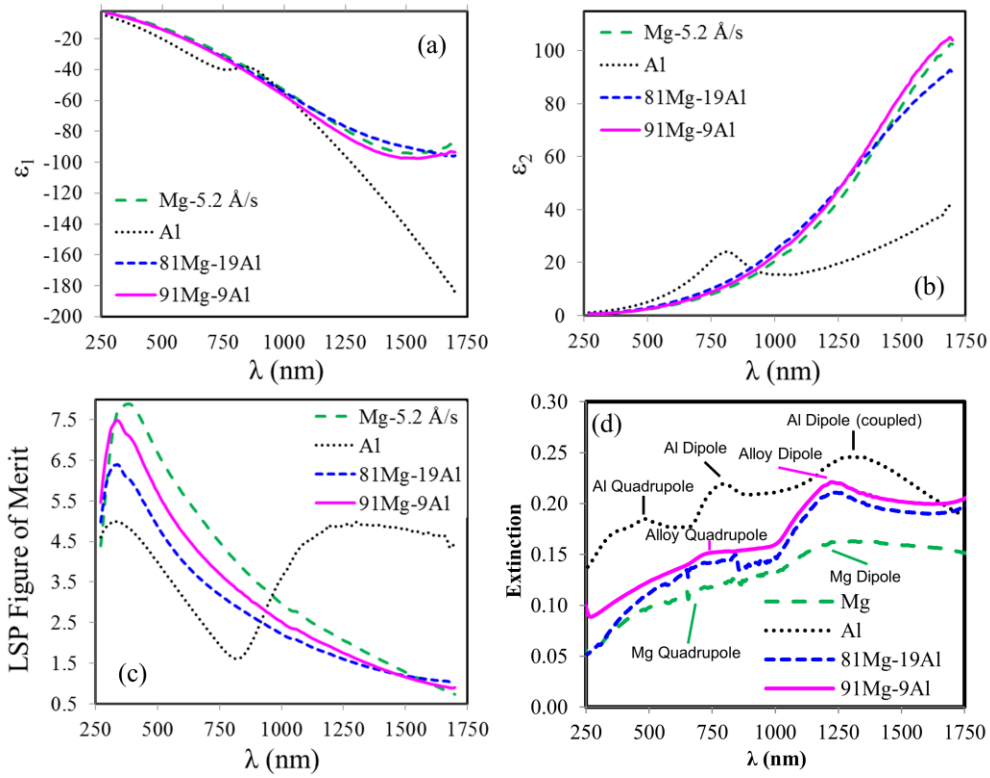

Figure 5.9 Optical response of Mg-Al alloys used for nanotriangle fabrication. Plots of (a) ε_1, (b) ε_2, and (c) LSP figure of merit as a function of wavelength for Mg-rich Mg-Al alloy films on quartz, and (d) comparison of extinction spectra of nanotriangles of Mg, Al, 81Mg-19Al, and 91Mg-9Al fabricated using 1400 nm PS beads with a film thickness of 50 nm.

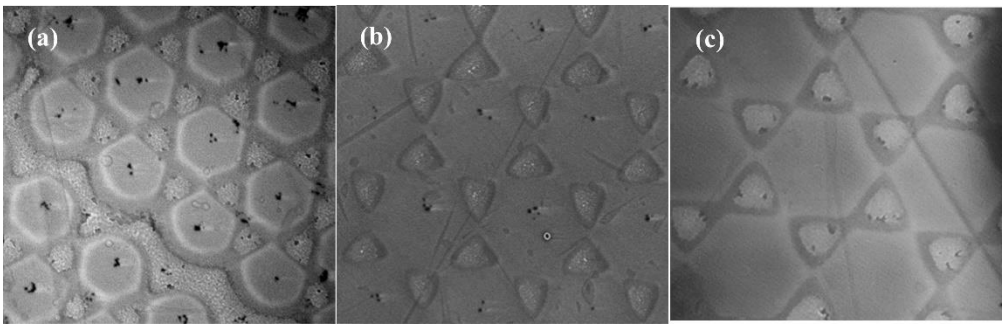

Figure 5.10 Sputtering Mg and Mg-Al alloys films over close-packed PS beads results in nanotriangles. SEM images of nanotriangles of (a) pure Mg, (b) pure Al, and (c) 91Mg-9Al fabricated using 1400 nm PS beads with a film thickness of 50 nm.

5.6 References

(1) S. A. Maier and H. A. Atwater, “Plasmonics: Localization and guiding of electromagnetic energy in metal/dielectric structures,” J. Appl. Phys. **98**(1), 011101 (2005).

(2) D. Gérard and S. K. Gray, “Special issue on aluminium plasmonics,” J. Phys. D Appl. Phys. **48**(18), 180301 (2015).

(3) K. Appusamy, S. Blair, A. Nahata, and S. Guruswamy, “Low-loss magnesium films for plasmonics,” Mater. Sci. Eng. B **181**, 77–85 (2014).

(4) K. Appusamy, X. Jiao, S. Blair, A. Nahata, and S. Guruswamy, “Mg thin films with Al seed layers for UV plasmonics,” J. Phys. D Appl. Phys. **48**(18), 184009 (2015).

(5) J. H. Simmons and K. S. Potter, Optical Materials (Academic Press 2000).

(6) H. Ehrenreich and H. R. Philipp, “Optical properties of Ag and Cu,” Phys. Rev. **128**(4), 1622–1629 (1962).

(7) M. H. Chowdhury, S. Chakraborty, J. R. Lakowicz, and K. Ray, “Feasibility of using bimetallic plasmonic nanostructures to enhance the intrinsic emission of biomolecules,” J Phys Chem C Nanomater Interfaces **115**(34), 16879–16891 (2011).

(8) D. A. Bobb, G. Zhu, M. Mayy, A. V. Gavrilenko, P. Mead, V. I. Gavrilenko, and M. A. Noginov, “Engineering of low-loss metal for nanoplasmonic and metamaterials applications,” Appl. Phys. Lett. **95**(15), 151102 (2009).

(9) C. Gong and M. S. Leite, “Noble metal alloys for plasmonics,” ACS Photonics **3**(4), 507–513 (2016).

(10) C. Zhang, D. Zhao, D. Gu, H. Kim, T. Ling, Y.-K. R. Wu, and L. J. Guo, “An ultrathin, smooth, and low-loss Al-doped Ag film and its application as a transparent electrode in organic photovoltaics,” Adv. Mater. **26**(32), 5696–5701 (2014).

(11) D. Gu, C. Zhang, Y.-K. Wu, and L. J. Guo, “Ultrasmooth and thermally stable silver-based thin films with subnanometer roughness by aluminum doping,” ACS Nano **8**(10), 10343–10351 (2014).

(12) D. Zhao, C. Zhang, H. Kim, and L. J. Guo, “High-performance Ta2O5/Al-doped Ag electrode for resonant light harvesting in efficient organic solar cells,” Adv. Energy Mater. **5**(17), 1500768 (2015).

(13) J. A. Woollam, B. D. Johs, C. M. Herzinger, J. N. Hilfiker, R. A. Synowicki, and C. L. Bungay, “Overview of variable-angle spectroscopic ellipsometry (VASE): I. Basic theory and typical applications,” Proc. SPIE **CR72**, 3–28 (1999).

(14) B. D. Johs, J. A. Woollam, C. M. Herzinger, J. N. Hilfiker, R. A. Synowicki, and C. L. Bungay, "Overview of variable angle spectroscopic ellipsometry (VASE), Part II: Advanced applications," Proc. SPIE **CR72**, 29–58 (1999).

(15) J. C. Hulteen and R. P. Van Duyne, "Nanosphere lithography: A materials general fabrication process for periodic particle array surfaces," J. Vac. Sci. Technol. A Vacuum, Surfaces. Film. **13**(3), 1553–1558 (1995).

(16) P. Moitra, B. A. Slovick, W. li, I. I. Kravchencko, D. P. Briggs, S. Krishnamurthy, and J. Valentine, "Large-scale all-dielectric metamaterial perfect reflectors," ACS Photonics **2**(6), 692–698 (2015).

(17) K. Chen, B. B. Rajeeva, Z. Wu, M. Rukavina, T. D. Dao, S. Ishii, M. Aono, T. Nagao, and Y. Zheng, "Moiré nanosphere lithography," ACS Nano **9**(6), 6031–6040 (2015).

(18) G. H. Chan, J. Zhao, G. C. Schatz, and R. P. Van Duyne, "Localized surface plasmon resonance spectroscopy of triangular aluminum nanoparticles," J. Phys. Chem. C **112**(36), 13958–13963 (2008).

(19) C. R. M. Grovenor, H. T. G. Hentzell, and D. A. Smith, "The development of grain structure during growth of metallic films," Acta Metall. **32**(5), 773–781 (1984).

(20) H. Savaloni and M. A. Player, "Influence of deposition conditions and of substrate on the structure of uhv deposited erbium films," Vacuum **46**(2), 167–179 (1995).

(21) K. M. McPeak, S. V. Jayanti, S. J. P. Kress, S. Meyer, S. Iotti, A. Rossinelli, and D. J. Norris, "Plasmonic films can easily be better: rules and recipes," ACS Photonics **2**(3), 326–333 (2015).

(22) D. A. Bobb, G. Zhu, M. Mayy, A. V. Gavrilenko, P. Mead, V. I. Gavrilenko, and M. A. Noginov, "Engineering of low-loss metal for nanoplasmonic and metamaterials applications," Appl. Phys. Lett. **95**(15), 151102 (2009).

(23) M. G. Blaber, M. D. Arnold, and M. J. Ford, "A review of the optical properties of alloys and intermetallics for plasmonics," J. Phys. Condens. Matter **22**(14), 143201 (2010).

(24) A. V. Zayats, I. I. Smolyaninov, and A. A. Maradudin, "Nano-optics of surface plasmon polaritons," Phys. Rep. **408**(3–4), 131–314 (2005).

(25) R. C. O'Handley, D. K. Burge, S. N. Jasperson, and E. J. Ashley, "Residual gas and the optical properties of silver films," Surf. Sci. **50**(2), 407–433 (1975).

(26) K. Yoshihara and K. Nii, "The effect of oxygen potential on the surface self-diffusion coefficient of silver," Trans. Japan Inst. Met. **20**(9), 533–542 (1979).

(27) T. B. Massalski, J. L. Murray, L. H. Bennett, and H. Baker, Binary Alloy Phase Diagrams (American Society for Metals, 1986).

CHAPTER 6

MAGNESIUM NANOHOLE ARRAYS

6.1 Introduction

There has been recent interest in plasmonic metals beyond gold and silver due to their inability to support plasmon resonances in the UV wavelength range. Many biological molecules absorb light at these low wavelengths and photocatalytic events are more likely to occur at these higher energies. Conventional plasmonic metals, such as silver and gold, are ill-equipped to support plasmon resonances at these low wavelengths because their interband transition lies at 350 and 450 nm, respectively. The presence of the interband transition leads to the excitation of electron-hole pairs instead of a collective electron oscillation.[1, 2] The use of non-noble (or poor) metals has been investigated as an alternative to Au and Ag at low wavelengths (<450 nm).[2] While Al is typically used for plasmonics in the UV range, it has been shown that Mg can have superior plasmonic properties at these wavelengths.[3-5]

Previous studies using Mg for plasmonics revealed that this metal is difficult to structure at the nanoscale. A common nanosphere lithography approach to nanotriangle fabrication that works well for other plasmonic metals such as gold, silver, aluminum, and copper did not work well for magnesium.[6-10] Prior work demonstrates that pure Mg does not form defined nanotriangles, instead the structures are rounded out where there should be sharp tips. Mg nanodisks have been fabricated using a hole-mask colloid lithography

method and used for hydrogen storage.[11] However, the emphasis of this work was using the plasmonic properties of the Mg as a redox indicator, not the plasmonic properties of Mg itself at low wavelengths. The fabrication of a plasmonic hole-array was employed to study the plasmonic properties of Mg. Hole-array structures have shown promising application in fields ranging from surface-enhanced Raman spectroscopy to lasing.[12-16] While Mg-hole arrays have shown promise in fluorescent lifetime modification, these structures were fabricated using focused ion-beam milling.[5] This technique is costly and covers a limited surface area, however, nanosphere lithography allows for the cost-effective fabrication of a hole array over large substrate areas.

One advantage of a hole array structure is the ability to excite surface plasmon polaritons in addition to localized surface plasmon resonances.[12, 17] The excitation of LSPR modes using a normal incidence geometry is quite typical and one of the advantages of using small metal nanoparticles for plasmonics. The excitation of a surface plasmon polariton (SPP) in a continuous metal film requires matching the wave vectors of the SPP and incident photon, which can be accomplished through the use of a prism. By using nanometer sized holes, wave vector matching can be achieved without the use of a prism. Here we have fabricated hexagonally close-pack nanohole arrays using nanosphere lithography to explore the plasmonic properties of nanostructured Mg.

6.2 Materials and Methods

Mg sputter targets were prepared by rolling Mg (99.99+%) from U.S. Magnesium to a size of 50 x 6.25 mm. Quartz substrates were cleaned for 45 min in piranha acid (3:1 volume ratio H_2SO_4: H_2O_2) and rinsed three times in water prior to use. Cleaned quartz substrates were placed in a petri dish elevated by 5˚ at one end and covered in water.

Aldehyde functionalized polystyrene (PS) microsphere templates were diluted 1:1 (volume ratio) in 200 proof ethanol and introduced to the petri dish using a microliter syringe pump. Once a monolayer of PS templates had formed at the water-air interface, as visible by eye, the water was pumped out of the petri dish using a peristaltic pump, transferring the monolayer to the quartz substrates.[18] PS microspheres were then shrunk using an oxygen plasma (Oxford).[12] Shrinking creates gaps in between the PS microspheres and leads to the templates that will define the nanopatterned film.

Thin, 25 nm films of magnesium were deposited in a custom built magnetron sputter chamber at base pressures of $<3 \times 10^{-7}$ Torr. After base pressure was achieved, argon gas was introduced into the chamber at a flow rate of 3.0×10^{-2} cc/min for 3 h prior to metal deposition to purge the chamber of any potential oxygen. Mg was deposited using an Advanced Energy 500 W RF power supply at a pressure of 2.5×10^{-3} Torr. Prior to deposition, the target was presputtered with the shutter closed for 10 min. This extended presputtering time was done to ensure that no oxidized magnesium would be deposited onto the substrates. Mg was deposited at a rate of 5 Å/s as it has been shown that reactive metals should be deposited quickly to prevent the incorporation of oxygen, leading to better plasmonic films.[19] The metal film thickness and deposition rate was monitored using a quartz crystal microbalance. PS templates were removed from the substrates using 3M scotch tape, leaving the Mg hole array attached to the substrate.

Substrates were characterized using UV/Vis transmission measurements and acquired with a normal incidence excitation using a Perkin Elmer Lambda 750 with a 1 cm^2 spot size. Spectra were acquired over a range of 200-2500 nm. Reflectance measurements were acquired using a 60 mm integrating sphere accessory from Perkin

Elmer. Hole diameter and surface roughness were characterized using a Bruker Dimension ICON-PT atomic force microscope (AFM).

6.3 Results and Discussion

Mg hole arrays were fabricated by close-packing and shrinking close-packed PS templates. Tuning of the pitch (distance between holes) was accomplished by changing the PS template size while the hole diameter was tuned by adjusting the plasma etch time. Figure 6.1A shows the AFM characterization of a 25 nm thin film of Mg deposited on a clean quartz substrate. Like Al, Mg is susceptible to oxidation and consequently a quality plasmonic film must be deposited rapidly. A fast metal deposition rate leads to grains in the film as they are regions of pure metal separated by oxide.[19] Arrays with a pitch of 400 nm and hole diameters of 330, 285, and 212 nm are shown in Figure 6.1 B, C, and D, respectively. Inside each of the holes there is evidence of either a ring or region of material that is taller than the metal film. This material is left over from the oxygen plasma etching of the PS templates. As the plasma etches the templates, some of the material redeposits underneath the sphere where it is protected from further plasma treatment. Since this material is essentially melted to the substrate, it does not come off with the scotch tape removal of the PS templates. This material can be removed using a strong nonpolar solvent such as toluene. To prevent the influence of this dielectric material on the plasmonic response, substrates were soaked in toluene overnight to remove any residue.

As the hole diameter decreases, the substrate is covered by a larger portion of the Mg film. Consequently, the transparency of small-diameter hole arrays begins to reflect an unmodified 25 nm Mg film (Figure 6.2). Transmission spectra of a 400 nm pitch hole array with decreasing hole diameters compared to a film clearly demonstrates this

phenomenon (Figure 6.2A). In addition to a decrease in the optical transmission, changing the hole size leads to changes in the SPP and LSPR modes.[12] The prominent features are labeled in the spectra. For a 330, 285, and 210 nm diameter hole arrays, a peak in transmission is observed at 1085, 960, and 835 nm, respectively, and the line shape broadens as the hole diameter increases (Figure 6.2A-1).[12] A dip, or decrease, in the transmission is observed at 400 nm and coincides with the pitch of the hole array (Figure 6.2A-3). The most prominent feature in all these transmission measurements is the dip around 600 nm (Figure 6.2A-2). This dip shifts slightly in response to changes in the hole diameter, from 600 nm for a 212 nm diameter hole to 635 nm for a 333 nm diameter hole.

When the pitch of the HNA is decreased to 330 nm, similar spectral features are observed (Figure 6.2B). Indeed the general shape of the transmission spectra are preserved, albeit shifted to shorter wavelengths (Figure 6.2C). The prominent dip in transmission shows a slight blue-shift from 525 nm to 505 nm as the template diameter increases (6.2B-2). The 330 nm pitch hole arrays exhibit a broadening and red-shifting of the transmission peak (6.2B-1). Again, we expect to observe a dip in transmission that corresponds to the pitch of the hole array. While this dip is present in our optical spectra, it shifts slightly based on hole diameter (Figure 6.2B-3). Comparing two hole arrays with similar hole diameters, but different spacing, shows that most of the spectral features are shifting as a result of pitch (Figure 6.2D). The two spectra are very similar except for the width of the dip (Figure 6.2D-1).

Reflection measurements were collected with both specular and diffuse reflected light (Figure 6.3). Using the combination of transmission and reflection spectra, the absorption of the hole arrays is determined as $A = 100 - R - T$.[17] Smaller diameter holes

have a higher overall reflectivity (Figure 6.3A/B) due to the higher portion of metal film. Increased reflectivity at discrete wavelengths is the result of an increased scattering due to LSPR. For a 330 nm pitch hole array, there are three features that lead to an increased reflectivity for both hole diameters. For a 129 nm diameter hole, increased reflectivity is observed at 1530 nm, 490 nm, and 330 nm (Figure 6.3A/C). The peak at longer wavelengths increases to 1605 nm for a larger diameter hole (Figure 6.3B). However. the two lower wavelength peaks at 490 nm and 330 nm do not shift as the hole diameter increases to 195 nm (Figure 6.3D).

Previous simulations show that the maximum absorption also coincide with the largest electric field enhancement.[12] Tuning the location of this absorption peak is of interested for SERS applications and is accomplished through changes in the HNA diameter (Figure 6.3C/D). By changing the hole diameter from 195 nm to 130 nm, the maximum absorption peak is shifted from 560 nm to 600 nm, respectively. A broad absorption peak is observed between 340-370 nm and is associated with the periodicity of the hole array.

Observing and assigning wavelengths to different features in our hole array spectra is fairly straightforward. Assigning the observed features to LSP or SPP modes is slightly more complex and will require theoretical simulations. However, a preliminary assignment of the three different spectral features will be made. In the transmission spectra, the dip labeled “2” is presumed to be due to a LSP mode. This mode exhibited the strongest peak in the reflection measurement, indicating that is scattering the incident light. LSP modes are known to strongly absorb and scatter light.[20] The alternate dip in the transmission spectra, labeled “3,” is attributed to the periodicity of the grating. It is anticipated that the

wavelength of light that matches the periodicity of the array couples into the hole array structure, leading to a decreased transmission. For now, the peak in transmission labeled "1" is being attributed to the SPP of the hole array. An increase in the transmission is observed for this mode, and has been attributed to a phenomenon called enhanced optical transmission (EOT).[12, 13, 21-24] EOT is attributed to the SPP on both sides of the hole array reconnecting and reradiating the light.

6.4 Conclusions

Nanosphere template lithography was used to fabricate nanohole arrays in Mg thin films. The optical properties of these nanostructured films were tuned by changing the pitch and diameter of the hole array. Unlike the Mg nanotriangles, these hole arrays retained their intended nanometer scale features. Additional theoretical work is still required to assign the spectral features to either LSP or SPP modes, however, a preliminary assignment based on related literature was made. Much experimental work is needed to make Mg competitive with Al as a plasmonic material, specifically, its lack of stability in the presence of water. However, its optical properties are favorable, and with some chemical modification, may be a viable alternative to Al, Au, and even Ag.

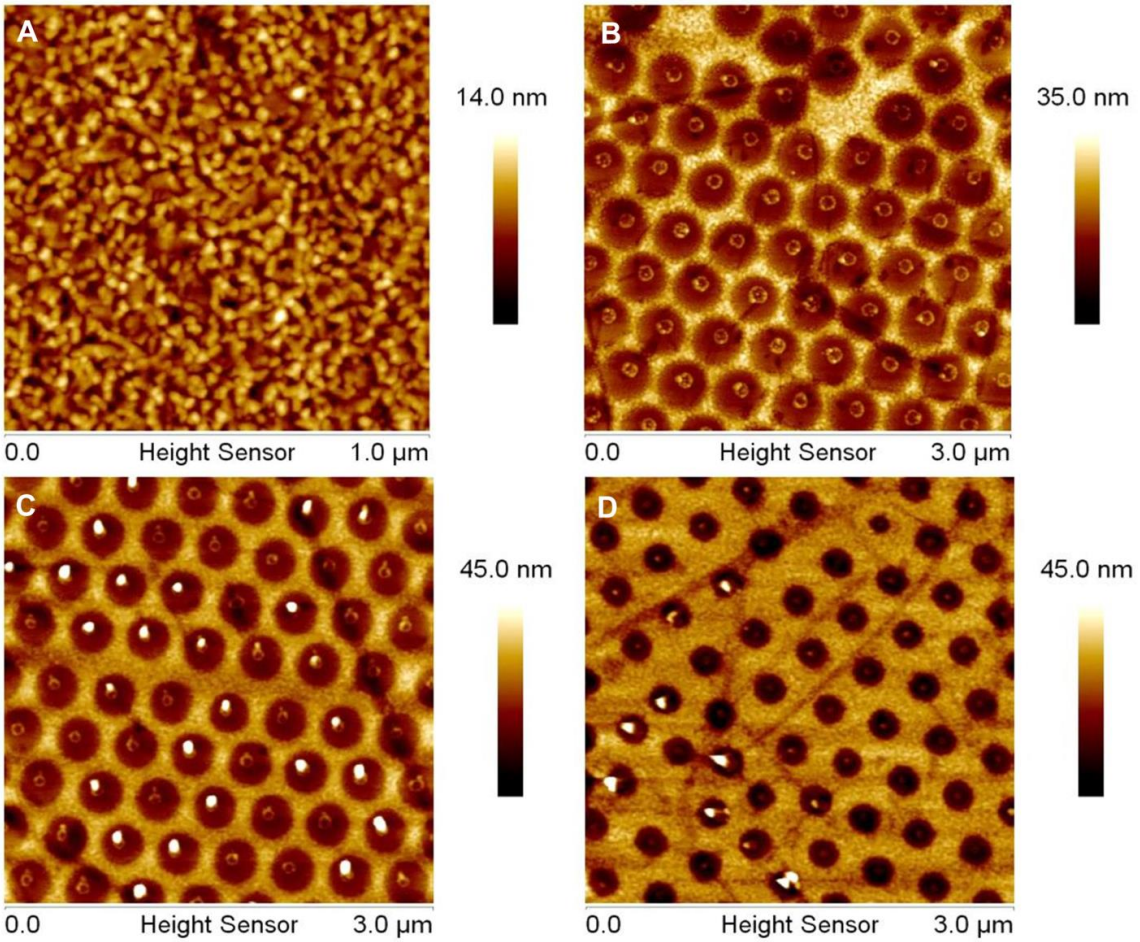

Figure 6.1 Structural characterizations of Mg hole arrays were conducted using AFM. The surface roughness of a 25 nm thin film of Mg (A) shows that the film is continuous. B-D) Hole array in a 25 nm film of Mg fabricated using nanosphere template lithography. All arrays have a pitch of 400 nm and hole diameters of 330 nm (B), 285nm (C), and 212 nm (D).

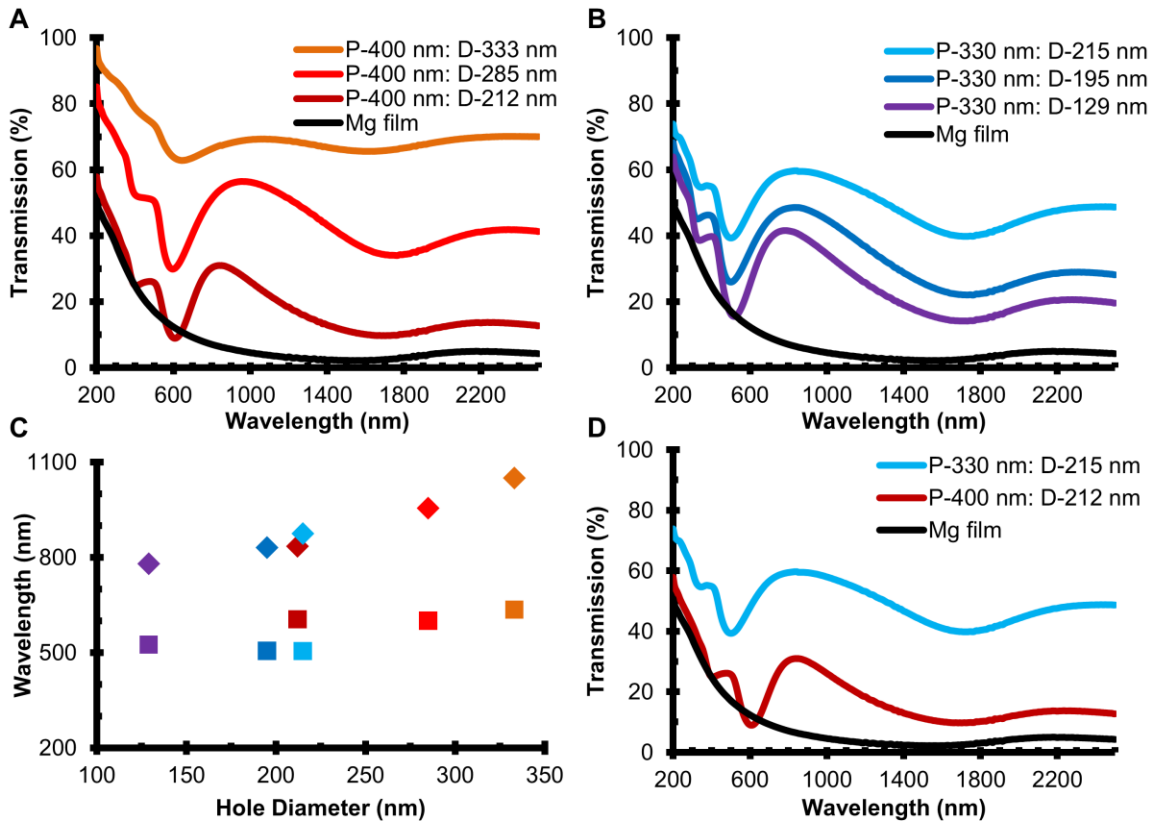

Figure 6.2 Transmission UV/Vis/NIR measurements of Mg hole arrays. A) 400 nm and 330 nm (B) pitch hole arrays with varying hole diameters. C) Plot of the SPP (>800 nm) and LSP (<800 nm) modes for the different pitch and diameter hole arrays. D) A comparison of the optical properties of two Mg hole arrays with different pitches but similar diameters.

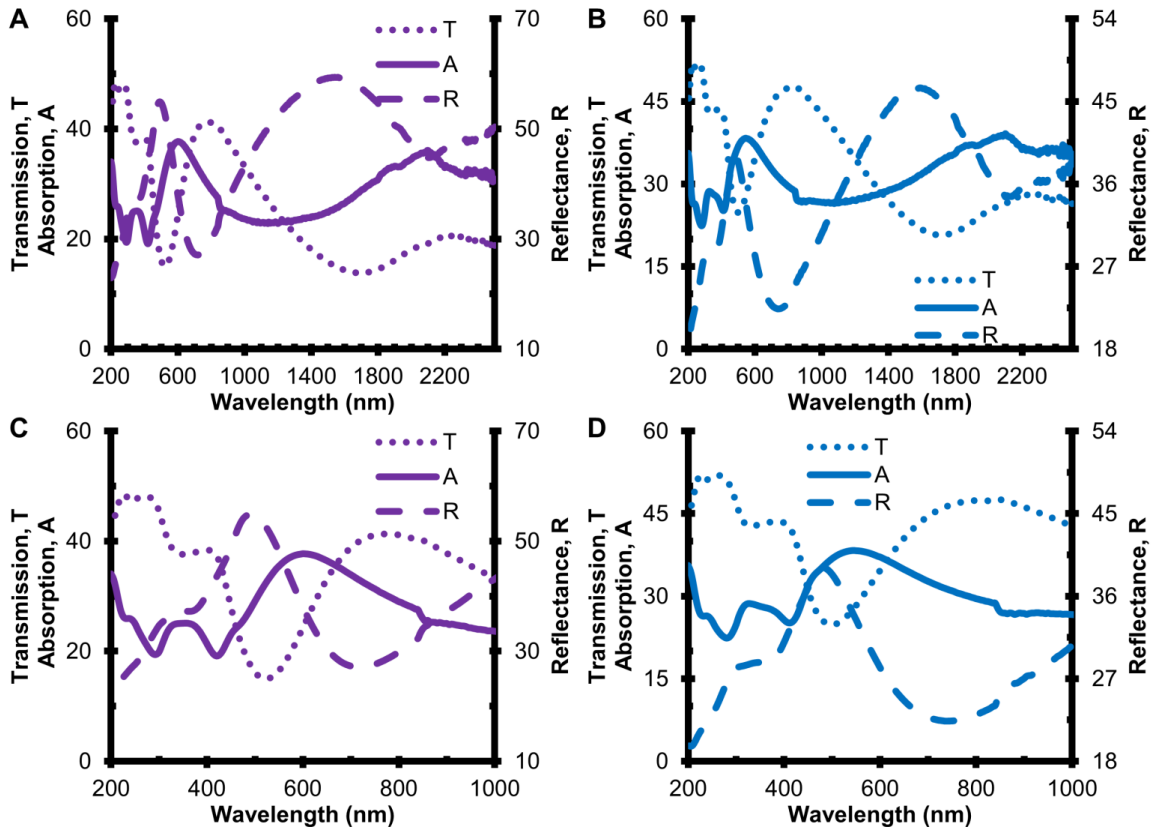

Figure 6.3 Comparing the reflected and transmitted spectra helps to distinguish between SPP and LSP modes. Reflection (R) and transmission (T) measurements for 330 nm pitch hole arrays with 129 nm (A/C) and 195 nm (B/D) diameter holes. Absorption (A) was calculated as A = 100 – T – R. Transmission measurements are the result of absorption and scattering, by subtracting out the reflectance spectra the light lost due to scattering is eliminated.

6.5 References

(1) Davy, G.; Stephen, K. G. Aluminium Plasmonics. *J. Phys. D: Appl. Phys.* **2015**, *48*, 184001.

(2) McMahon, J. M.; Schatz, G. C.; Gray, S. K. Plasmonics in the Ultraviolet with the Poor Metals Al, Ga, In, Sn, Tl, Pb, and Bi. *Phys. Chem. Chem. Phys.* **2013**, *15*, 5415-5423.

(3) Appusamy, K.; Blair, S.; Nahata, A.; Guruswamy, S. Low-Loss Magnesium Films for Plasmonics. *Mat. Sci. Eng. B-Solid* **2014**, *181*, 77-85.

(4) Kanagasundar, A.; Xiaojin, J.; Steve, B.; Ajay, N.; Sivaraman, G. Mg Thin Films with Al Seed Layers for UV Plasmonics. *J. Phys. D: Appl. Phys.* **2015**, *48*, 184009.

(5) Xiaojin, J.; Yunshan, W.; Steve, B. UV Fluorescence Enhancement by Al and Mg Nanoapertures. *J. Phys. D: Appl. Phys.* **2015**, *48*, 184007.

(6) Chan, G. H.; Zhao, J.; Hicks, E. M.; Schatz, G. C.; Van Duyne, R. P. Plasmonic Properties of Copper Nanoparticles Fabricated by Nanosphere Lithography. *Nano Lett.* **2007**, *7*, 1947-1952.

(7) Chan, G. H.; Zhao, J.; Schatz, G. C.; Duyne, R. P. V. Localized Surface Plasmon Resonance Spectroscopy of Triangular Aluminum Nanoparticles. *J. Phys. Chem. C* **2008**, *112*, 13958-13963.

(8) Haynes, C. L.; Van Duyne, R. P. Nanosphere Lithography: A Versatile Nanofabrication Tool for Studies of Size-Dependent Nanoparticle Optics. *J. Phys. Chem. B* **2001**, *105*, 5599-5611.

(9) Hulteen, J. C.; Van Duyne, R. P. Nanosphere Lithography: A Materials General Fabrication Process for Periodic Particle Array Surfaces. *J. Vac. Sci. Technol. A* **1995**, *13*, 1553-1558.

(10) Jensen, T. R.; Malinsky, M. D.; Haynes, C. L.; Van Duyne, R. P. Nanosphere Lithography: Tunable Localized Surface Plasmon Resonance Spectra of Silver Nanoparticles. *J. Phys. Chem. B* **2000**, *104*, 10549-10556.

(11) Sterl, F.; Strohfeldt, N.; Walter, R.; Griessen, R.; Tittl, A.; Giessen, H. Magnesium as Novel Material for Active Plasmonics in the Visible Wavelength Range. *Nano Lett.* **2015**, *15*, 7949-7955.

(12) Zheng, P.; Cushing, S. K.; Suri, S.; Wu, N. Tailoring Plasmonic Properties of Gold Nanohole Arrays for Surface-Enhanced Raman Scattering. *Phys. Chem. Chem. Phys.* **2015**, *17*, 21211-21219.

(13) Gao, H.; Henzie, J.; Odom, T. W. Direct Evidence for Surface Plasmon-Mediated Enhanced Light Transmission through Metallic Nanohole Arrays. *Nano Lett.* **2006**, *6*,

2104-2108.

(14) Kwak, E.-S.; Henzie, J.; Chang, S.-H.; Gray, S. K.; Schatz, G. C.; Odom, T. W. Surface Plasmon Standing Waves in Large-Area Subwavelength Hole Arrays. *Nano Lett.* **2005**, *5*, 1963-1967.

(15) Odom, T. W.; Gao, H.; McMahon, J. M.; Henzie, J.; Schatz, G. C. Plasmonic Superlattices: Hierarchical Subwavelength Hole Arrays. *Chem. Phys. Lett.* **2009**, *483*, 187-192.

(16) Yang, A.; Hoang, T. B.; Dridi, M.; Deeb, C.; Mikkelsen, M. H.; Schatz, G. C.; Odom, T. W. Real-Time Tunable Lasing from Plasmonic Nanocavity Arrays. *Nat. Commun.* **2015**, *6*.

(17) Murray, W. A.; Astilean, S.; Barnes, W. L. Transition from Localized Surface Plasmon Resonance to Extended Surface Plasmon-Polariton as Metallic Nanoparticles Merge to Form a Periodic Hole Array. *Phys. Rev. B* **2004**, *69*, 165407.

(18) Chen, K.; Rajeeva, B. B.; Wu, Z.; Rukavina, M.; Dao, T. D.; Ishii, S.; Aono, M.; Nagao, T.; Zheng, Y. Moiré Nanosphere Lithography. *ACS Nano* **2015**, *9*, 6031-6040.

(19) McPeak, K. M.; Jayanti, S. V.; Kress, S. J. P.; Meyer, S.; Iotti, S.; Rossinelli, A.; Norris, D. J. Plasmonic Films Can Easily Be Better: Rules and Recipes. *ACS Photonics* **2015**, *2*, 326-333.

(20) Kelly, K. L.; Coronado, E.; Zhao, L. L.; Schatz, G. C. The Optical Properties of Metal Nanoparticles: The Influence of Size, Shape, and Dielectric Environment. *J. Phys. Chem. B* **2003**, *107*, 668-677.

(21) Correia-Ledo, D.; Gibson, K. F.; Dhawan, A.; Couture, M.; Vo-Dinh, T.; Graham, D.; Masson, J.-F. Assessing the Location of Surface Plasmons Over Nanotriangle and Nanohole Arrays of Different Size and Periodicity. *J. Phys. Chem. C* **2012**, *116*, 6884-6892.

(22) Grupp, D. E.; Lezec, H. J.; Ebbesen, T. W.; Pellerin, K. M.; Thio, T. Crucial Role of Metal Surface in Enhanced Transmission through Subwavelength Apertures. *Appl. Phys. Lett.* **2000**, *77*, 1569-1571.

(23) Martín-Moreno, L.; García-Vidal, F. J.; Lezec, H. J.; Pellerin, K. M.; Thio, T.; Pendry, J. B.; Ebbesen, T. W. Theory of Extraordinary Optical Transmission through Subwavelength Hole Arrays. *Phys. Rev. Lett.* **2001**, *86*, 1114-1117.

(24) Barnes, W. L.; Dereux, A.; Ebbesen, T. W. Surface Plasmon Subwavelength Optics. *Nature* **2003**, *424*, 824.

CHAPTER 7

CONCLUSION AND FUTURE WORK

7.1 Conclusion

A method for fabricating aluminum nanocrescents (AlNCs) was developed by combining nanosphere template lithography (NTL) with a sacrificial copper mask. This method is a cost-effective way to produce oriented AlNCs over large substrate areas. These AlNCs have localized surface plasmon resonances (LSPR) that can be tuned from the UV through IR wavelength range simply by changing the template size. For the first time, NCs with dipole resonances in the UV were successfully fabricated. The oxide layer thickness of AlNCs was subsequently characterized using energy dispersive spectroscopy (EDS) with high-resolution scanning transmission electron microscopy (HR-S/TEM). HR-S/TEM revealed that the native oxide layer of the Al was unaffected by the fabrication process. This was expected as these particles demonstrated particularly strong LSPR throughout the UV, visible, and near-infrared wavelength ranges.[1]

AlNCs were shown to be useful for spectroscopic enhancement in the infrared wavelength range. First, the particle density had to be maximized to increase the overall signal. By arranging the polystyrene templates in a hexagonal close-packed array and subsequently shrinking the templates with an oxygen plasma, the surface density of AlNCs was maximized. Arrays of AlNCs were tuned to have LSPR in the IR wavelength range. Using a simple transmission geometry setup in a FT-IR instrument, the surface-enhanced

infrared absorption (SEIRA) of an array of AlNCs was measured. Arrays of Au and AlNCs were shown to enhance the IR absorption of a monolayer of molecules on the surface. Combining NTL with a sacrificial copper layer allows for the fabrication of more complex nanoparticle geometries. Coupled nanoparticle systems were made using the native oxide of aluminum as a spacer between two nanocrescents. Arrays of dimer nanocrescents were shown to have optical spectra far more complex than anticipated. Additional complexity was achieved by utilizing two different plasmonic metals to produce bimetallic dimer nanocrescents.

Magnesium was investigated as an alternative metal to Al for plasmonics in the UV wavelength range. Alloying Mg with Al improved the LSP figure of merit in the UV wavelength range. Fabricating Mg nanotriangles proved to be challenging, as sharp features, which lead to large field enhancements, were not supported by Mg. By alloying Mg with Al, an improvement was observed in the nanoscale structure. To continue investigating the LSPR properties of Mg, nanohole arrays were fabricated. These hole arrays support both surface plasmons and localized surface plasmons. Due to the lack of sharp features, there was no issue in the maintaining the nanoscale geometry.

7.2 Future Work

Research showing the utility of AlNC system in surface-enhanced spectroscopies, in addition to SEIRA, is necessary. Preliminary work showing that the particles enhanced IR absorption is a promising start. The basic premise of the project was that Al supports plasmons in the UV, which we have shown. However, it is necessary to demonstrate that AlNCs can enhance fluorescence and Raman signal as predicted. These particles are predicted to be excellent substrates for surface-enhanced fluorescence (SEF) and Raman

spectroscopy (SERS) due to their sharp tips and large field enhancements.[2] Additionally, both SEIRA and SERS enhancement may be possible on a single AlNC substrate.

Further characterization is required to show that there is in fact a uniform gap separating the two particles. While the complex optical response is indicative of plasmonic coupling, further characterization is required to confirm some of the structural details. EDS combined with HR-S/TEM would be the best instrument accessible for characterizing such a small gap. Additionally, finite difference time domain (FDTD) simulations are necessary to provide insight into the magnitude and shape of the near field enhancement of these particles. These DNCs structures could prove to be very useful in surface-enhanced spectroscopies such as SERS and SEIRA. Additional studies concerning the chiroptical response of these structures must also be conducted. Do to their asymmetric structure and gap separation in the z-direction, DNCs may interact strongly with circularly polarized light. If so these structures have the potential to be used in superlensing, chiral catalysis, and may be useful as a negative refractive index material.

Significant work remains for magnesium to be a viable metal in plasmonic applications. While the optical properties of Mg are favorable over the UV and visible wavelength ranges, the chemical reactivity of the metal is a severe hindrance. Since Mg oxidizes rapidly in the presence of water, it cannot be used in any biological applications. The stability of the Mg-Al alloys in the presence of water should be examined to determine the uses of such alloys for plasmonics. Alternative methods for the passivation of Mg include plasma etching with SF_6 or CF_4. This would, theoretically, provide a thin layer of MgF_2 over the surface that would prevent water from oxidizing the nanostructures and destroying the plasmonic properties of the metal. While it is possible to sputter MgF_2 over

a Mg film, these targets are expensive; consequently plasma etching may be a more cost-effective alternative.

7.3 References

(1) Swartz, M.; Rodriguez, M.; Quast, A. D.; Cooper, C. T.; Blair, S.; Shumaker-Parry, J. S. Aluminum Nanocrescent Plasmonic Antennas Fabricated by Copper Mask Nanosphere Template Lithography. *J. Phys. Chem. C* **2016**, *120*, 20597-20603.

(2) Rodriguez, M.; Furse, C.; Shumaker-Parry, J. S.; Blair, S. Scaling the Response of Nanocrescent Antennas into the Ultraviolet. *ACS Photonics* **2014**, *1*, 496-506.